2014

Modeling and Spray Pyrolysis Processing of Mixed Metal Oxide Nano-Composite Gas Sensor Films

Seyed Mohammad Navid Khatami
University of Central Florida

STARS Citation

Khatami, Seyed Mohammad Navid, "Modeling and Spray Pyrolysis Processing of Mixed Metal Oxide Nano-Composite Gas Sensor Films" (2014). *Electronic Theses and Dissertations, 2004-2019*. 685.
https://stars.library.ucf.edu/etd/685

MODELING AND SPRAY-PYROLYSIS PROCESSING
OF MIXED METAL OXIDE NANO-COMPOSITE GAS SENSOR FILMS

by

SEYED MOHAMMAD NAVID KHATAMI
B.Sc., Iran University of Science and Technology, 2004
M.Sc., Iran University of Science and Technology, 2007
M.Sc., University of Central Florida, 2012

A dissertation submitted in partial fulfillment of the requirements
for the degree of Doctor of Philosophy
in the Department of Mechanical and Aerospace Engineering
in the College of Engineering and Computer Science
at the University of Central Florida
Orlando, Florida

Fall Term
2014

Major Advisor: Olusegun J. Ilegbusi

ABSTRACT

The role of sensor technology is obvious in improvement and optimization of many industrial processes. The sensor films, which are considered the core of chemical sensors, have the capability to detect the presence and concentration of a specific chemical substance. Such sensor films achieve selectivity by detecting the interaction of the specific chemical substance with the sensor material through selective binding, adsorption and permeation of analyte. This research focuses on development and verification of a comprehensive mathematical model of mixed metal oxide thin film growth using spray pyrolysis technique (SPT). An experimental setup is used to synthesize mixed metal oxide films on a heated substrate. The films are analyzed using a variety of characterization tools. The results are used to validate the mathematical model. There are three main stages to achieve this goal: 1) A Lagrangian-Eulerian method is applied to develop a CFD model of atomizing multi-component solution. The model predicts droplet characteristics in flight, such as spatial distribution of droplet size and concentration. 2) Upon reaching the droplets on the substrate, a mathematical model of multi-phase transport and chemical reaction phenomena in a single droplet is developed and used to predict the deposition of thin film. The various stages of droplet morphology associated with surface energy and evaporation are predicted. 3) The processed films are characterized for morphology and chemical composition (SEM, XPS) and the data are used to validate the models as well as investigate the influence of process parameters on the structural characteristics of mixed metal oxide films. The structural characteristics are investigated of nano structured thin films comprising of ZnO, SnO_2, $ZnO+In_2O_3$ and $SnO_2+In_2O_3$ composites. The model adequately predicts the size distribution and film thickness when the nanocrystals are well-structured at the controlled temperature and concentration.

To Zhoobin

ACKNOWLEDGEMENTS

I would like to thank Dr. Olusegun Ilegbusi for serving as my academic advisor and his guidance on various aspects of the project. I also wish to thank Dr. Leonid Trakhtenberg for his valuable direction and his insights on the sensor aspects of the current study. My thanks also go to Dr. Son Ho at FAZ Technology, Orlando, FL for his guidance both academically and professionally. I am grateful to Dr. Alain Kassab, Dr. Kevin Coffey, Dr. Weiwei Deng and Dr. Eduardo Divo for being kind enough to serve in my committee and reviewing the manuscript. I also wish to acknowledge the cooperation and guidance of Mr. Kirk Scammon on material characterization at Advanced Materials Processing and Analysis Center (AMPAC), Orlando, FL. My research would not have been possible without their help.

I am grateful to the members of our research group particularly Mr. Nadun Kuruppumullage who helped me significantly at various phases of experimental procedures. Their assistance and companionship have been invaluable in completing this research effort.

I express my gratitude to my family for their continuing love and encouragement. They were always supporting me and encouraging me with their best wishes.

Last, but most important, I would like to thank my lovely wife Zhoobin who has tolerated long hours of solitude with wonderful unconditional support. She was always there cheering me up and stood by me through the good times and bad.

The project was supported by the US National Science Foundation under grant number CMMI-1030689.

TABLE OF CONTECTS

LIST OF FIGURES

LIST OF TABLES

CHAPTER 1: INTRODUCTION

1.1 Problem Considered

This research focuses on development and verification of a comprehensive mathematical model of the spray pyrolysis method for nanocomposite sensor film growth. The model is used to design an experimental apparatus for synthesis of mixed metal oxide films on a substrate. The films developed are analyzed using a variety of characterization tools. The results are used to validate the mathematical model.

Sensor technology plays a key role in the improvement and optimization of many important industrial and engineering processes [1-2]. Chemical sensors detect the presence and concentration of a specific chemical substance. The sensor films have the capability to detect the presence and concentration of a specific chemical substance. Such sensors achieve selectivity by detecting the interaction of the specific chemical substance with the sensor material through selective binding, adsorption and permeation of analyte [3]. Since the discovery almost 50 years ago that the absorption of a chemical substance on the surface of a semiconductor can cause a change in the electrical resistance of the material, there has been an effort to produce such conductometric chemical sensors. For example, detection of toxic and flammable gases is one of the most important applications of such gas sensors [4].

Various techniques have been investigated for thin film production with emphasis on reliability and cost. These techniques can be classified as physical and chemical methods. The physical methods include oxidation of an evaporated metal film, reactive/non-reactive sputtering techniques, laser ablation and molecular beam epitaxy. The chemical methods are divided into gas phase deposition (for example, chemical vapor deposition (CVD)) and solution techniques (for example, spray pyrolysis) [5]. The chemical techniques have been studied extensively for the preparation of thin films.

The present study uses the aerosol deposition method which is essentially a chemical spray pyrolysis (CSP) or spray pyrolysis technique (SPT). SPT was developed initially for the deposition of CdS and CdSe films [6]. It has since been used in glass industry and in solar cell production to deposit electrically conducting electrodes. Through this technique, dense and porous oxide films, ceramic coatings and powders can be prepared. It represents a very simple and relatively cost-effective method. Materials obtained by SPT find a wide range of applications in optoelectronic devices, anti-reflective coatings, sensors, etc. [7].

Figure 1-1 shows a schematic of the SPT experimental setup. The method typically involves a number of steps. A precursor solution which contains constituent elements of the compound is pulverized in the form of tiny droplets. The droplets spray onto a preheated substrate. Based on the thermal decomposition of precursor, a film of more stable compounds form and adhere to the heated substrate.

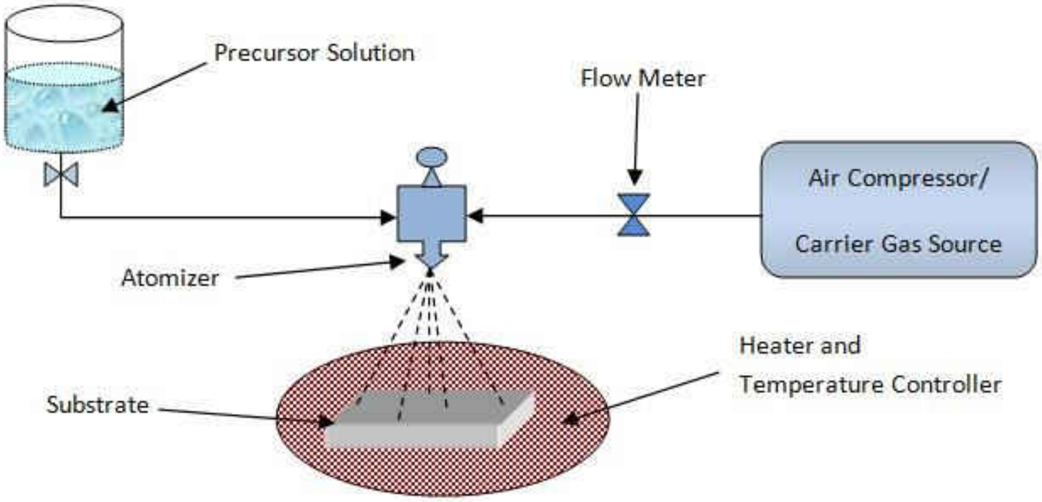

Figure 1-1 - The experimental setup of spray pyrolysis technique.

A comprehensive mathematical model of the aerosol formation is necessary to aid design of the experiment. The model developed starts with consideration of single droplet physics and the interaction with the surrounding flow and the heated substrate. In the next step, a system of droplets, forming a spray, is considered and modeled by a commercial computational fluid dynamics software (FLUENT [8]). The model uses numerical solution of the equations governing the transport of atomized droplets from the nozzle. A variety of processing parameters is investigated to provide fundamental understanding of the spray physics including particle size, particle velocity, thermal parameters and etc. This study focuses on the particle size and particle distribution which largely dictate the subsequent film microstructure and film properties.

The precise control of nanoparticle size homogeneity in the film is the key to achieving high sensing effect. In general, both the nanoparticle mean size and size distribution are influenced by the following: the chemical constituents, concentration and distribution of the nanoparticles, and synthesis conditions including substrate temperature, droplet size, droplet transport, and deposition rate. Therefore, the main goal of the growth modeling is to predict the particle and film growth rate and particle size distribution as a function of the above factors. Specifically, modeling will assist prediction of the particle size distribution on the substrate required to ensure structural and concentration homogeneity.

Another parameter to be considered is the composition of reactants both in the spray solution and in the droplets just before reaching the substrate. A complete reaction to form the oxides occurs only when the ratio of reacting materials in the sprayed solution is stoichiometric. Therefore, control of the particle size and composition just before impinging on the substrate is crucial to synthesis of a homogeneous film. The droplet characteristics are subject to change on impingement due to evaporation. Thus, the aerosol model considers the variety of synthesis parameters that affect particle size and size distribution in flight.

The results obtained are first checked for numerical accuracy through grid-independence tests. Then the model results from modeling are validated with available published data before being applied for the design of the spray deposition system for the physical experiment. Modeling also allows the input data from the experiment to be used to predict the film structure for direct comparison with the experimental data obtained from structural characterization studies.

The different components of the experimental apparatus are connected and controlled as an integrated system. The system can thus sustain the repeatability of experiments as well as assessment of the effect on the results of each parameter.

In this research, SPT is used to form metal oxides and mixed metal oxides thin films. Metal oxide-based gas sensors are chosen due to several inherent advantages [9-10] such as technology simplicity, inexpensive materials and process, small and moveable experimental apparatus size, high stability and fast response. In addition, mixed oxides are utilized in order to improve the sensor properties and benefit from the best sensing property of the different constituent oxides; the mixed oxides have used to form the thin film.

The films produced are characterized by a variety of methods. Structural characterization is the important link between materials synthesis, growth modeling, and simulation. In particular, the particle size and distribution in the films obtained are the important parameters that can be used to assess the accuracy of the mathematical model being developed. The following specific methods are used for film characterization:

- SEM (Scanning Electron Microscopy): for surface morphology, particle size and size distribution [11-12].
- XPS (X-ray Photoemission Spectroscopy), Raman Spectroscopy: for chemical composition [13].

A comparison of the results of simulation and experiments aids better understanding of film growth mechanism. In addition, finding the correlation between particle size and size distribution obtained from experiments, and the input spray parameters and substrate properties, will aid optimization of processing conditions for improved film growth. The specific objectives of the research are presented in the following section.

1.2 Objectives

The main objectives of this research are as follow:

a. Predict the *spray* parameters that determine growth characteristics of mixed metal oxide film (thickness and porosity). These parameters include particle size, droplet temperature and droplet velocity within the spray. A mathematical model is developed to simulate aerosol formation, stochastic motion of droplets, and interaction between droplets.

b. Model the effect of heated substrate on motion and solution characteristics of a *single droplet*, phase change inside droplet, and film growth on the substrate. The model utilizes spray data in (a) to simulate spray deposition and growth of mixed metal-oxide films from multicomponent precursor solution.

c. Design and construct an *experimental* spray deposition system guided by mathematical modeling. The system consists of customized spray system for generating droplets with specified sizes. The composition of the precursor solution and experimental conditions (substrate temperature and flight distance) are determined from the predicted spray parameters in (a).

d. Measure the *film characteristics* (such as size and size distribution of deposited particles, and chemical composition) using XRD, XPS, and SEM.

e. *Validate* mathematical model by comparison of experimental data with predictions. Specifically, the following parameters obtained from the measurements are compared with the predictions: droplet size distribution, temperature distribution, and velocity profile.

1.3 List of References

1. Fraden, J. (2004). Handbook of modern sensors: physics, designs, and applications. Springer.
2. Wilson, J. S. (2004). Sensor technology handbook. Elsevier.
3. Gründler, P. (2007). Chemical sensors: an introduction for scientists and engineers. Springer.
4. Zakrzewska, K. (2001). Mixed oxides as gas sensors. Thin solid films, 391(2), 229-238.

5. Perednis, D. (2003). Thin film deposition by spray pyrolysis and the application in solid oxide fuel cells. Doctoral dissertation, Swiss Federal Institute of Technology, Zurich.

6. George, J. *Preparation of Thin Films*; CRC Press: New York, 1992, 339-342.

7. Dedova, T. (2007). Chemical spray pyrolysis deposition of zinc sulfide thin films and zinc oxide nanostructured layers. Doctoral dissertation, Tallinn University of Technology, Estonia.

8. ANSYS FLUENT 12.0 User's Guide, www.ansys.com, April 2009.

9. Tofield, B. C. (1987). State of the art and future prospects for solid state gas sensors. *Solid state gas sensors, Eds. PT Moseley and BC Tofield,* Adam Hilger, Bristol, 198-237.

10. Ferro, R., Rodriguez, J. A., Jimenez, I., Cirera, A., Cerda, J., & Morante, J. R. (2005). Gas-sensing properties of sprayed films of $(CdO)_x$ $(ZnO)_{1-x}$ mixed oxide. *Sensors Journal, IEEE*, *5*(1), 48-52.

11. Basu, A., Haranath, D., Chander, H., & Chandra, S. (2004). Characterization of thin films of ZnO prepared by sol-gel processes. In *Eighteenth European Frequency and Time Forum* (Vol. 499, p. 87). Institution of Electrical Engineers.

12. Baykul, M. C., & Balcioglu, A. (2000). AFM and SEM studies of CdS thin films produced by an ultrasonic spray pyrolysis method. *Microelectronic Engineering*,*51*, 703-7

13. Deng, R., Yao, B., Li, Y. F., Zhao, Y. M., Li, B. H., Shan, C. X., Zhang, Z. Z., Zhao, D. X., Zhang, J. Y., Shen, D. Z., & Fan, X. W. (2009). X-ray photoelectron spectroscopy measurement of n-ZnO/p-NiO heterostructure valence-band offset. *Applied Physics Letters*, *94*(2), 022108-022108.

CHAPTER 2: LITERATURE REVIEW

2.1 Introduction

Various methods are used in industry to synthesize nanocomposite gas sensing films. These methods can be broadly classified as physical and chemical. Chemical spray pyrolysis (CSP) or spray pyrolysis technique (SPT) uses chemical reaction of compounds in a precursor solution to form desired film components. One of the most common materials that have extensive applications in gas sensors are metal oxides. Such materials exhibit relatively strong sensitivity to gas phase compounds; primarily due to the adsorption of oxide ions on the surface that enhance film conductivity. Nanoparticle size and size distribution are the parameters that largely determine the conductivity property of such films. These parameters can be measured by film characterization methods and controlled by managing the formation of the spray droplets.

2.2 Gas Sensor Technology

A gas sensor consists of a material whose physical properties, such as electrical or optical, can be changed in the presence of a gas. The change can then be measured to reflect the gas concentration. The microscopic chemical interactions are typically converted selectively into a measurable electrical signal. The selective and reversible sensing properties are the main requirements for these types of sensors [1].

Nanocrystalline metals are one of the simplest nanomaterial-based sensors. When a nanocrystalline metal is exposed to gas such as hydrogen, the electrical resistance of the metal may change. For example, hydrogen molecules can exhibit dissociative reactions at the surface and diffusive into nanocrystalline Palladium (Pd). The response to gas is faster when nanocrystalline materials are used instead of conventional micron-sized particles. This trend is attributed to the relatively smaller inter-particle spacing and gas diffusivity within particles in the former than the latter [2].

2.2.1 Metal Oxide Semiconductor Sensors

Gas sensors have traditionally been based on metal-oxide semiconductors. The main advantages of such sensors are [3]:

- Low cost,
- Technological simplicity,
- Small size,
- Ease of handling and
- Low power consumption

Thin film gas sensors have high performance, such as high stability and fast response. Simple metal oxides such as SnO_2, WO_3, ZnO and Fe_2O_3 are well known for their high sensitivity to changes in the surrounding gas atmosphere [4]. They, thus, play an important role in gas sensing applications.

The sensors are usually constructed as a porous sintered ceramic body which is heated between 300^0 C and 700^0 C. The sensing behavior is believed to be related to the adsorption of oxygen in the neck region between the grains. In the oxide layer, a positive space charge (depletion layer) develops as electrons transfer to the adsorbed oxygen. Meanwhile a negative charge accumulates on the surface of the film. Some of the O^{2-} ions can be removed from the surface by the reducing gas, creating a conduction path that increases the electrical conductivity of the film material [1]. One of the most common oxides is SnO_2 which is used for detecting H_2, CH_4 and CO_2 and operates at moderate temperatures (300^0 C to 400^0 C). These sensors are considered as surface sensors [4]. The properties of SnO_2 based sensors have been investigated comprehensively under different working conditions [5].

The sensing properties of some other metal oxides such as titanium oxide (TiO_2) are governed by another mechanism. Specifically in these materials, the bulk diffusion of defects determines the sensor response [4].

2.2.2 Need for Alternative Sensor Materials

Despite the high sensitivity of some of the metal oxide materials, they often demonstrate high resistivity which affects the performance of the sensor. For example, NO_2, which is an oxidizing gas, increases the resistance of a film because of the increase in the O^{2-} ions in n-type semiconductors[1] [6]. The sensing property of gas sensors are defined by four main factors [7]:

- Sensitivity: “The ratio of incremental change in the output of the sensor to its incremental change of the measured in the input”.
- Selectivity: “Ability to measure a single component in the presence of others”.
- Response time: “The time taken by a sensor to arrive at a stable value (a certain percentage of its final value, for instance 95%)”.

---

[1] N-type semiconductors are a type of semiconductors which the dopant atoms provide extra conduction electrons to the host material. It makes an excess of negative electron charge carriers. In contrast, a P-type semiconductor has an excess of free of charge carriers.

- Recovery time: “Defined in a similar way of response time, but conversely”.

The sensitivity of gas sensors can be increased by doping with noble metal[1] catalysts such as platinum, rhodium or palladium. These materials usually act as catalysts for adsorption of gases [4]. For example, Labeau et al. [8-9] investigated the effect of noble metals, such as Pt and Pd, on SnO_2 films. It was found that these metals acted as catalyst to decrease activation energy of surface reaction for CO and ethanol molecules. Therefore, the sensitivity of gas sensor increased. Cirera et Al. [10] investigated the effect of Pd doping on enhancement of CO-CH_4 selectivity for SnO_2 sensor. It was found that by increasing concentration of Pd up to 10% and distributed on all sensing layer, a decrease of resistance occurred. However the response of heavy catalyzed sensors produces zero sensitivity due to bulk and fast catalytic conversion of the gas.

2.2.3 Mixed Metal Oxide Films

Besides introducing dopants, another method to improve sensor performance is mixing metal oxides [11]. The mixed oxides have the potential to benefit from the best sensing properties of their pure components. The mixing of oxides modifies the electron structures which results in changes to both the bulk and surface properties.

---

[1] Noble metals: Metals those are resistant to corrosion and oxidation in moist air. They rarely can be found in the Earth’s crust and considered to be (in order of increasing atomic number): ruthenium (Ru), rhodium (Rh), palladium (Pd), silver (Ag), osmium (Os), iridium (Ir), platinum (Pt), and gold (Au). (In contrast, base metals, such as iron (Fe), nickel (Ni) and lead (Pb), oxides and corrodes easily).

These systems are usually categorized into three types:

- Compounds,
- Solid solutions,
- Neither (a) nor (b).

The first category takes advantage of forming distinct chemical compounds. For example, ZnO-SnO_2 forms $ZnSnO_3$ and Zn_2SnO_4. The $CdIn_2O_4$ that occurs in the CdO-In_2O_3 mixed system behaves as an active medium for CO. The second category consists of the mixed oxides that form solid solutions. For example, TiO_2-SnO_2 has such a behavior. The third category represents the materials which form neither compounds nor solid solutions, such as TiO_2-WO_3 [4].

Ferro et al. [3] investigated the effect of mixing CdO with ZnO. ZnO was the first metal oxide used for chemical sensors. It is mostly used to detect NO_2. However, ZnO thin films have high resistance. To enhance the film conductivity and modulate the sensing properties of ZnO, CdO is often mixed in adequate proportions. CdO films have low electrical resistivity. Therefore, a thin film with variable material proportions, $(CdO)_x(ZnO)_{1-x}$, has been investigated [3].

Vigil et al. [12] investigated $(ZnO)_x(CdO)_{1-x}$ mixed oxides, over a range of oxide proportions with a focus on the effect of post-thermal annealing on the film properties. It was demonstrated that the post-thermal annealing in air at 450^0 C enhances the structural perfection of the samples.

Moon et al. [13] examined the electrical conductivity and the sensing properties of $SnO_2 - TiO_2$. It was found that SnO_2 and TiO_2 metal oxides form a mixture when sintered at 800^0 C. The sensitivity of the mixture to hydrogen gas is higher than that of SnO_2. This increase in sensitivity is attributed to the increase in the surface area by adding 80% of TiO_2. The sensitivity of the mixed oxide to CO gas is however lower than the value obtained with SnO_2. When the mixture is coated with Cu, the selective detection to both CO and H_2 demonstrates significant improvement.

Correa-lozano et al. [14] studied the effect of preparation temperature on resistivity of the SnO_2-Sb_2O_5 films. It was figured out that the minimum resistivity occurred at 550^0 C. Also, it was shown that SPT method allowed more control on quantitative control comparing to Chemical Vapor Deposition (CVD) method.

Inoue et al [15] found that by introducing SiO_2 binding to WO_3 oxide sensors, the sensing behavior, such as stability and selectivity, to NO_2 gas was improved. Patil et al. [16] studied MoO_3 – WO_3 thin films. This mixture determines a very good electro-chromic behavior which can be used in large area display devices and smart windows[1].

A comprehensive study on different metal oxides and mixed oxide thin films and their synthesis has been undertaken [17].

2.3 Chemical Spray Pyrolysis Technique

The main step in the synthesis of modern gas sensors is the transfer from ceramic to thin film gas sensor (TFGS). Through this transfer, microminiaturization, cost reduction and energy consumption can be achieved. Therefore thin films are typically used to make gas sensitive micro sensors [5].

---

[1] The windows that control the amount of light and heat allowed passing through them.

Various methods are used for producing thin films. Kalantar-zadeh [7] introduced the following six classifications:

- Physical Vapor Deposition (PVD)
- Chemical Vapor Deposition (CVD)
- Liquid Phase Techniques
- Casting
- Sol-gel
- Nanolithography and Nano-Patterning.

These six methods can be summarized into two broad groups based on the nature of the deposition process, namely, physical and chemical methods. Figure 2-1 illustrates this broad classification [18].

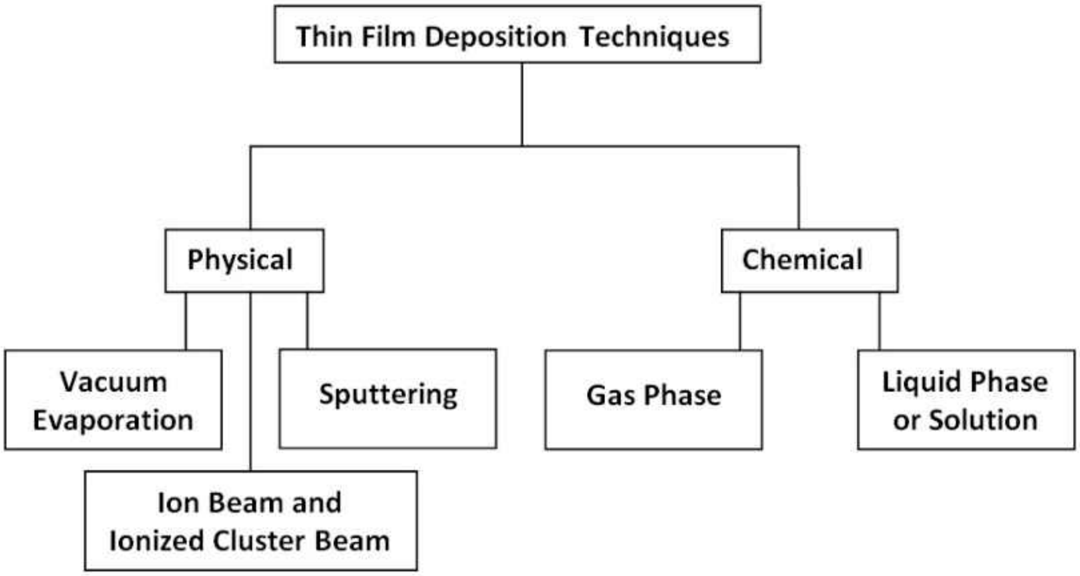

Figure 2-1 - Classification of thin film deposition.

Physical methods involve the techniques in which the deposition occurs after the material to be deposited has been transferred to a gaseous state. It can happen either by evaporation or an impact process. On the other hand, chemical methods can be described as thermal oxidation processes in which the substrate itself can be considered as the source for the constituent oxide. The reactants can be in either gaseous or liquid phase.

These methods of preparation lead to different properties of deposited thin film layers such as structural, optical and electrical properties. The deposition mechanism has strong influence on oxygen vacancies which serve as donors in oxide films. In general, physical methods results into deposition of other insulating phases, and subsequently relatively highly resistive films. On the other hand, chemical methods especially spray pyrolysis technique, leads to thin films without co-existence of other insulating phases. It results into films with relatively low resistivity [19]

Figure 2-2 summarizes different chemical deposition methods [20].

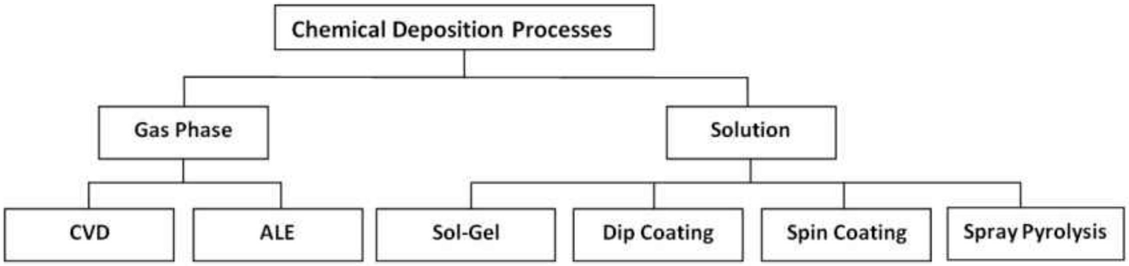

Figure 2-2 - Chemical thin film deposition methods.

Based on the phase of reactants to form the film, chemical deposition process can be categorized as gas phase or solution methods. Each method is briefly described below [7, 21]:

Chemical vapor deposition (CVD) is a popular technique in which a solid film on the substrate surface is formed as the constituents of the vapor phase reacts. LCVD (laser CVD) uses laser source to activate the chemical reaction.

Atomic Layer Epitaxy (ALE) is a method for producing thin film layers one atomic layer at a time by utilizing self-control based on saturating surface reactions. It is based on separate surface reactions between the growing surface and each of the components of the compound, one at a time.

Sol-Gel is defined as a colloidal suspension that will be gelled to form a solid. It includes the transition of a system from a liquid "sol" into a solid "gel" phase.

Spin coating involves four consequent steps: a) place a small volume of liquid on a surface; b) spin up the substrate to flow the liquid radially; c) let the excess liquid flow and leave the surface; and d) start evaporation to lead to solidification.

Dip Coating means the immersion of a substrate into a liquid, coating the material, removing the substrate and letting the excess liquid drain off.

The chemical method proposed for the present research is spray pyrolysis. It is also sometimes called chemical spray pyrolysis (CSP) [1] or simply spray pyrolysis technique (SPT). Spray pyrolysis is a processing technique used to prepare oxide films, ceramic coatings and powders. It has also been used for several years in glass industries and solar cell production.

Spray pyrolysis includes a thermally stimulated chemical reaction between fine droplets of different chemical species. In this technique, a solution containing soluble salts of the constituent atoms of the compound is sprayed on a heated surface as tiny droplets by a nozzle atomizer with help of a carrier gas. The droplets start pyrolytic decomposition to form a film on the substrate surface, when they reach the substrate. The hot surface maintains the required thermal energy for the decomposition and recombination. The carrier gas sometimes plays an active role in the pyrolytic process.

To spray the solution on the substrate, the following atomizers are usually used [20]:

- Airblast/Air assisted/Pressure swirl: Liquid is atomized by a stream of air;
- Ultrasonic: Ultrasonic frequencies are used to atomize the solution using short wave-lengths;
- Electrostatic: High electric fields cause droplet formation.

This technique has many advantages; some of which are listed below [1, 18, 20, 22]:

- Low cost (inexpensive apparatus);

- Does not require high quality targets or vacuum at any stage: a major advantage when scaled up for industrial applications;
- Simplicity and good productivity;
- Easy control of composition, deposition rate, film thickness and microstructure by changing the spray parameters. It eliminates the major problems of chemical methods such as sol-gel which produces films of limited thickness.
- Ease of doping virtually any material in any proportion by merely adding doping element to spray solution;
- Deposition possible at low or moderate temperatures (100^0 C to 500^0 C);
- Can produce films on less robust materials, with virtually no limitation on substrate material , dimension or the surface profile;
- Technological capability for mass production;
- Easy preparation of multi-layer films with composition gradient through the thickness by changing composition of the spray solution during the spray process;
- Produce uniform coatings on large area;
- Does not produce local overheating (Overheating may avoid materials to be deposited), unlike high-power methods such as radio frequency magnetron sputtering (RFMS);
- Offers opportunity to obtain reliable fundamental kinetic data because of well-formed film surfaces. The resulting films are quite compact, uniform without any side effects from substrate.

Despite the many advantages, there are also some disadvantages to this method including:

- Possibility of sulfide oxidation when processed in air atmosphere;
- Difficult to determine the growth temperature;
- Spray nozzle might get cluttered after long usage;
- Film quality highly dependent on droplet size and spray nozzle.

2.3.1 Design of Experimental Apparatus

To synthesis thin films using SPT, a precursor solution which contains constituent reactant compounds is atomized in the nozzle to tiny droplets. The droplets spray onto a preheated substrate. Based on the chemical reaction and thermal decomposition of the precursor, a film of more stable compounds form and adhere to the substrate. A simple spray pyrolysis system consists a spray nozzle, a furnace for heating the substrate, thermocouple (included temperature controller) and air compressor. To measure the flow of solution and air, liquid and air flow meters have been used (Fig. 2-3 [23]).

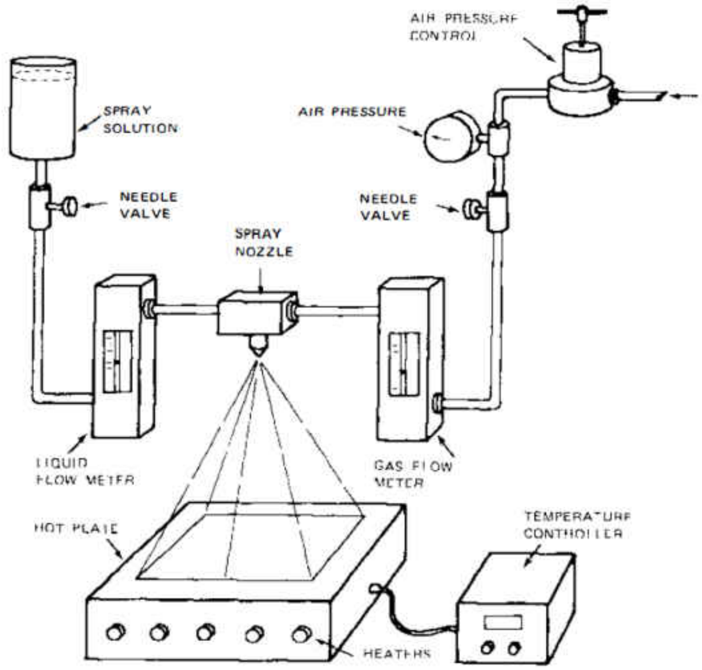

Figure 2-3 - Spray pyrolysis system.

The precise control of nanoparticle size homogeneity in the film is a key to achieving high sensitivity. The average size and size distribution of the particles can be estimated from the size of the atomized droplet and the concentration of the starting solution [24]. Particle size can be controlled through appropriate choice of the atomization method and parameters [17, 25].

Particle generation and distribution in the resulting film is a multi-stage process which is highly dependent among other things, on the initial solution atomization conditions, and the substrate temperature. Thus, the major issues that need to be addressed in the film synthesis are the type and composition of the starting solution, droplet generation, and particle morphology.

The reactants are typically dissolved in the solution with pre-determined stoichiometric ratio. Water or alcohol can be used as solvent [24]. The initial reactant concentration in the solution plays a significant role in determining the final particle size [27-27].

2.3.2 Component Specifications and Parameters

The experimental parameters are addressed in several previous technical papers. Each parameter value can be maintained in a specific range in order to produce metal oxide thin films efficiently. There are several parameters which control the size and shapes of nanostructures:

- Temperature on the substrate (T_{pyr}),
- Input pressure of the carrier gas (P_g),
- Solution volume (v_l),
- Construction of heating reactor,
- Distance between the nozzle and the substrate (L),
- Concentration of precursors in solution (C),
- Time of spraying (t_s), etc.

Changing any of these parameters leads to variation of film thickness and nanostructure crystallite size. Specifically, increasing the solution volume (v_l), and deposition temperature (T_{pyr}) generally leads to increase the film thickness. In contrast, a greater distance from the nozzle and the substrate (L) and higher carrier gas pressure (P_g) may cause to produce thinner film. To achieve minimum size of crystallites, a trade-off between low T_{pyr}, L, and P_g is necessary [28].

Based on these parameters, experimental setup is designed and each component is selected. It is important to consider that the droplets reaching the substrate are expected to still contain sufficient amount of solvent to produce smooth and dense film [22]. Thus the solvent in the initially formed tiny particles can be partially evaporated before reaching the substrate and still able to stick to the substrate [20].

It is necessary that the experimental system maintains the mentioned desired conditions. The most important controllable parameters are the ambient temperate, the substrate temperature, distance between the nozzle and the substrate and the solution mass flow rate.

2.4 Thin Film Processing

2.4.1 Film Growth Mechanism

2.4.1.1 Film Growth Stages

The quality of thin films by the SPT deposition method considered depends primarily on the substrate temperature and precursor solution concentration and to a lesser extent other parameters [25]:

a) Temperature: The substrate surface temperature is the most important parameter which determines film morphology, roughness, crystallinity, the stoichiometry of the film etc. High temperature also leads to large crystal size [29]. The film morphology can range from a cracked to a porous microstructure depending on the temperature [25, 30].

b) Precursor solution: The concentration of precursor solution is the second most important parameter which can modify the morphology of the thin films [25]. Increasing Solution concentration can increase film thickness and grain size [19]. In some cases, the grain size decreases with increasing film thickness when the roughness of the film decreases [31]. The volume of solution (or spray flow rate) also modifies the morphology of the film. A linear correlation has been found between volume of solution and film thickness. Precursor solution ageing has also been observed to have the opposite effect on the thickness of the film. When the time between preparation and spraying increases, the film thickness reduces. This result may be due to hydrolysis between the metal salt and water in the solution [28].

c) Other parameters: Other parameters have been found to have minor effect on the film synthesis but must be maintained in specific range in order to form the desired structure. For example, Korotcenkov et al. [28] showed that the film thickness increases when air pressure decreases. The result may be related to the decrease of spray flow velocity and increase of droplet sizes. It was also found that the film thickness can be decreased by increasing the distance between the nozzle and the substrate.

The process also involves a series of time constants which determines the properties of the deposited film. These characteristic times are highly dependent on the above mentioned control parameters. The reaction time (τ_{rxn}) and residence time of reaction (τ_{res}) are considered the most deterministic parameters. The reaction time is defined as $\tau_{rxn}=[C]_i/R_i$ where $[C]_i$ is the concentration of metal oxide species and R_i is the reaction rate of precursor. The residence time can be readily estimated by the time required for droplets to reach the boundary of the substrate [32]. Based on these parameters, different deposition regimes are expected in the SPT process as illustrated in Fig. 2-4 [25].

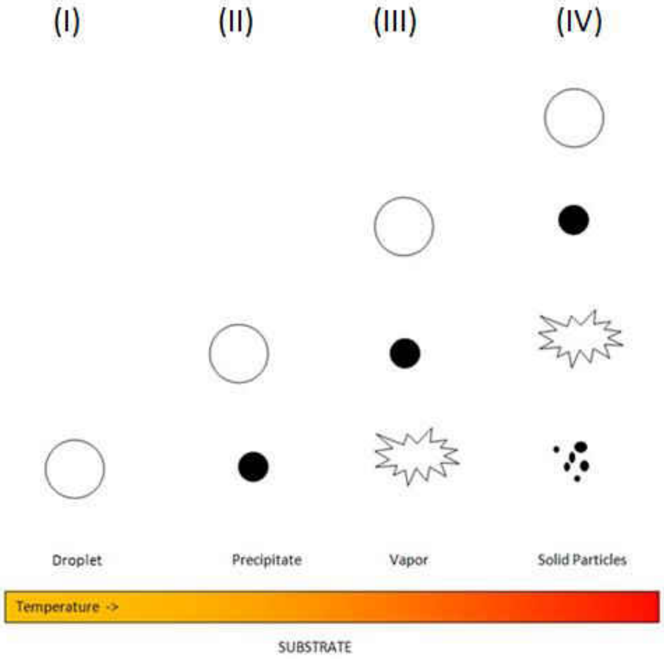

Figure 2-4 - Effect of heated substrate on a single droplet in a spray pyrolysis process.

At very low substrate temperature, the droplet has small residence time to initiate chemical reaction and therefore splashes onto the surface without any reaction (Regime I). By increasing the temperature, the droplets can reach the substrate as a precipitate and chemical reaction cannot be completed at this regime (Regime II). At higher temperatures of the substrate which is sufficient to initiate the chemical reaction (Regime III), the reaction rate increases and the solvent evaporates in flight. In this regime the reaction time is higher than the residence time and therefore the vapor reacts at the substrate. The deposition occurs on the substrate and a dense and smooth film can be deposited. This process is a vapor phase deposition process which is also used in chemical vapor deposition method (CVD) [33]. Increasing the flow rate at the same temperature further reduces the residence time resulting in a thicker film.

Increasing the residence time (e.g. by increasing the distance between spray nozzle and the surface) and decreasing the reaction time (e.g. by reducing the precursor concentration in the solvent or increasing the temperature), make these two time characteristics to be on the same order of magnitude. Therefore the chemical reaction can be initiated in some of the droplets in flight and a mixture of particles and vapor will be formed. This process will lead to the growth of columnar films on the surface (Regime III and IV together). The reaction time will be lower than residence time at much higher temperatures (Stage IV). This condition causes the formation of solid particles before reaching the surface in the gas phase. The deposited particles will eventually form granular film on the surface [32]. Increasing the concentration of the precursors at this level will decrease residence time and increase coalescences and subsequently increase particle sizes. This result is attributed to the complete evaporation of the solvent before the droplet hits the substrate [34].

Spray Pyrolysis Technique (SPT) can handle all these regimes by controlling the experimental parameters. On the other hand, vapor phase deposition (Regime III) is representing Chemical Vapor Deposition method (CVD) which is another common method to deposit metal oxides like ZnO [33]. In this process, the precursor is exposed on a heated substrate through inert gas and the film deposition is independent on direction which facilitates modeling formulation. Similarly, the solvent evaporates before the droplet hits the substrate and droplets reach the surface as vapor through controlled SPT with the specified surface temperature.

2.4.1.2 Chemical Reaction

The preparation of a metal oxide thin film depends on surface reaction (pyrolysis) of metal compounds, such as metal chlorides, on a heated substrate surface. The reaction type depends on the selection of the carrier gas and the solvent. By choosing air as carrier gas and water as the solvent, the general reaction equation can be stated as [35]:

$$\mathrm{MCl_x} + \mathrm{y\,H2O} \rightarrow \mathrm{MO_y} + \mathrm{x\,HCl} \tag{2-1}$$

where M is the host metal such as *Zn*, *Cd*, *In* etc. of the oxide films. The spray nozzle with the aim of the carrier gases performs the atomization of the chemical solution into aerosols. The temperature of the substrate is fixed at a constant value by using a temperature controlled furnace or hot plate. In general, the films grown at a substrate temperature less than a specific value, depending on metal oxide type, are amorphous in nature. It is needed to apply higher temperatures or perform post annealing treatment to get polycrystalline films. The film formation depends upon the droplet landing, reaction and solvent evaporation, which relates to the droplet size. When the droplet approaches the substrate just before the solvent is completely removed, that is the ideal condition for the preparation of the film.

To produce mixed metal oxides, the similar approach can be addressed. A dilute solution consists of two metal compounds, such as metal chlorides or acetates[1] [12] which are miscible, is produced. The produced aqueous solution is sprayed on the hot substrate to maintain chemical pyrolysis.

---

[1] Acetate is a salt or ester of acetic acid, containing the anion CH3COO− or the group -OOCCH3.

2.4.1.3 Thin Film Properties

The main purpose of deposition of metal oxide on the target substrate is growing a thin film on it. The thin film is characterized by the thickness and particles shape and arrangement. The term thin film is used when these particles are classified as nanostructures. Nanostructures can be introduced as structures designed on atomic or molecular scale in which at least one dimension is measured in nanometers (1-100 *nm*). Since they have small size of building blocks (particle, grain or layer) and high surface to volume ratio, significant increase in grain boundary area, these materials are expected to demonstrate unique mechanical, optical, electronic, and magnetic properties [22]. Therefore, the interest in these materials has been increased. The main effort of researchers is focusing on the production of these structures with desired size and shapes. Figure 2-5 shows a few typical growth morphologies of ZnO nanostructures including nanowires, nanorods, nanotubes and nanobelts [22].

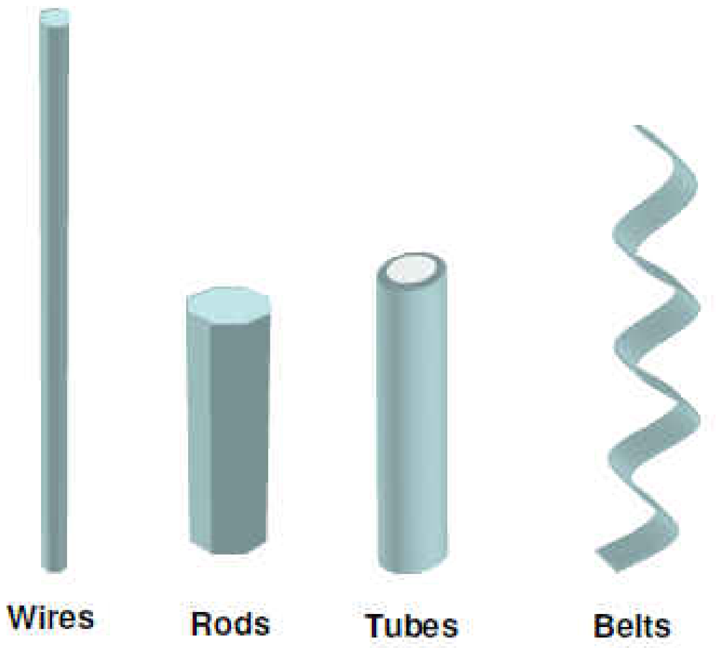

Figure 2-5 - Different morphologies of hexagonal ZnO nanostructures.

2.4.2 Deposition of Single and Mixed Oxides

The objective of this research is to investigate the effect of synthesis conditions (specifically, substrate temperature and precursor concentration) on the structure of ZnO, SnO_2, $ZnO+In_2O_3$ and $SnO_2+In_2O_3$ thin films produced by SPT.

Several studies have considered the deposition of ZnO films. A study on the effect of post annealing on the properties of ZnO films shows that annealing enhances the quality of film by removing structural defects through agglomeration of small particles. The results indicated that post–thermal annealing could enhance the structural quality in general [12, 29]. A similar approach has been used to synthesize ZnS and ZnO thin films, and study the growth mechanism and film characteristics (such as structure and crystalline properties) as a function of temperature, solution composition and concentration [22]. The effect of temperature on ZnO film structure has also been investigated, indicating that such films could be crystallized better at substrate temperatures above 400° C [36].

The influence of deposition parameters on SnO_2 thin film characteristics has demonstrated that SPT could be used to produce nano-scale films for gas sensing applications [28]. The electrical and structural properties of SnO_2 films deposited by SPT also show improvement of crystal growth at high temperatures (above 450° C) [37].

Mixing of metal oxides in a sensor film has recently been explored to improve sensor performance and thermal stability. The mixed oxides have the potential to benefit from the best sensing properties of their pure components. As it is mentioned before, the electronic structures of the oxides are modified, resulting in change to both the bulk and surface properties [11].

Some research studies have investigated the properties of indium-doped ZnO nanofiber thin films by SPT, using temperatures between 350° C and 500° C for film deposition and 500° C for annealing. The results indicate a decrease in grain size with increasing temperature [38-39].

Similar studies have investigated the effect of deposition parameters on the characteristics of indium-doped SnO_2 films as well as ZnO. The studies used low temperature (380° C) for deposition of zinc-indium oxides and higher temperature (450° C) for tin-indium oxides at ambient atmosphere [40].

Two primary synthesis parameters controlling the structure of films produced by SPT are the substrate temperature and the concentration of precursors in solution. Although several studies have considered the effect of substrate temperature and solution concentration on the structure of metal oxide films [41], there is a lack of systematic investigation of the effect of temperature on different oxides synthesized by SPT under similar controlled conditions. This issue is addressed in the present study by maintaining constant values of some process parameters (e.g. spray nozzle diameter, spray velocity, and distance between spray nozzle and substrate), while varying the temperature. In addition, the effect of precursor concentration is similarly investigated.

2.4.3 Effect on Sensor properties

A number of studies have shown that one promising approach to improve conductometric metal oxide sensors is to utilize semiconducting nanostructured composite materials consisting of metal oxides with different electronic structure and chemical properties [42-44]. It has been established that using a mixture of metal oxides, the resulting composite sensor material can achieve selectivity and sensitivity for gas detection in air ambience that far exceed those achievable with the individual constituent metal oxides of the composite [45-49].

Studies of sensory phenomena in metal oxide composites have shown that there are certain optimum compositions for which these effects reach maximum values [46-47]. One of the important factors that determine the dependence of sensory phenomena in metal oxide composites on composition is the effect of composition on the morphology of the sensor film. Therefore, it is important to clarify the morphological features of the composite sensors that exhibit high sensitivity. These features depend on the nature of the components of the mixed metal oxide composite and the processing conditions.

2.5 Mathematical Models

The film property depends crucially on the film microstructure, which in turn is determined largely by the synthesis. The objective of this section is to investigate by means of mathematical modeling the effect of synthesis conditions on the droplets produced by the aerosol technique.

2.5.1 Spray Modeling

The mathematical model involves numerical solution of the equations governing the transport of atomized droplets from the nozzle to predict the droplet characteristics in the spray prior to impingement on the substrate. This information is used to model evaporation and chemical reaction on the substrate to produce the oxide particles, as well as oxide particle size distribution and film growth. A complete reaction occurs only when the ratio of reacting materials in the sprayed solution is stoichiometric. Therefore, control of the particle size and composition just before impingement on the substrate is crucial to the synthesis of film with optimal oxide particle size distribution and sensitivity.

There are several studies of spray modeling which includes different steps such as solution evaporation modeling and nanoparticle formation process.

Spray modeling studies often consider various stages of the process including solution evaporation and nanoparticle formation.

Semiao et al. [50] simplified the equations of droplet size distribution in sprays. The study considered two types of atomizers (pressure jet atomizers and airblast atomizers).

Lim et al. [51], Jiang et al. [52], and Yu and Liao [53] simulated the liquid aerosol evaporation and verified the results with the results with experimental data. The velocity, droplet temperature and size distribution were investigated. The focus was on the effect of types of liquids in aerosol and initial conditions on droplet specification.

Eslamian et al. [54] performed CFD simulation to determine necessary solute concentration and droplet size distribution on during aerosol pyrolysis process. The formulation considered different parameters such as droplet and wall temperate. Jayanthi et al. [55] studied particle formation during aerosol thermolysis. The model investigated the effect of solute properties, ambient temperature, initial solute concentration and initial droplet radius on particle formation process.

2.5.2 Droplet Evaporation Modeling

Droplet impingement on heated substrate has been a subject of intense investigation in recent years [56]. However, a number of issues are still not fully addressed including the conditions that lead to maximum droplet spread without rebound, the mechanisms correlating heat transfer with contact line dynamics, and the partitioning of energy between single- and two-phase zones. In order to understand the fundamental mechanisms responsible for wetting and two-phase mass and heat transfer during spray deposition of droplet on a heated surface, a detailed study of single droplet dynamics is essential. The objective of this section is to develop a comprehensive mathematical model of transport and chemical reaction phenomena in a single droplet deposited on a heated substrate. The ultimate goal is to utilize the results in a spray-deposition model for the synthesis of mixed-oxide composite film for sensor application.

Droplet impingement on a hot surface is relevant to a variety of practical applications, including surface cooling through spray, mist and electrowetting [57-58]. In the cooling methods, coolant droplets are applied to absorb heat from the surface. In such cases, the goal is to make the surface as wet as possible. Previous studies of this problem have focused on evaporation rate and wetting properties [59]. The contact angle and contact lines are subject to change during the impingement and evaporation processes. The variation of contact angle has been widely investigated and formulated in relation to the surface energy [59]. Hu et al. [60] investigated the evaporation of a droplet on a surface and derived the formulation of variation of height and contact line with respect to the contact angle. Figure 2-6 [61] shows a schematic representation of droplet shape variation during this process. This figure indicates that droplet contact line and contact angle gradually decrease due to evaporation.

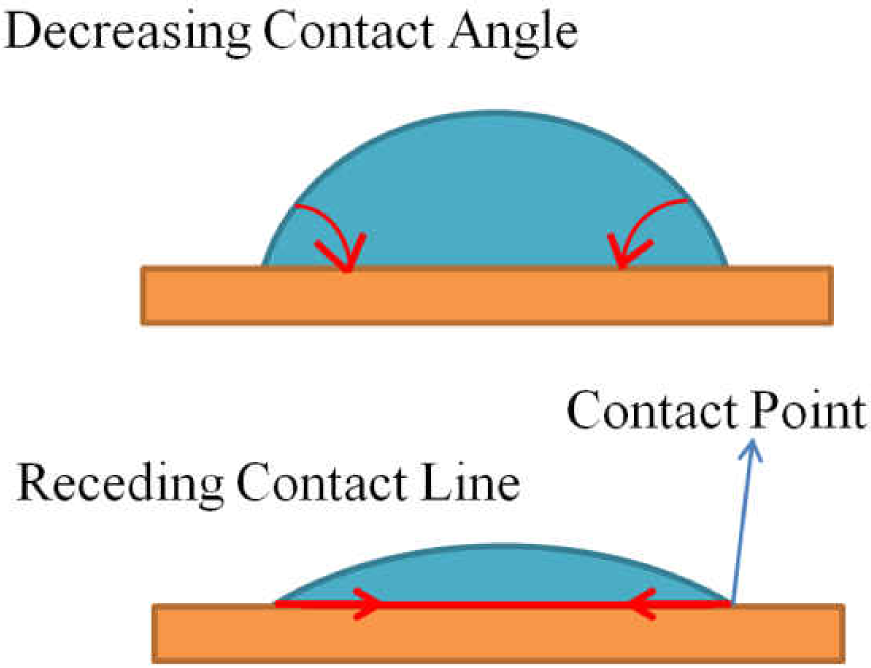

Figure 2-6 - Schematic sketch of droplet evaporation process.

There are other applications which demand minimum surface wetting and maximum evaporation rate on a surface. At very low temperature, the droplet splashes onto the surface and decomposes. At higher temperatures, the solvent evaporates during flight and dry precipitate reaches the substrate, where decomposition occurs. At much higher temperatures, the solvent evaporates before the droplet hits the substrate [25]. This situation occurs when the surface is very hot and able to initiate chemical reaction between the precursors in the droplet solution. A typical example is the spray pyrolysis process which is of interest in this study. This deposition method is based on surface reaction in droplets that still contain enough solution after reaching the surface.

A number of studies have been done on droplet impingement and evaporation on a flat surface. Most of these studies focus on low temperature deposition or single component droplets [62-63]. There are also studies that consider evaporation of multi-component droplets but without chemical reaction [64-65]. However, spray pyrolysis which is of interest here typically involves surfaces at high temperatures. In addition, the components in the droplet solution affect the dynamics and the evaporation process. Therefore, the purpose of this study is to understand the behavior of a multi-component droplet impinging on a hot substrate while undergoing evaporation and chemical reaction. The mathematical model developed is solved using the FLUENT commercial code [66].

2.5.3 Comprehensive Film Growth Model

SPT is a solution based method [67] utilizing thermal deposition of a metal precursor. It involves primarily four stages:

i. Atomization

ii. Evaporation

iii. Decomposition/Reaction

iv. Deposition

Figure 2-7 represents the approach used to cover all of these 4 stages.

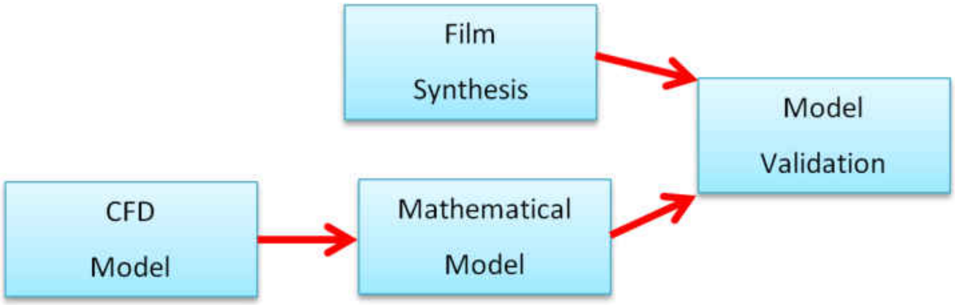

Figure 2-7 - Modeling and experimental approach.

The parameters associated to each stage are described in Fig. 2-8.

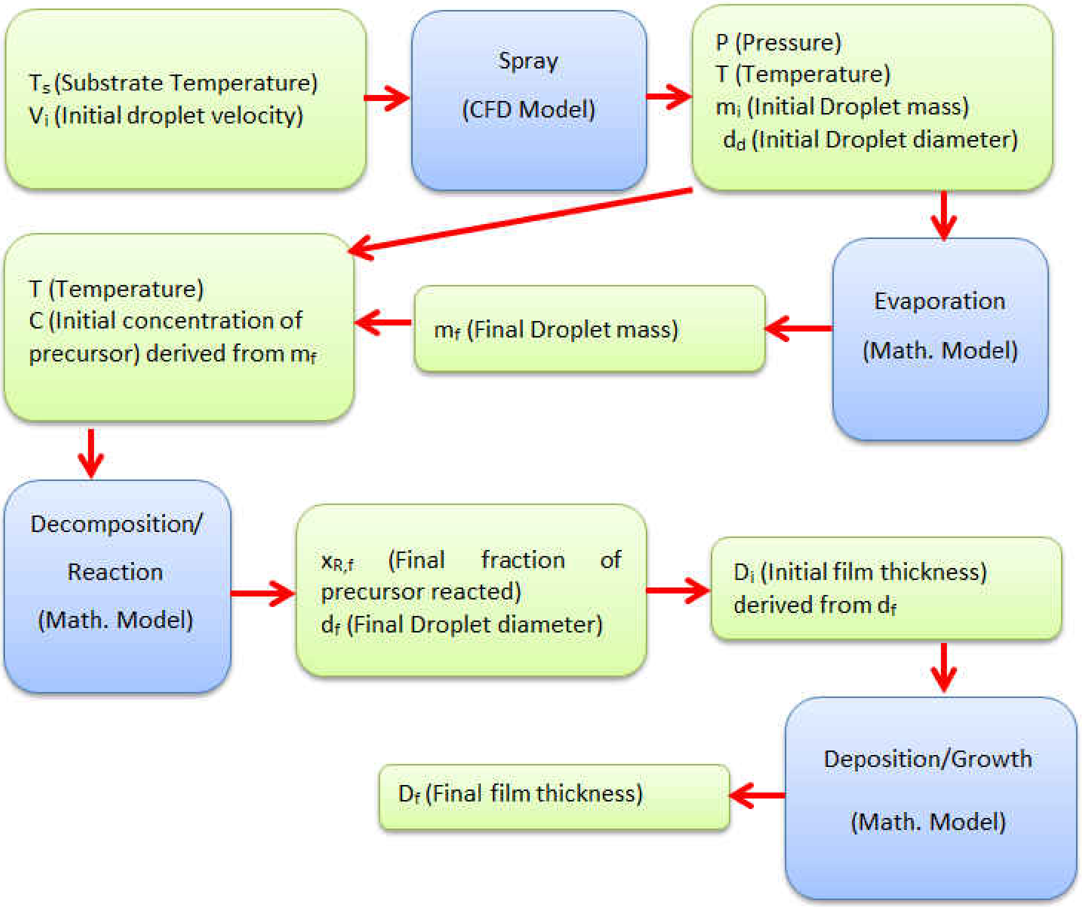

Figure 2-8 - Spray pyrolysis process models.

The synthesized film is typically composed of mixtures of electron donors (e.g. In_2O_3) and electron acceptors (e.g. ZnO, SnO_2). In order to synthesize the film with the desired properties, the morphology of the film must be controlled and largely predictable. The objective of this research is to develop a model for systematic investigation of the processes involved in mixed metal oxide deposition by SPT in order to predict the film morphology.

Several approaches have been used to develop mathematical methods of the process. One approach involves descriptive models which mostly consider the physics of the process.

Different spray methods and the deposition stages were studied by using this approach [25] and a conceptual model of the process was developed in previous study [68].

Computational Fluid Dynamics (CFD) approach has been applied to study SPT deposition process in previous studies. Evaporation and drying for SPT was modeled and validated with the deposition of different materials [69]. CFD was used to model spray droplets and the effect of heated environment on droplet characteristics [70]. A similar model was developed to investigate the evaporation phenomena in ethanol-NaCl-water droplet in [71].

Modeling the reaction and the film growth has been considered in some recent studies. These studies considered the variation of concentration within the droplets by defining the characteristic time constants. A model which includes the evaporation and reaction stages was developed and validated for deposition of TiO_2 nano particles in [72]. The atomization and decomposition processes were also considered. Droplet transport and interaction between droplets was assumed as chemical vapor deposition phenomena in [73]. In this study, the precursor was exposed to a heated substrate through inert gas and the film deposition was independent of direction, which facilitated model formulation. The model was validated by experimental results from deposition of tin chloride on silicon wafer substrate.

Considering that the flow rates of gas and precursor in both CVD and SPT methods can be controlled [74] for the same range of temperature [75], a novel approach is proposed in this research to model the deposition of metal oxide thin films. Specifically, SPT and CVD can be assumed to be analogous when the solvent evaporates before the droplet hits the substrate, and subsequently reaches the surface in the vapor phase. The temperature of the substrate is considered at the range for which columnar film is expected to grow. This temperature permits the assumption that the residence and reaction times are on the same order.

In summary, mathematical models developed in this research, provide a cost-effective mean to guide mixed metal oxide deposition experiments. The aerosol model presents here examines the variety of synthesis parameters that affect droplet size and size distribution in flight. This research uses mathematical modeling to investigate the effect of solution mass flow rate and swirl velocity on droplet size and distribution. The results of such a study are used to guide placement of substrate for optimal film growth and film properties. In addition, the droplet characteristics are subject to change on impingement due to evaporation.

In spite of the advances that have been made in understanding spray pyrolysis, very limited studies have involved the formation mixed oxide films. Specifically, there is still a need to develop a comprehensive mathematical model which considers not only solution atomization through spray nozzle but also the formation of mixed metal oxide thin film on a heated substrate. This model needs to be developed by studying the interaction and combination of deposition stages and validated by experimental studies.

2.6 Conclusion

The spray pyrolysis technique has numerous advantages that outweighs the disadvantages and make it an ideal choice for the present research. The spray method has different classifications. The pressurized spray method (PSM) has been chosen for the present study due to its relative simplicity and ease of synthesizing mixed oxides merely by changing the precursors. The technique will be used to provide mixed-oxide films on which there have been relatively few published studies. A novel and comprehensive model is also required to investigate systematically the process of mixed metal oxide deposition by SPT. This model should be able to predict the film characteristics and morphology based on processing parameters.

2.7 List of References

1. Kruis, F. E., Fissan, H., & Peled, A. (1998). Synthesis of nanoparticles in the gas phase for electronic, optical and magnetic applications—a review. *Journal of Aerosol Science*, *29*(5), 511-535.
2. Volkening, F. A., Naidoo, M. N., Candela, G. A., Holtz, R. L., & Provenzano, V. (1995). Characterization of nanocrystalline palladium for solid state gas sensor applications. *Nanostructured materials*, *5*(3), 373-382.
3. Ferro, R., Rodriguez, J. A., Jimenez, I., Cirera, A., Cerda, J., & Morante, J. R. (2005). Gas-sensing properties of sprayed films of $(CdO)_x$ $(ZnO)_{1-x}$ mixed oxide. *Sensors Journal, IEEE*, *5*(1), 48-52.
4. Zakrzewska, K. (2001). Mixed oxides as gas sensors. Thin solid films, 391(2), 229-238.
5. Korotchenkov, G., Brynzari, V., & Dmitriev, S. (1999). SnO_2 films for thin film gas sensor design. *Materials Science and Engineering: B*, *63*(3), 195-204.
6. Ferro, R., Rodriguez, J. A., & Bertrand, P. (2005). Development and characterization of a sprayed ZnO thin film-based NO2 sensor. *physica status solidi (c)*, *2*(10), 3754-3757.
7. K. Kalantar-zadeh, K., & Fry, B. (2007). *Nanotechnology-enabled sensors*. Springer, New York.
8. Labeau, M., Gautheron, B., Cellier, F., Vallet-Regi, M., Garcia, E., & Carbet, J. M. (1993). Pt Nanoparticles Dispersed on SnO_2 Thin Films: A Microstructural Study. *Journal of Solid State Chemistry*, *102*(2), 434-439.
9. Labeau, M., Gas'Kov, A. M., Gautheron, B., & Senateur, J. P. (1994). Synthesis of Pd-doped SnO_2 films on silicon and interaction with ethanol and CO. *Thin Solid Films*, *248*(1), 6-11.

10. Cirera, A., Cabot, A., Cornet, A., & Morante, J. R. (2001). CO–CH_4 selectivity enhancement by in situ Pd-catalysed microwave SnO_2 nanoparticles for gas detectors using active filter. *Sensors and Actuators B: Chemical*, *78*(1), 151-160.

11. Bai, S., Li, D., Han, D., Luo, R., Chen, A., & Chung, C. L. (2010). Preparation, characterization of WO_3–SnO_2 nanocomposites and their sensing properties for NO_2. *Sensors and Actuators B: Chemical*, *150*(2), 749-755.

12. Vigil, O., Cruz, F., Santana, G., Vaillant, L., Morales-Acevedo, A., & Contreras-Puente, G. (2000). Influence of post-thermal annealing on the properties of sprayed cadmium–zinc oxide thin films. *Applied surface science*, *161*(1), 27-34.

13. Moon, W. J., Yu, J. H., & Choi, G. M. (2004). Selective gas detection of SnO_2-TiO_2 gas sensors. *Journal of electroceramics*, *13*(1-3), 707-713.

14. Correa-Lozano, B., Comninellis, C., & De Battisti, A. (1996). Preparation of SnO_2-Sb_2O_5 films by the spray pyrolysis technique. *Journal of applied electrochemistry*, *26*(1), 83-89.

15. Inoue, T., Ohtsuka, K., Yoshida, Y., Matsuura, Y., & Kajiyama, Y. (1995). Metal oxide semiconductor NO_2 sensor. *Sensors and Actuators B: Chemical*, *25*(1), 388-391.

16. Patil, P. R., & Patil, P. S. (2001). Preparation of mixed oxide MoO_3-WO_3 thin films by spray pyrolysis technique and their characterisation. *Thin Solid Films*, *382*(1), 13-22.

17. Patil, P. S. (1999). Versatility of chemical spray pyrolysis technique. *Materials Chemistry and physics*, *59*(3), 185-198.

18. George, J. (1992). Preparation of thin films. CRC Press, New York.

19. Patil, P. S., Kawar, R. K., Sadale, S. B., & Chigare, P. S. (2003). Properties of spray deposited tin oxide thin films derived from tri-n-butyltin acetate. *Thin Solid Films*, *437*(1), 34-44.

20. Perednis, D. (2003). Thin film deposition by spray pyrolysis and the application in solid oxide fuel cells. Doctoral dissertation, Swiss Federal Institute of Technology, Zurich.

21. Pakkala, A. (2012). EL Displays Based on ALE Grown Phosphors and Insulator Thin Films. *white paper, Planar International Ltd. http://www. planar. com/support/design-resources/docs/alephosph. pdf, accessed*, *20*.

22. Dedova T. (2007). Chemical spray pyrolysis deposition of zinc sulfide thin films and zinc oxide nanostructured layers. Doctoral dissertation, Tallinn University of Technology, Estonia.

23. Mooney, J. B., & Radding, S. B. (1982). Spray pyrolysis processing. *Annual review of materials science*, *12*(1), 81-101.

24. Okuyama, K., & Wuled Lenggoro, I. (2003). Preparation of nanoparticles via spray route. *Chemical Engineering Science*, *58*(3), 537-547.

25. Perednis, D., & Gauckler, L. J. (2005). Thin film deposition using spray pyrolysis. *Journal of Electroceramics*, *14*(2), 103-111.

26. Ko, J. W., Yoo, J., Kim, Y. K., Chung, K. C., Chung, H., & Yoo, S. I. (2005). Fabrication of fine and homogeneous MgB 2 nano powders by spray pyrolysis. *Applied Superconductivity, IEEE Transactions on*, *15*(2), 3349-3351.

27. Kang, Y. C., Chung, Y. S., & Park, S. B. (1999). Preparation of YAG: Europium Red Phosphors by Spray Pyrolysis Using a Filter-Expansion Aerosol Generator. *Journal of the American Ceramic Society*, *82*(8), 2056-2060.

28. Korotcenkov, G., Brinzari, V., Schwank, J., DiBattista, M., & Vasiliev, A. (2001). Peculiarities of SnO_2 thin film deposition by spray pyrolysis for gas sensor application. *Sensors and Actuators B: Chemical*, *77*(1), 244-252.

29. Nehru, L. C., Umadevi, M., & Sanjeeviraja, C. (2012). Studies on structural, optical and electrical properties of ZnO thin films prepared by the spray pyrolysis method. *International Journal of Materials Engineering*, *2*(1), 12-17.

30. Ayouchi, R., Martin, F., Leinen, D., & Ramos-Barrado, J. R. (2003). Growth of pure ZnO thin films prepared by chemical spray pyrolysis on silicon. *Journal of crystal growth*, *247*(3), 497-504.

31. Godbole, B., Badera, N., Shrivastava, S., Jain, D., & Ganesan, V. (2011). Growth mechanism of ZnO films deposited by spray pyrolysis technique. *Materials Sciences and Applications*, *2*, 643.

32. An, W. J., Thimsen, E., & Biswas, P. (2009). Aerosol-chemical vapor deposition method for synthesis of nanostructured metal oxide thin films with controlled morphology. *The Journal of Physical Chemistry Letters*, *1*(1), 249-253.

33. Zunke, I., Heft, A., Schäfer, P., Haidu, F., Lehmann, D., Grünler, B., ... & Zahn, D. R. T. (2013). Conductive zinc oxide thin film coatings by combustion chemical vapour deposition at atmospheric pressure. Thin Solid Films, 532, 50-55.

34. Khatami, S. M. N., Ilegbusi, O. J. (2012, November). Droplet Evaporation and Chemical Reaction in a Single Multi-Component Droplet to Synthesis Mixed-Oxide Film Using Spray Pyrolysis Method. In: *ASME 2012 International Mechanical Engineering Congress and Exposition* (pp. 633-638). American Society of Mechanical Engineers.

35. Godbole, B., Badera, N., Shrivastav, S. B., & Ganesan, V. (2009). A simple chemical spray pyrolysis apparatus for thin film preparation. *Jl. of Instrum. Soc. of India*, *39*(1), 42-45.

36. Zahedi, F., Dariani, R. S., & Rozati, S. M. (2013). Effect of substrate temperature on the properties of ZnO thin films prepared by spray pyrolysis. *Materials Science in Semiconductor Processing*, *16*(2), 245-249.

37. Ikhmayies, S. J., & Ahmad-Bitar, R. N. (2009). Effect of the substrate temperature on the electrical and structural properties of spray-deposited SnO_2: F thin films. *Materials Science in Semiconductor Processing*, *12*(3), 122-125.

38. Ilican, S., Caglar, Y., Caglar, M., & Yakuphanoglu, F. (2006). Electrical conductivity, optical and structural properties of indium-doped ZnO nanofiber thin film deposited by spray pyrolysis method. *Physica E: Low-dimensional Systems and Nanostructures*, *35*(1), 131-138.

39. Rozati, S. M., Zarenejad, F., & Memarian, N. (2011). Study on physical properties of indium-doped zinc oxide deposited by spray pyrolysis technique. *Thin Solid Films*, *520*(4), 1259-1262.

40. Wienke, J., & Booij, A. S. (2013). Spray deposition of oxides at ambient atmosphere Part 1: Transparent Conductive oxides. *Solar Energy*, *2012*, 2011.

41. Bagheri Khatibani, A., & Rozati, S. M. (2013). Synthesis and characterization of amorphous aluminum oxide thin films prepared by spray pyrolysis: Effects of substrate temperature. *Journal of Non-Crystalline Solids*, *363*, 121-133.

42. Trakhtenberg L.I., Gerasimov G.N., Gromov V.F., Kozhushner M.A., & Ilegbusi O.J. (2012) Experimental Investigations and Modeling of Gas Sensing Effect in Mixed Metal oxide nanocomposites. in: *Chemical Sensors: Simulation and Modeling, Ed. G. Korotcenkov*, Momentum Press: New York, pp. 261-296.

43. De Lacy Costello, B. P. J., Ewen, R. J., Ratcliffe, N. M., & Sivanand, P. S. (2003). Thick film organic vapour sensors based on binary mixtures of metal oxides. *Sensors and Actuators B: Chemical*, *92*(1), 159-166.

44. Comini, E., Ferroni, M., Guidi, V., Faglia, G., Martinelli, G., & Sberveglieri, G. (2002). Nanostructured mixed oxides compounds for gas sensing applications. *Sensors and Actuators B: Chemical*, *84*(1), 26-32.

45. Kim, K. W., Cho, P. S., Kim, S. J., Lee, J. H., Kang, C. Y., Kim, J. S., & Yoon, S. J. (2007). The selective detection of C_2H_5OH using SnO_2-ZnO thin film gas sensors prepared by combinatorial solution deposition. *Sensors & Actuators: B. Chemical*, *123*(1), 318-324.

46. Trakhtenberg, L. I., Gerasimov, G. N., Gromov, V. F., Belysheva, T. V., & Ilegbusi, O. J. (2012). Effect of composition on sensing properties of $SnO_2 + In_2O_3$ mixed nanostructured films. *Sensors and Actuators B: Chemical*, *169*, 32-38.

47. Trakhtenberg, L. I., Gerasimov, G. N., Gromov, V. F., Belysheva, T. V., & Ilegbusi, O. J. (2012). Effect of composition on sensing properties of $SnO_2 + In_2O_3$ mixed nanostructured films. *Sensors and Actuators B: Chemical*, *169*, 32-38.

48. Moon, W. J., Yu, J. H., & Choi, G. M. (2002). The CO and H_2 gas selectivity of CuO-doped SnO_2–ZnO composite gas sensor. *Sensors and Actuators B: Chemical*, *87*(3), 464-470.

49. Neri, G., Bonavita, A., Micali, G., Rizzo, G., Pinna, N., Niederberger, M., & Ba, J. (2008). Effect of the chemical composition on the sensing properties of In_2O_3+SnO_2 nanoparticles synthesized by a non-aqueous method. *Sensors and Actuators B: Chemical*, *130*(1), 222-230.

50. Semião, V., Andrade, P., & Carvalho, M. D. G. (1996). Spray characterization: numerical prediction of Sauter mean diameter and droplet size distribution. *Fuel*, *75*(15), 1707-1714.

51. Lim, E. W. C., Heng Koh, S., Kuang Lim, L., Hoon Ore, S., Kiat Tay, B., Ma, Y., & Wang, C. H. (2008). Experimental and computational studies of liquid aerosol evaporation. *Journal of Aerosol Science*, *39*(7), 618-634.

52. Jiang, X., Ward, T. L., Swol, F. V., & Brinker, C. J. (2010). Numerical Simulation of Ethanol− Water− NaCl Droplet Evaporation. *Industrial & Engineering Chemistry Research*, *49*(12), 5631-5643.

53. Yu, H. F., & Liao, W. H. (1998). Evaporation of solution droplets in spray pyrolysis. *International journal of heat and mass transfer*, *41*(8), 993-1001.

54. Eslamian, M., Ahmed, M., & Ashgriz, N. (2006). Modelling of nanoparticle formation during spray pyrolysis. *Nanotechnology*, *17*(6), 1674.

55. Jayanthi, G. V., Zhang, S. C., & Messing, G. L. (1993). Modeling of solid particle formation during solution aerosol thermolysis: the evaporation stage. *Aerosol Science and Technology*, *19*(4), 478-490.

56. Annapragada, S. R., Dash, S., Garimella, S. V. and Murthy, J. Y. (2011). Dynamics of droplet motion under electrowetting actuation. *Langmuir*, *27*(13), pp. 8198-8204.

57. Bahadur, V. and Garimella, S. V. (2006). An energy-based model for electrowetting-induced droplet actuation. *Journal of Micromechanics and Microengineering*, *16*(8), 1494.

58. Wang, T., Gaddis, J. L. and Li, X. (2005). Mist/steam heat transfer of multiple rows of impinging jets. *International Journal of Heat and Mass Transfer*, *48*(25), pp. 5179-5191.

59. Lok, B. K. and Hu, X. (2010, December). Transient contact angle of evaporating inkjet droplet on trans-parent polymer substrate. In: *Electronics Packaging Technology Conference (EPTC), 2010 12th*, pp. 240-245.

60. Hu, H. and Larson, R. G. (2002). Evaporation of a sessile droplet on a substrate. *The Journal of Physical Chemistry B*, *106*(6), pp. 1334-1344.

61. Hu, H. and Larson, R. G. (2005). Analysis of the microfluid flow in an evaporating sessile droplet. *Langmuir*, *21*(9), pp. 3963-3971.

62. Briones, A. M., Ervin, J. S., Putnam, S. A., Byrd, L. W., & Gschwender, L. (2010). Micrometer-sized water droplet impingement dynamics and evaporation on a flat dry surface. *Langmuir*, *26*(16), 13272-13286.

63. Shahidzadeh-Bonn, N., Rafai, S., Azouni, A. and Bonn, D. (2006). Evaporating droplets. *Journal of fluid mechanics*, *549*, pp. 307-313.

64. Wilms, J. (2005) Evaporation of Multicomponent Droplets, Doctoral dissertation, University of Stuttgart, Germany.

65. Sazhin, S. S., Elwardany, A., Krutitskii, P. A., Castanet, G., Lemoine, F., Sazhina, E. M. and Heikal, M. R. (2010). A simplified model for bi-component droplet heating and evaporation. *International Journal of Heat and Mass Transfer*, *53*(21), pp. 4495-4505.

66. ANSYS FLUENT 12.0, User's Guide, www.ansys.com, April 2009.

67. Kumar, P. (2013). Magnetism and magnetotransport in half and over doped manganites impact of substrate induced strain and Polycrystalline Disorder, Doctoral dissertation, Jaypee Institute of Information Technology, India.

68. Nakaruk, A. S. C. C., & Sorrell, C. C. (2010). Conceptual model for spray pyrolysis mechanism: fabrication and annealing of titania thin films. *Journal of coatings technology and research*, *7*(5), 665-676.

69. Reuge, N., & Caussat, B. (2007). A dimensionless study of the evaporation and drying stages in spray pyrolysis. *Computers & chemical engineering*, *31*(9), 1088-1099.

70. Huang, L., Kumar, K., & Mujumdar, A. S. (2004). Simulation of a spray dryer fitted with a rotary disk atomizer using a three-dimensional computational fluid dynamic model. *Drying Technology*, *22*(6), 1489-1515.

71. Jiang, X., Ward, T. L., Swol, F. V., & Brinker, C. J. (2010). Numerical Simulation of Ethanol− Water− NaCl Droplet Evaporation. *Industrial & Engineering Chemistry Research*, *49*(12), 5631-5643.

72. Widiyastuti, W., Wang, W. N., Lenggoro, I. W., Iskandar, F., & Okuyama, K. (2007). Simulation and experimental study of spray pyrolysis of polydispersed droplets. *Journal of Materials* Research, *22*(07), 1888-1898.

73. Filipovic, L., Selberherr, S., Mutinati, G. C., Brunet, E., Steinhauer, S., Köck, A., ... & Schrank, F. (2013). Modeling spray pyrolysis deposition. In *Proceedings of the World Congress on Engineering* (Vol. 2, pp. 987-992).

74. Blaker, K. A., Halani, A. T., Vijayakumar, P. S., Wieting, R. D., & Wong, B. (1988). *U.S. Patent No. 4,751,149*. Washington, DC: U.S. Patent and Trademark Office.

75. Barnes, T. M., Leaf, J., Fry, C., & Wolden, C. A. (2005). Room temperature chemical vapor deposition of c-axis ZnO. *Journal of Crystal Growth*, *274*(3), 412-417.

CHAPTER 3: MODELING OF AEROSOL SPRAY

3.1 Overview

In this chapter, a model of aerosol spray is developed for synthesis of sensor film from solution. The synthesis technique considered involves atomization of a solution of mixed salts in methanol, spraying of solution droplets, droplet deposition on a heated substrate, evaporation and chemical reaction to produce mixed oxides, and subsequent film growth. The precise control of oxide nanoparticle size distribution and inter-particle spacing in the film is crucial to achieving high sensitivity. These in turn largely depend on the droplet characteristics prior to impingement on the substrate. This research focuses on the development of a model to describe the atomization and spray processes prior to the film growth. Specifically, a mathematical model is developed utilizing computational fluid dynamics solution of the equations governing the transport of atomized droplets from the nozzle to the substrate in order to predict droplet characteristics in flight. The predictions include spatial distribution of droplet size and concentration, and the effect on these characteristics of swirling inlet flow at the spray nozzle.

3.2 Problem Considered

In SPT, a precursor solution which contains constituent reactant compounds is assumed to be atomized in the nozzle to tiny droplets. The droplets are then sprayed onto a preheated substrate. (Fig. 3-1) A film of stable compounds subsequently forms and adheres to the substrate due to chemical reaction and thermal decomposition of the solution. Complete chemical reaction occurs only when the ratio of reacting materials in the sprayed solution is stoichiometric. Therefore, control of the droplet size and composition just prior to impingement on the substrate is crucial to synthesis of film with optimal oxide particle size distribution and sensitivity [1]. A number of experimental studies have focused on the variation of the parameters affecting film growth [2].

Figure 3-1 - Aerosol system used for spraying the solution.

The precise control of nanoparticle size distribution and inter-particle spacing in the film is essential to achieving high sensitivity. The average size and size distribution of the particles can be estimated from the size of the atomized droplet and the concentration of the precursor solution [3]. Particle size can be controlled through appropriate choice of the atomization method and parameters [4-5].

The generation and distribution of particles in the resulting film is a multi-stage process which is highly dependent among other things, on the initial solution, atomization conditions, and the substrate temperature. Thus, the major issues that need to be addressed in the film synthesis are the type and composition of the initial solution, droplet generation, and particle morphology.

The reactants are usually dissolved in the solution of pre-determined stoichiometric ratio, with water or alcohol being the typical solvent [3]. The initial reactant concentration in the solution plays a significant role in determining the final particle size [6-7]. The droplets reaching the substrate are expected to contain sufficient amount of solvent to produce smooth and dense film [8]. Thus the solvent in the initially formed tiny particle can be evaporated before reaching the substrate and still be able to adhere to the substrate [9].

3.3 Formulation

There are two distinct stages to solving the aerosol spray problem investigated. For the present study air has been chosen as the continuous phase and methanol as the discrete phase. The first stage solution considers the air flow from the spray nozzle as well as the surrounding air. This is a steady state problem that determines the flow that will be used to track the droplets subsequently. The second stage considers droplet generation at the spray nozzle with defined initial velocity. After being released from the spray, the droplets follow the pattern which was defined previously by the continuous flow field. There occurs mass and energy exchange between the discrete phase (droplets) and continuous phase (air flow). In addition, the droplets may be evaporated as a result of the ambient thermal flow field which again would have been previously determined.

3.3.1 Modeling Continuous and Discrete Phase

Two approaches are typically used for mathematical modeling of spray deposition [10]: Euler-Lagrangian (E-L) and Euler-Euler (E-E). In the E-L approach which is employed in this chapter, the spray is considered a quasi-two phase flow of carrier gas and liquid droplets. The gas phase is treated as a continuum with the flow-field solved by the Navier-Stokes equations [12]. The dispersed phase (methanol droplets) is solved by tracking a large number of droplets through the calculated gas flow field. The droplet dynamics result from a force balance between the droplet inertia and the forces acting on the droplet thus:

$$\frac{du_p}{dt} = \frac{18\mu}{\rho_p d_p^2}\frac{C_D\,Re}{24}\left(u-u_p\right)+\frac{g_x(\rho_p-\rho)}{\rho_p}+\frac{1}{2}\frac{\rho}{\rho_p}\frac{d}{dt}\left(u-u_p\right)+F_x \qquad (3\text{-}1)$$

where u is the fluid phase velocity, u_p is the droplet velocity, ρ_p is the density of the droplet, d_p is the droplet diameter, C_D is the drag coefficient, and Re is the droplet relative Reynolds number $Re \equiv \frac{\rho d_p|u_p-u|}{\mu}$. The first term on the right-hand side of Eq. (3-1) is the drag force per unit droplet mass, the second is the buoyancy force due to gravity, and the third is the virtual mass force which is the force required to accelerate the fluid surrounding the droplets [12]. The virtual mass force is negligible since the density of air is much less than the droplet density. The other possible forces, such as thermophoretic force, Brownian force and Saffman's lift force are collectively inserted as F_x that can be eliminated in most cases in our study [10]. The Brownian force, which applies for sub-micron droplets, can be important when the energy equation is needed and the flow is laminar [10, 13].

It should be remarked that the flow field is predominant in one direction (gravitational direction), the shear rate is negligible, and since the droplet size is typically large (above the submicron domain), the Reynolds number will be high (the Re ranges from 600 to 1000 for the mass flow rates considered. Note that the transition Reynolds number for such flow systems is typically 1000) and Saffman force is expected to be insignificant [10, 14].

3.3.1.1 Drag Coefficient

The resistance of gas molecules always tends to slow down the movement of particles.

Under turbulent conditions, the drag force, F_D, can be defined as Newton's resistance thus:

$$F_D = C_D \frac{\pi}{8} \rho_g V^2 d_p^2 \tag{3-2}$$

where C_D is the drag coefficient. The drag coefficient has a nearly constant value of 0.44 when the flow is turbulent. Under laminar conditions, the Newton's law is no longer valid.

A number of correlations have been established for the drag coefficient, C_D, for the Euler-Lagrange model. The Schiller-Maumann correlation has been used in this research because the Reynolds number range considered is less than 1000 [10], thus:

$$\mathrm{C_D} = \frac{24}{\mathrm{Re}}(1 + 0.15\mathrm{Re}^{0.687}) \tag{3-3}$$

3.3.2 Heat and Mass Exchange

A multi-component droplet is defined as one consisting of a mixture of species [15]. Therefore, droplet mass (m) and density (ρ) can be formulated as [10]:

$$m = \sum_i m_i \tag{3-4}$$

$$\rho = \left(\sum_i \frac{m_i}{m\rho_i}\right)^{-1} \tag{3-5}$$

where subscript *i* refers to species *i*.

Heat and mass transfer equations are defined as follow:

$$m_p c_p \frac{dT_p}{dt} = A_p \varepsilon_p \sigma\left(\Theta_R{}^4 - T_p{}^4\right) + hA_p\left(T_\infty - T_p\right) + \sum_i \frac{dm_i}{dt}(h_{i,p} - h_{i,\infty}) \tag{3-6}$$

$$\frac{dm_i}{dt} = A_p M_{w,i} k_{c,i}\left(C_{i,s} - C_{i,\infty}\right) \tag{3-7}$$

where m_p is the mass of droplet, c_p is the droplet heat capacity, T_p is the droplet temperature, A_p is the surface area of droplet, T_∞ is the temperature of the continuous phase, ε_p is droplet emissivity, σ is Stefan-Boltzmann constant (5.67×10^{-8} W/m^2 K^4), Θ_R radiation temperature, and $h_{i,p}$ and $h_{i,\infty}$ are latent heats of droplets and the bulk gas respectively. The first term on the right-hand side of the heat transfer Eq. (3-6) represents the adsorption/emission of radiation at the droplet surface. The second term is the convective heat transfer between droplet and surrounding air, while the last term represents energy transfer associated with droplet evaporation.

The convective heat transfer coefficient h at the droplet/continuous phase interface of Eq. (3-6) is evaluated using the following correlation [16]:

$$Nu = \frac{hd_p}{k_\infty} == 2.0 + 0.6Re^{\frac{1}{2}}Pr^{\frac{1}{3}} \tag{3-8}$$

where k_∞ is the thermal conductivity of the continuous phase, and $Pr = c_p\mu/k_\infty$ is the Prandtl number of the continuous (gas) phase.

In Eq. (3-7), $C_{i,s}$ is the concentration of vapor at the droplet surface, and $C_{i,\infty}$ is the concentration of vapor in the bulk gas. It is important that all the processes of relevance are considered and integrated in one equation in the analysis of a multicomponent droplet. $M_{w,i}$ is the molecular weight of species i. The transfer coefficient k_c is calculated from the Sherwood correlation [16].

3.3.3 Droplet Diameter

One of the basic characteristics of atomization is the distribution of droplet size which is closely related to the nozzle condition. The Rosin-Rammler distribution approach introduces the most probable droplet size and a spread parameter to characterize the droplet size distribution. The most probable droplet size, d_0, can be expressed as [17]:

$$d_0 = 1.2726 d_{32}\left(1-\frac{1}{s}\right)^{\frac{1}{s}} \tag{3-9}$$

where d_{32} is the Sauter mean diameter [18], and *s* is the spread parameter. Eq. (3-9) gives the range of droplet size distribution and can be evaluated from experimental observations. A large spread parameter value results in narrow droplet size distribution. The spread parameter can be chosen as 3.5 [10].

Wu et al. [19] proposed a correlation to relate the initial drop size to the estimated turbulence quantities of spray, thus:

$$d_{32} = 133.0\lambda We^{-0.74} \tag{3-10}$$

where $\lambda(=\frac{d}{80})$ is the radial integral length scale at the spray exit based upon fully-developed turbulent pipe flow, and $We \equiv \frac{\rho l u^2 \lambda}{\sigma}$ is the Weber number (l is the characteristic length which is assumed to be equivalent to the droplet diameter)

3.3.3.1 Droplet breakup, Collision and Coalescence

The breakup model assumes that when the droplet oscillations grow to a critical value (that is, when oscillations at the north and south poles of droplet with this amplitude meet at the droplet center and the distortion is equal to half the droplet radius), the parent droplet breaks up into a number of smaller child droplets. The initial child droplets are assumed neither distorted nor oscillating [20]. Child droplets are sampled based on the Rosin-Rammler distribution (see Eqs. (3-9) and (3-10)).

The outcome of a collision is coalescence or bouncing. The probability of each outcome is calculated from the coalitional Weber number (We_c) and experimental observations thus [10]:

$$We_c \equiv \frac{\rho U_{rel}^2 \bar{D}}{\sigma} \tag{3-11}$$

where U_{rel} is the relative velocity between two droplets of interest and $\bar{D}$ is the arithmetic mean diameter of the two droplets. This probability is derived from the point of view of the larger droplet (droplet 1) and the smaller droplet (droplet 2). The model uses droplet 1 as reference such that its velocity is zero. In this reference frame, the probability of coalescence is related to the offset of droplet 1 center and trajectory of droplet 2. In general, the outcome leads to coalescence if the droplets collide head-on, and bouncing if the collision is oblique. There is a critical offset which is a function of the collisional Weber number and the relative radii of the droplets, defined by the critical collision parameter b_{crit} thus [21]:

$$b_{crit} = (r_1 - r_2)\sqrt{\min(1.0, \frac{2.4f}{We})} \qquad (3\text{-}12)$$

where r_1 is the radius of droplet 1, r_2 is the radius of droplet 2, and f is a function of r_1/r_2 defined as:

$$f\left(\frac{r_1}{r_2}\right) = \left(\frac{r_1}{r_2}\right)^3 - 2.4\left(\frac{r_1}{r_2}\right)^2 + 2.7\left(\frac{r_1}{r_2}\right) \qquad (3\text{-}13)$$

The value of the actual collision parameter, b, is $(r_1 + r_2)\sqrt{Y}$, where Y is a random number between 0 and 1. The calculated b is compared to $b_{crit.}$ If $b < b_{crit}$ we can assume that the result of collision is coalescence. Otherwise, the droplets bounce and each one has a new velocity and direction based on conservation of momentum and energy.

3.3.4 Atomizer Model

The physical atomizer parameters such as orifice diameter and mass flow rate can be used to estimate the initial droplet size, velocity and position. The liquid sheet issuing from the nozzle is atomized into droplets by the air directed against it. The liquid sheet trajectory exits from an annulus with inner and outer diameters of 3.5 mm and 4.5 mm respectively (the film height can be calculated as 0.5 mm consequently). The sheet initially converges toward the centerline at an angle of 45° (spray half angle). In this atomization process the droplet size is largely controlled by the gas/liquid mass ratio and the initial length scale of the liquid as it encounters the air. The droplet size can be controlled by means of the liquid port diameter [22]. Figure 3-2 [10] shows a schematic sketch of the atomizer system considered. It consists of two air flow sources: inner air stream and a swirling annular stream, which surrounds the inner air.

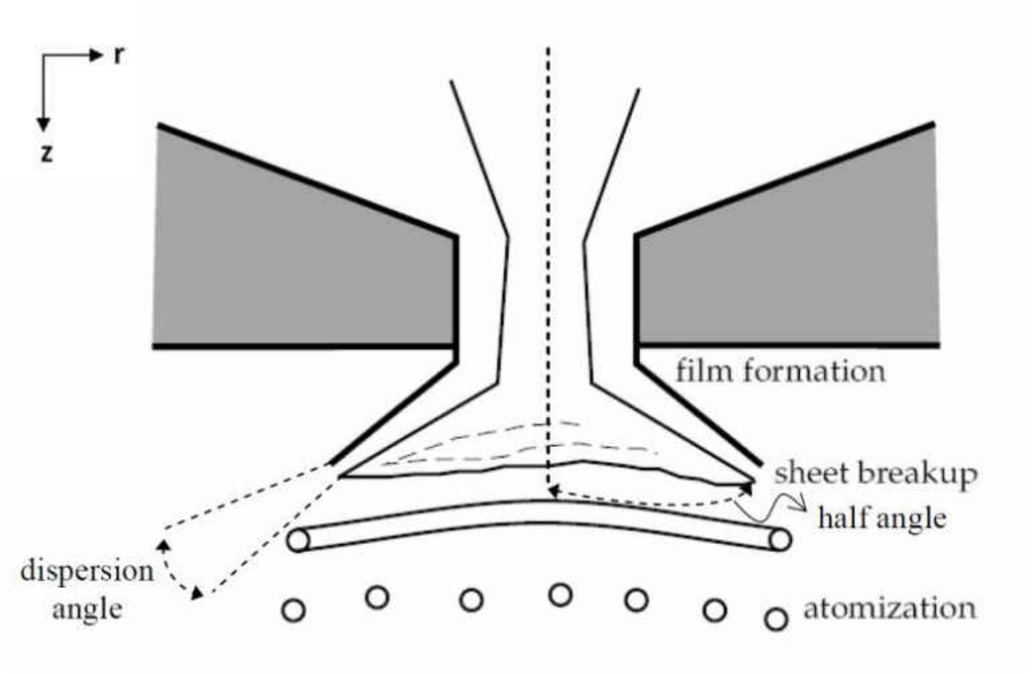

Figure 3-2 - Internal atomizer flow to the external spray.

3.3.5 Computational Details

3.3.5.1 Boundary and Initial Conditions

The atomizer consists of two air flow sources: inner air stream and a swirling annular stream, which surrounds the inner air. The corresponding computational domain considered is shown schematically in Fig. 3-3.

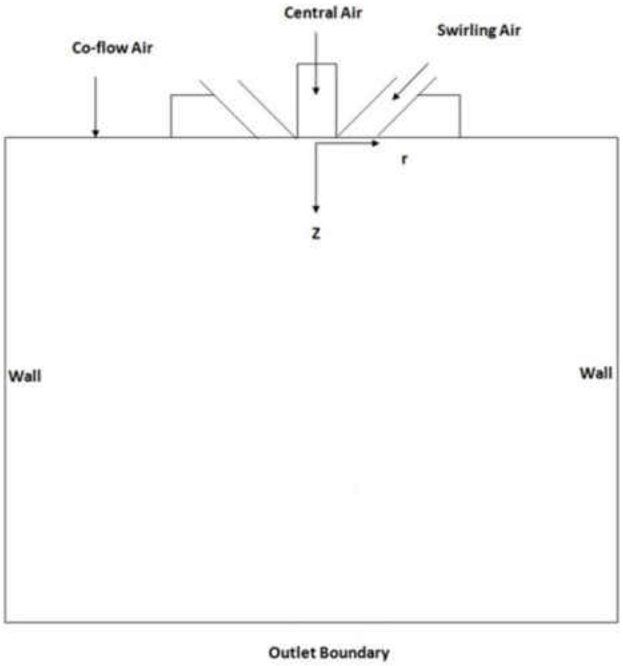

Figure 3-3 - Inlet and boundary conditions.

The initial and boundary conditions employed at the inlet to the computational domain are listed in Table 3-1. The outlet boundary is defined as a pressure outlet with I_t=5%, μ_t = 5 % and T=293K because of inflow through this boundary [15]. These values have been chosen based on previous studies [12].

Table 3-1 - Continuous phase boundary conditions.

Inlet	**Mass flow rate, $\dot{M}$ (kg/s)**	**Velocity, $\lvert V \rvert$ (m/s)**	**Turbulence intensity, I_t (%)**	**Hydraulic Diameter, D_h (m)**	**T (K)**
Central Air	9.167×10^{-5}	-	10	0.0037	293
Co-flow Air	-	1	5	0.0726	293
Swirling Air	-	19; 27	5	0.0043	293

Methanol (CH_3OH) is chosen as the base liquid for generating the droplets which can also evaporate. Its saturated vapor pressure is considered a linear function of temperature. The methanol is assumed to be cooled to 263 K before being introduced into the atomizer.

The relative velocity between the atomizing air and liquid sheet is assumed to be 82.6 m/s based on previous experimental study [2]. To reduce calculation load of 3 dimensional modeling, a 30° section of the atomizer is simulated with symmetric boundaries. For this 30° section, three mass inflow rates are investigated thus: 8.5×10^{-5}(kg/s), 1.275×10^{-4} (kg/s), and 1.7×10^{-4} (kg/s). The atomizer dispersion angle assumes the default value of 6° based on previous work [23].

3.3.5.2 Mesh and Geometry

A comprehensive grid refinement study was done to ensure numerical accuracy of the results. The initial mesh size was set at 1 mm and systematically refined especially near the outlet of spray and centerline using the approach in a previous study [12]. Finally 6.40×10^4 quadratic cells were used to obtain grid independent results. The experimental data of Patil [5] were used to validate the initial results of the impingement study.

3.3.5.3 Swirl Flow

The effect of swirl flow on spray characteristics is also investigated. A Swirl number, S, is defined as:

$$S = \frac{G_{\emptyset}}{RG_x} = \frac{\int_o^R UWr^2dr}{\int_o^R U^2rdr} \tag{3-14}$$

where $G_{\emptyset}$ (kg m^2/s^2) is the axial flux of the swirl momentum, G_x (kg m^2/s^2) is the axial flux of the axial momentum, and R (m) is the characteristic length. Here we take the radius of the swirl annulus as the characteristic radius [24].

The axial and radial components of inlet gas velocity (U and W) are calculated at each radial distance from the centerline (r) are considered in Eq. (3-14). The resulting swirling air velocity is varied from 19 m/s to 27 m/s, giving S=0.01 to 0.02.

3.3.5.4 Viscous model parameters

Since the main flow is turbulent, a "realizable" k-ε turbulence model is used. The term "realizable" indicates that the model satisfies certain mathematical constrains on the Reynolds stresses which is consistent with the physics of turbulent flows. This model provides a more accurate prediction of the spreading rate of jets than the standard k-ε model. The model constants are chosen as the default values of Launder and Spalding [25] and Kays et al. [26], including $C_{1\varepsilon} = 1.44$, and $C_{2\varepsilon} = 1.9$, and turbulent Prandtl numbers of $\sigma_k = 1.0$, and $\sigma_\varepsilon = 1.2$, energy and wall turbulent Prandtl numbers of 0.85, and Turbulent Schmidt number of 0.7.

A stochastic tracking approach is used to predict the turbulent dispersion of particles. The model simulates the interaction of a particle with a succession of discrete stylized fluid phase turbulent eddies, called discrete random walk model. In this model, each eddy is characterized by a Gaussian distributed random velocity fluctuation and a time scale which can be set as a random number multiplied by the k/ε ratio and an integral time-scale constant factor (CL = 0.15 for the k- ε model). Integral time shows the time spent in turbulent motion along the particle path.

3.3.6 Numerical Details

The above set of equations is solved subject to the given boundary conditions, using the FLUENT commercial code [15]. The discrete phase is allowed to interact with continuous phase, i.e. exchange mass, momentum, and energy. Although the continuous phase flow is treated as a steady state problem, particle tracking is assumed unsteady in order to improve numerical stability of particle source terms. In addition, since there is allowance for droplet collision and droplet breakup in the model, the particle dynamics is unsteady. The number of interactions which allows control of the frequency at which the particles are tracked is set to 10. The particle time step size is 0.0001 *s* and the number of time steps is 1 per simulation iteration. The injection duration is 100 *s* which is much larger the period of interest which means the injection essentially continuous. The maximum number of time steps used to compute a single particle trajectory via integration of equation is set to 500 to ensure sufficient time for particle tracking and avoid particle being trapped in a recirculating flow. The integration time step size (Δt) is set to *5 s* implying that 60 droplet parcels are introduced into the domain at every time step. Under relaxation factor of 0.1 is employed for discrete phase sources. The simulations converged after about 160 iterations and 15 minutes of CPU time in all the cases considered.

3.4 Results

Figure 3-4 shows the predicted radial variation of the axial velocity at several axial (z) planes from the spray tip for the case with spray mass flow rate of 1.275×10^{-4} (kg/s) and inlet swirl number S=0.01. The velocity is normalized by the centerline value while the radial distance is normalized by the half radius of the jet. The predicted velocity profile exhibits self-similarity far from the nozzle. The high swirling flow outside the nozzle acts to mix and atomize the spray as well as suppress droplet dispersion. The self-similarity observed at some distance from the spray nozzle indicates that the effect of swirl is limited to the vicinity of the nozzle, for the specific conditions considered.

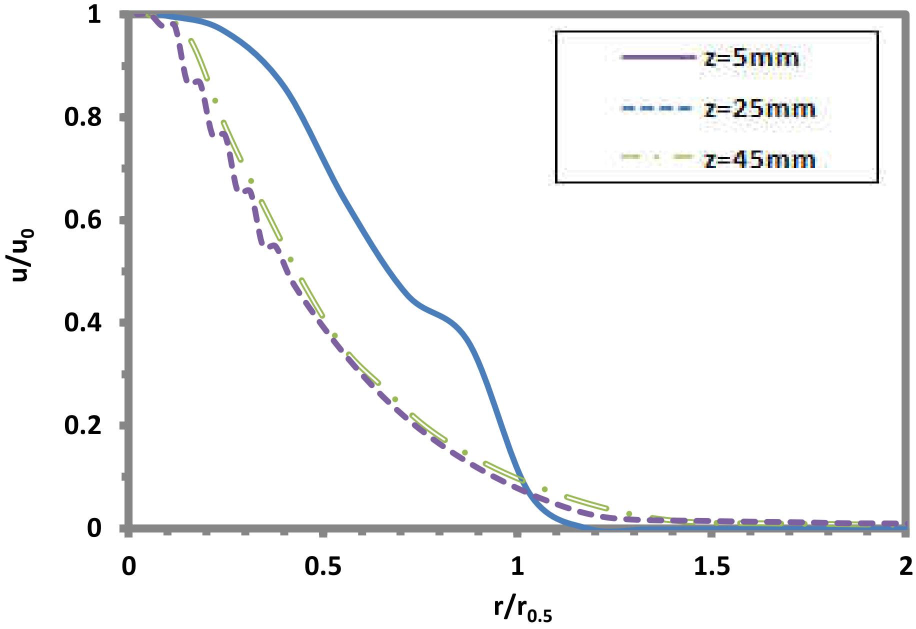

Figure 3-4 - Axial velocity profile on three axial planes from the spray nozzle; $\dot{m}$ = 1.275×10^{-4} (kg/s).

Figure 3-5 shows the corresponding radial distribution of normalized concentration (mole fraction of the methanol) at three axial planes from the nozzle. The mole fraction is normalized by values at the centerline and the radial distance is normalized by the outer diameter of the spray at each axial distance. In the consensus of the velocity profile prescribed in the previous Fig. 3-4, the predicted concentration profile spreads more uniformly farther away from the nozzle, where the confinement effect of swirl has attenuated for the relatively small swirl number (*S*=0.01) considered. This finding may be useful in guiding the optimal placement of substrate for uniform particle distribution and uniform film growth.

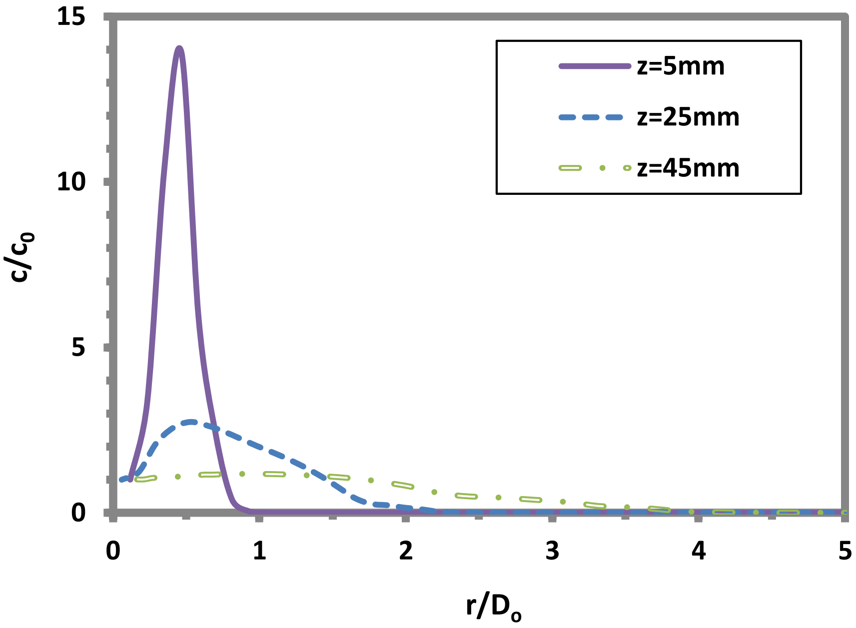

Figure 3-5 - Normalized concentration of solvent on three axial planes from spray nozzle; $\dot{m}$ = 1.275×10^{-4} (kg/s).

3.4.1 Effect of spray Mass flow rate

Different mass flow rates are applied to examine spray modeling: 8.5×10^{-5} (kg/s), 1.275×10^{-4} (kg/s), and 1.7×10^{-4} (kg/s). Figures 3-6 and 3-7 represent mole concentration variation like Fig. 3-5 but with different mass flow rates. Similar trends have been observed as explained before.

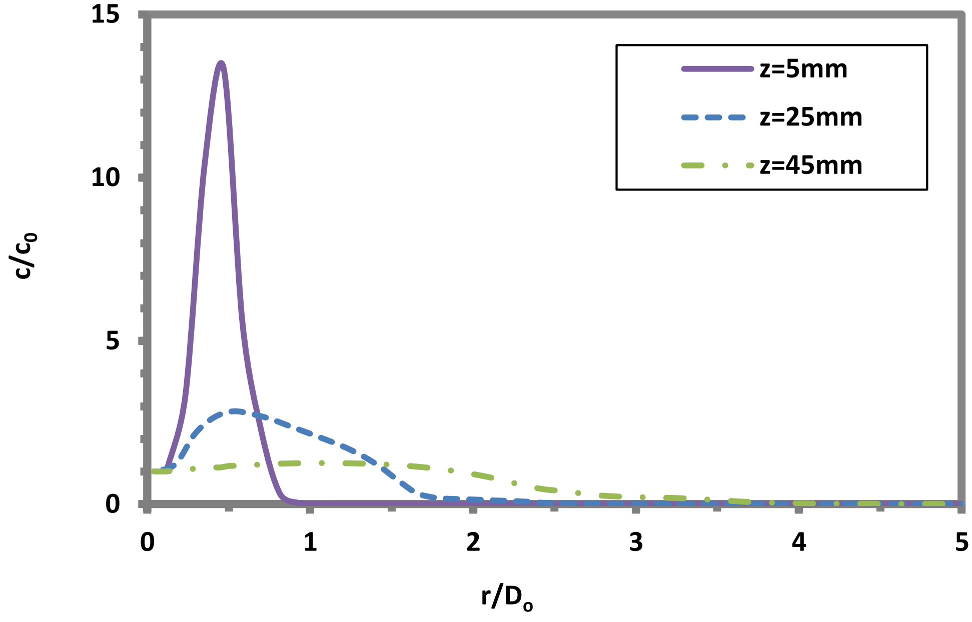

Figure 3-6 - Mole concentration of solvent on three planes from spray nozzle; $\dot{m}$ = 8.5×10^{-5}(kg/s).

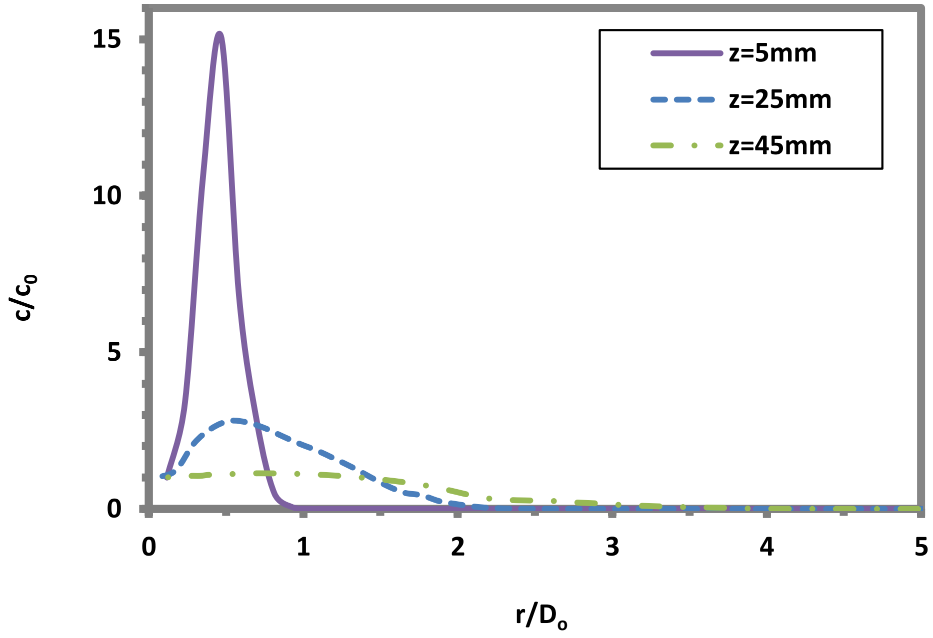

Figure 3-7 - Mole concentration of solvent on three planes from spray nozzle; $\dot{m}$ = 1.7×10^{-4} (kg/s).

Figures 3-8 and 3-9 show the effect of varying the inlet mass flow rate on the radial distribution of mass fraction at specific axial planes of z = 5 mm and z = 25 mm from the spray nozzle.

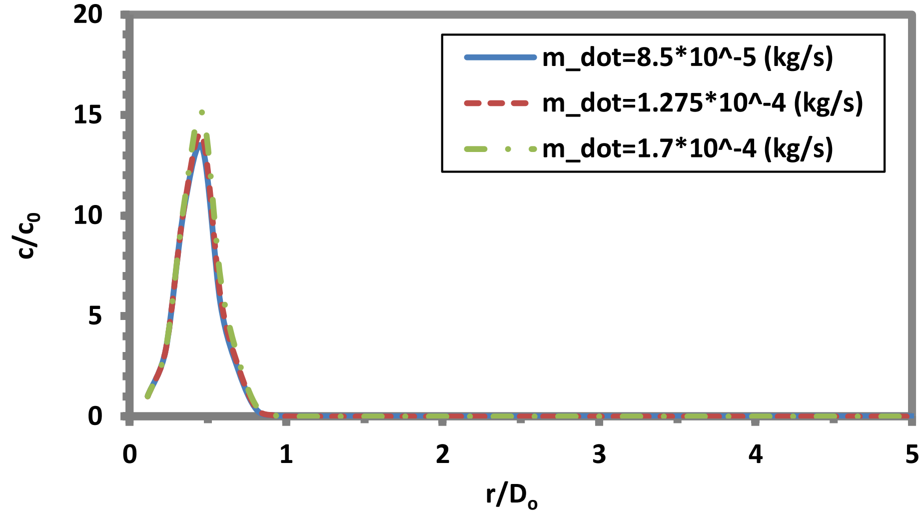

Figure 3-8 - Mole concentration of solvent at z=5mm from spray at three different spray mass flow rates.

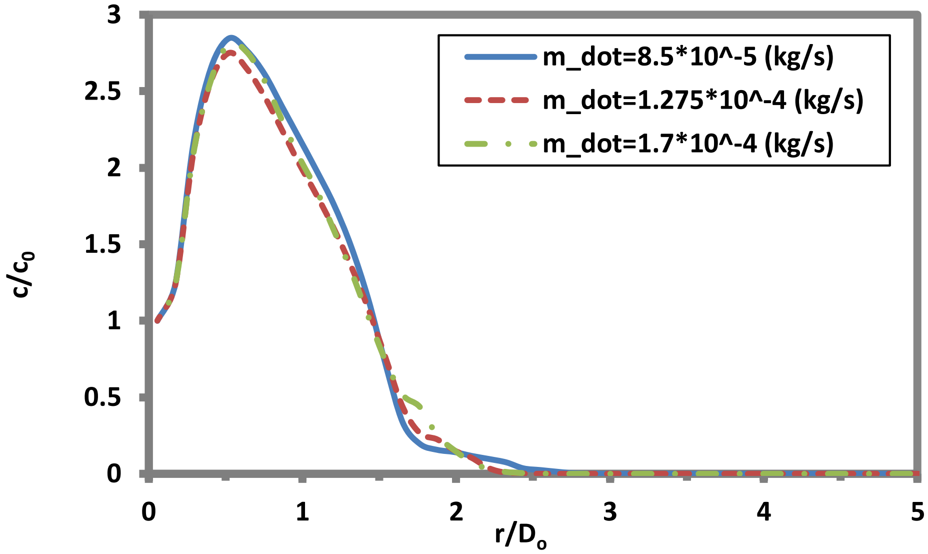

Figure 3-9 - Mole concentration of solvent at z=25mm from spray at three different spray mass flow rates.

Figure 3-10 shows the effect of varying the inlet mass flow rate of spray on the radial distribution of concentration (mole fraction of methanol) at a specific axial plane z=45mm from the spray nozzle. It should be noted that the flow has become self-similar at this location. This result indicates that the input spray flow rate within the range considered does not have significant effect on the normalized radial concentration distribution. This is consistent with the self-similarity of results at that axial location, as well as the limited effect of the swirling flow beyond the vicinity of the nozzle.

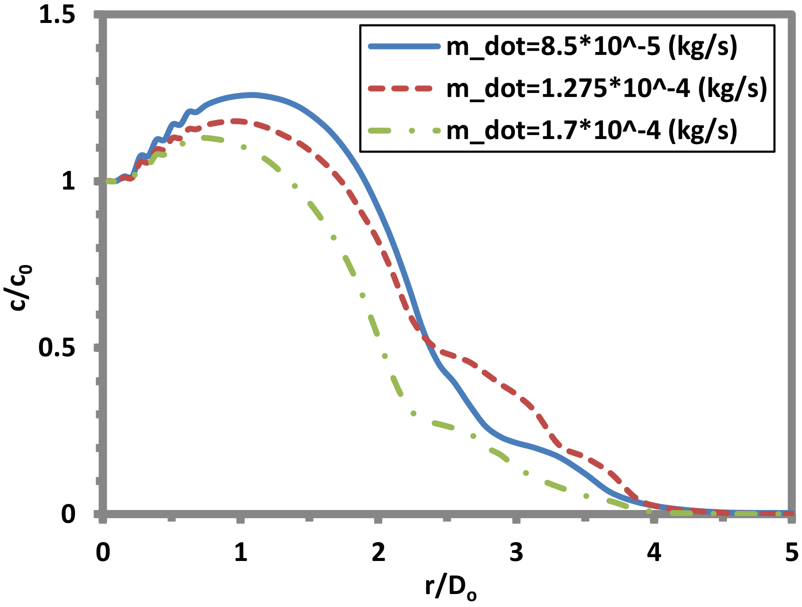

Figure 3-10 - Normalized concentration of solvent at axial plane z=45mm from spray nozzle for three different spray mass flow rates.

Figure 3-11 shows the predicted proportion of droplets (vertical axis) having specified average concentration (horizontal axis) as a function of the spray mass flow rate.

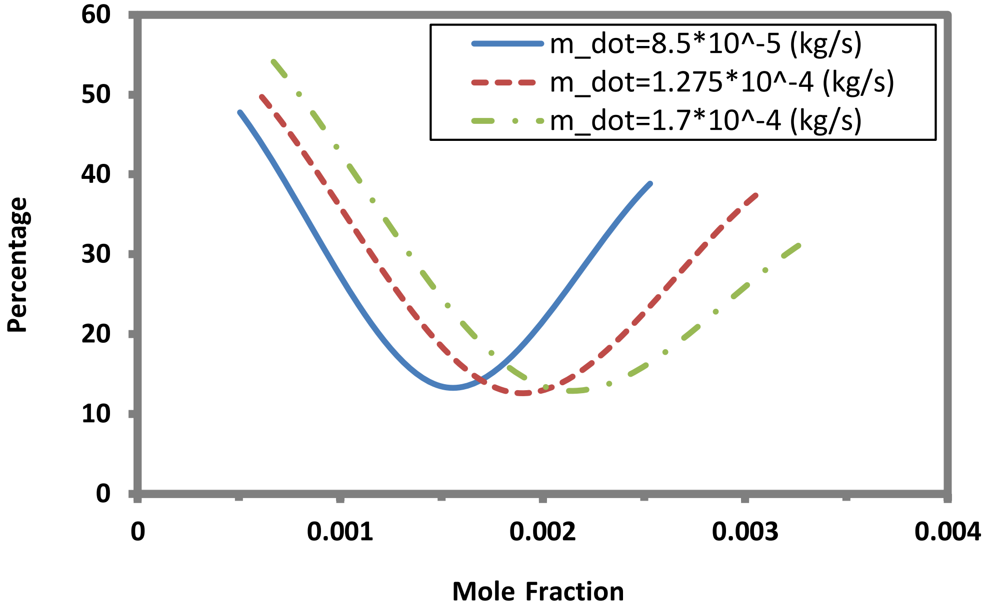

Figure 3-11 - Percentage of droplets with different mole concentration.

The result exhibits a minimum at almost 13% of particles, in irrespective of mass flow rate, having a mass fraction of 1.517×10^{-3}, 1.837×10^{-3}, and 2.011×10^{-3} as the mass flow rate increases. It can be explained that the particles either tend to remain tiny with low mass concentration or to collide to form larger particles with higher mass concentration. This may be related to the balance between particles momentums and surface tension effect. The results indicate that high mass flow rate affects the concentration of droplets in general. Specifically, there are more droplets with high mole fraction of solvent when the spray rate is increased, or in other word, the droplets with high solvent concentration increases. This trend can be attributed to the strong effect of mass flow rate on atomization rate. When the droplets have high kinetic energy, the momentum overwhelms the surface tension (smaller Weber number less than 100 [27]). Thus the initial droplets adhered together readily to form droplets with higher mole fractions. Therefore, there may be more sufficient solvent for the chemical reaction to proceed to produce the particles on the substrate.

3.4.2 Effect of Swirl

Figure 3-12 shows the normalized concentration in the radial direction from the centerline at different axial locations from the nozzle for swirl number S=0.01. Figure 3-13 shows the corresponding results at a higher swirling number S=0.02. The two sets of results are essentially similar. However, the peak concentration is larger at the lower swirl rate (S=0.01) at all axial planes. This trend implies that the droplets are more concentrated near the axis when swirl flow is relatively weak. When the swirl flow rate increases, the droplets are largely spread out in the radial direction and the maximum concentration decreases as a consequence.

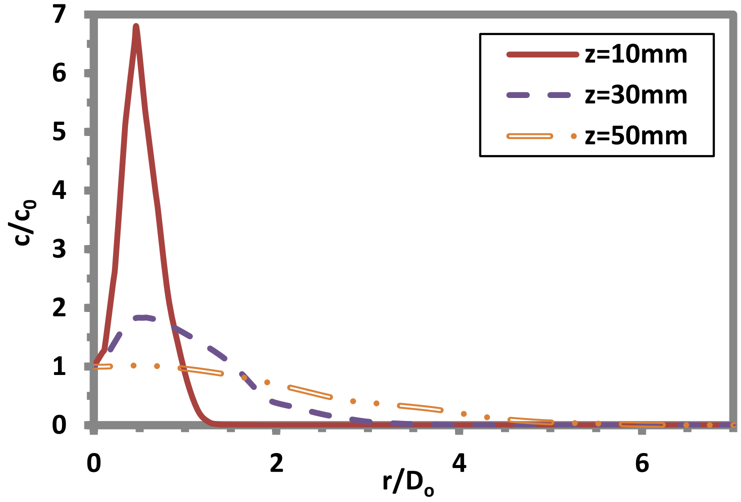

Figure 3-12 - Variation of normalized concentration of solvent with radial distance from centerline at three axial planes from spray nozzle (S=0.01).

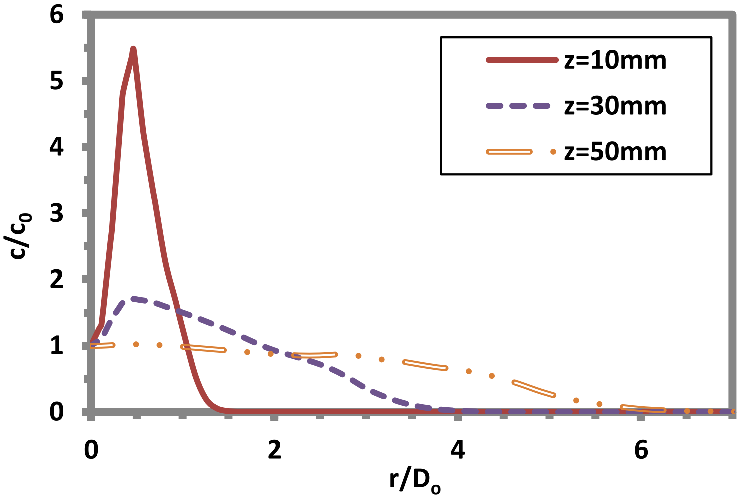

Figure 3-13 - Variation of normalized concentration of solvent with radial distance from centerline at three axial planes from spray nozzle (S=0.02).

Figure 3-14 shows the predicted concentration variation for swirl numbers *S*=0.01 and 0.0.2 at axial plane z=40 mm from the nozzle. The corresponding results at axial plane z=50 mm are presented in Fig. 3-15. The concentration profile spreads out more gradually at the larger swirl number, in the consensus of the results presented in previous Figs. 3-12 and 3-13. There is a marked change in slope between r/D_0=2 and r/D_0=3 at the smaller swirl number S=0.01. This trend may be attributed to the effect of the central air which spreads through the domain at the lower swirl flow rate. The sudden change in slope does not exist at the higher swirl number because the swirl effect perpetuates father away from the nozzle.

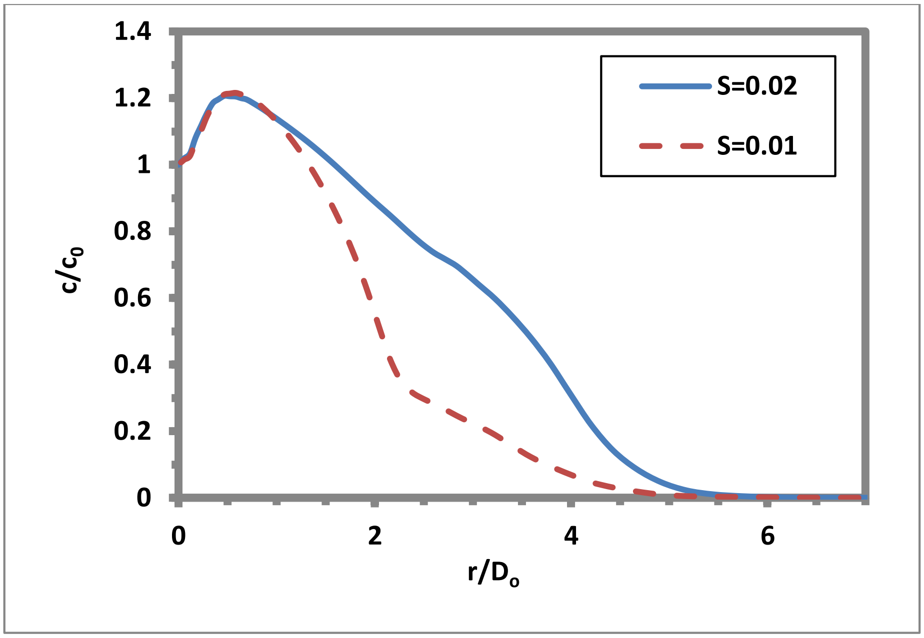

Figure 3-14 - Variation of normalized concentration of solvent with radial distance from centerline at z=40 mm.

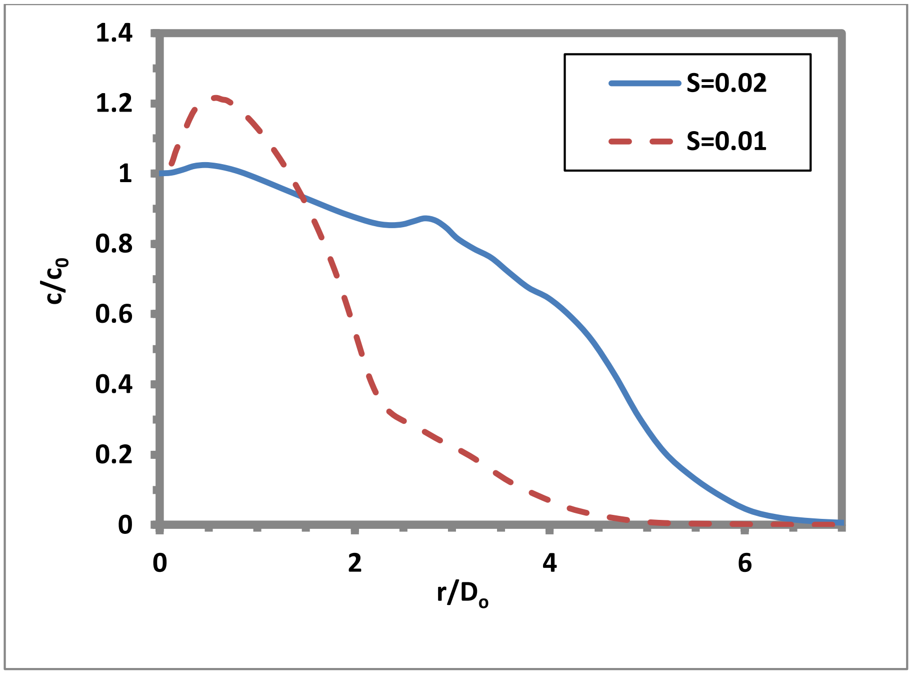

Figure 3-15 - Variation of normalized concentration of solvent with radial distance from centerline at z=50 mm.

Figure 3-16 shows the predicted evolution of droplet size for the two swirling numbers considered. The results show that there is in general a significant reduction in droplet size when the swirling air velocity increases. Specifically, by increasing the swirl number from 0.01 to 0.02, the minimum droplet diameter is reduced by 9%, the maximum diameter is reduced by 26% and the average size is reduced by 26% (see Table 3-2).

It should be noted that although the minimum diameter is reduced with increased swirling rate, there are other physical factors impacting droplet breakup. One of the most important of such factors is the surface tension of droplet fluid which determines the range of possible droplet sizes. The surface tension can be modified by changing the type of precursor solution used for the spray.

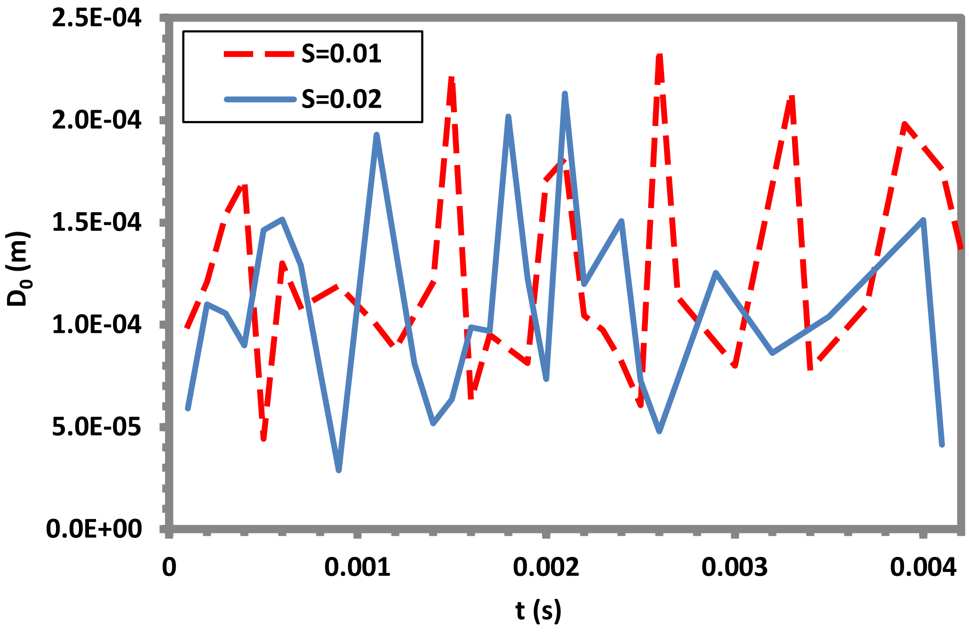

Figure 3-16 - Change in droplet diameter with time for one set of droplets (in whole domain): (a) S=0.01 and (b) S=0.02.

Table 3-2 - Predicted effect of swirl flow on droplet diameter.

Swirl Condition	**Minimum Diameter (m)**	**Maximum Diameter (m)**	**Average Diameter (m)**
S=0.01	3.16×10^{-5}	0.000288	5.70×10^{-5}
S=0.02	2.88×10^{-5}	0.000213	4.21×10^{-5}
Size change (%)	9.08	25.94	26.27

Figure 3-17 shows the predicted axial variation of total number of representative droplets (N) for S=0.01 and S=0.02. These results are obtained by introducing continuously 120 representative droplets of uniform size at the inlet and allowing for coalescence and breakup in the subsequent spray. The number of droplets first decreases until a certain axial distance (z=12.5 in both cases), increases until approximately z=35mm, decreases till about z = 40 and subsequently increases to the outlet of the domain. This trend may be attributed to the various stages of droplet collision, coalescence and breakup in relation to the flow pattern. Initially, the droplets have very high velocity and correspondingly, the highest Weber number (*We*) in the domain. This high *We* translates to high probability of collisions leading to coalescence (see Eq. (3-12)) and production of large-sized droplets but fewer in number. Further from the nozzle the velocity decreases (due to spray zone expansion) and the large droplets which were previously formed start to break up (secondary breakup) to smaller sizes. At this stage, the collisions primarily make the droplets bounce and disperse in different directions due to the relatively large size of droplets and low Weber number. Subsequently, (at z=35 mm in the cases considered) a slight decrease in number of droplets can be observed which may be attributed to evaporation of tiny droplets in the low downstream pressure and coalescence of the tiny droplets produced after secondary breakup. Beyond this zone and near the outlet, the probability of collision decreases significantly and the only phenomenon occurring is breakup of the remaining large droplets. There are generally more droplets at the higher swirl number than the lower swirl number due to higher potential for droplet breakup in the former situation. However there is a notable switch in that trend between z=35mm and z=45 mm. This switch may be due to the effect of swirl on droplet kinetic energy. Specifically, at high swirling rate, there is a higher probability for droplet collision and coalescence due to their high kinetic energy even far from the nozzle. Such coalescence may lead to a reduction in the number of droplets. This result is consistent with those presented in previous Figs. 3-15 and 3-16 which indicate residual effect of swirl at the higher swirl number (S=0.02) even at distances relatively remote from the spray nozzle.

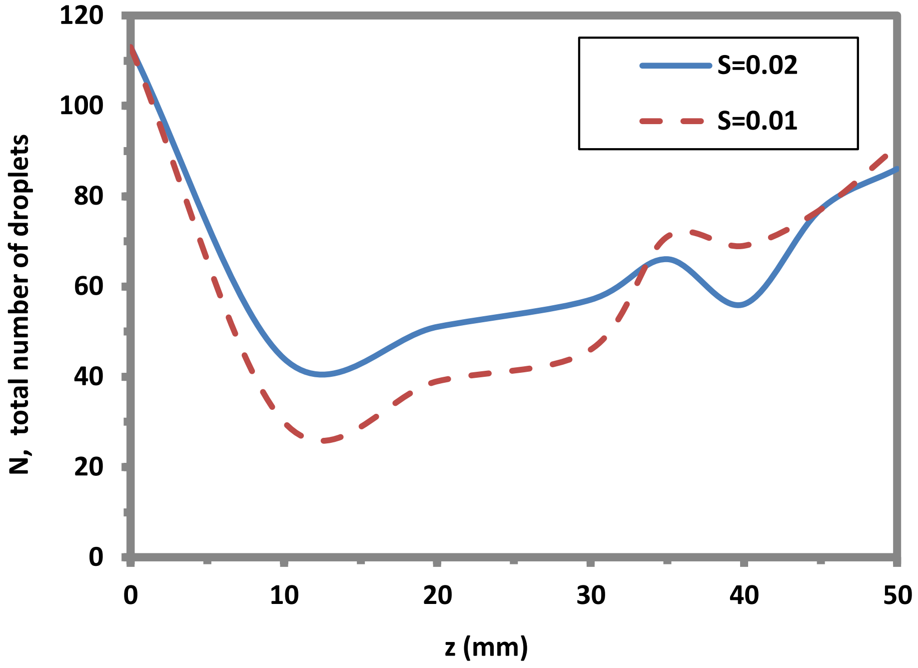

Figure 3-17 - Effect of swirl on axial variation of number of droplets.

3.5 Conclusion

The quality of films produced through spray pyrolysis method depends critically on tuning the atomizer parameters. Specifically, the droplet characteristics play important role in the determination of film microstructure and film properties. The optimum spray flow rate, and substrate positioning and temperature for desired film property can be determined through mathematical modeling. The droplet characteristics in an aerosol spray has thus been investigated. The characteristics considered include droplet diameter distribution, velocity and rate of spread of spray, effect of spray mass flow rate as well as the effect of swirling flow on solvent concentration and number of droplets generated

3.6 List of References

1. Chen, C. Y., Tseng, T. K., Tsai, S. C., Lin, C. K., & Lin, H. M. (2008). Effect of precursor characteristics on zirconia and ceria particle morphology in spray pyrolysis. *Ceramics International*, *34*(2), 409-416.
2. Korotcenkov, G., Brinzari, V., Schwank, J., DiBattista, M., & Vasiliev, A. (2001). Peculiarities of SnO_2 thin film deposition by spray pyrolysis for gas sensor application. *Sensors and Actuators B: Chemical*, *77*(1), 244-252.
3. Okuyama, K., & Wuled Lenggoro, I. (2003). Preparation of nanoparticles via spray route. *Chemical Engineering Science*, *58*(3), 537-547.
4. Perednis, D., & Gauckler, L. J. (2005). Thin film deposition using spray pyrolysis. *Journal of Electroceramics*, *14*(2), 103-111.
5. Patil, P. S. (1999). Versatility of chemical spray pyrolysis technique. *Materials Chemistry and physics*, *59*(3), 185-198.
6. Ko, J. W., Yoo, J., Kim, Y. K., Chung, K. C., Chung, H., & Yoo, S. I. (2005). Fabrication of fine and homogeneous MgB 2 nano powders by spray pyrolysis. *Applied Superconductivity, IEEE Transactions on*, *15*(2), 3349-3351.
7. Kang, Y. C., Chung, Y. S., & Park, S. B. (1999). Preparation of YAG: Europium Red Phosphors by Spray Pyrolysis Using a Filter-Expansion Aerosol Generator. *Journal of the American Ceramic Society*, *82*(8), 2056-2060.
8. Dedova T. (2007). Chemical spray pyrolysis deposition of zinc sulfide thin films and zinc oxide nanostructured layers. Doctoral dissertation, Tallinn University of Technology, Estonia.
9. Perednis, D. (2003). Thin film deposition by spray pyrolysis and the application in solid oxide fuel cells. Doctoral dissertation, Swiss Federal Institute of Technology, Zurich.
10. ANSYS FLUENT 12.0 Theory Guide, Chapter 15. Discrete Phase, www.ansys.com, April 2009.

11. Ettema, R. (Ed.). (2000). *Hydraulic modeling: Concepts and practice* (No. 97). ASCE Publications.

12. Lim, E. W. C., Heng Koh, S., Kuang Lim, L., Hoon Ore, S., Kiat Tay, B., Ma, Y., & Wang, C. H. (2008). Experimental and computational studies of liquid aerosol evaporation. *Journal of Aerosol Science*, *39*(7), 618-634.

13. Liu, A. B., Mather, D., & Reitz, R. D. (1993). *Modeling the effects of drop drag and breakup on fuel sprays* (No. 930072). SAE Technical Paper.

14. Saffman, P. (1965). The lift on a small sphere in a slow shear flow. *Journal of Fluid Mechanics*, *22*(02), 385-400.

15. ANSYS FLUENT 12.0 User's Guide, www.ansys.com, April 2009.

16. Ranz, W. E., & Marshall, W. R. (1952). Evaporation from drops. *Chem. Eng. Prog*, *48*(3), 141-146.

17. Lefebvre, A. (1988). *Atomization and sprays* (Vol. 1040, No. 2756). CRC press.

18. Kuo, K. K. (1986). Principles of combustion. John Wiley and Sons, New York.

19. Wu, P. K., Tseng, L. K., & Faeth, G. M. (1992). Primary breakup in gas/liquid mixing layers for turbulent liquids. *Atomization and Sprays*, *2*(3).

20. Aerosol Research Group at Washington University in St. Loius, Educational website: http://www.aerosols.wustl.edu/Education/default.htm.

21. O'Rourke, P. J. (1981). *Collective drop effects on vaporizing liquid sprays* (No. LA-9069-T). Los Alamos National Lab., NM (USA).

22. Nasr, G. G., Yule, A. J., & Bendig, L. (2002). *Industrial sprays and atomization: design, analysis and applications*. Springer, New York.

23. Schmidt, D. P., Corradini, M. L., & Rutland, C. J. (1999, July). A two-dimensional, non-equilibrium model of flashing nozzle flow. In *3rd ASME/JSME Joint Fluids Engineering Conference* (Vol. 208, p. 616).

24. Malalasekera, W., Ranga Dinesh, K. K. J., Ibrahim, S. S., & Kirkpatrick, M. P. (2007). Large eddy simulation of isothermal turbulent swirling jets. *Combustion Science and Technology*, *179*(8), 1481-1525.

25. Launder, B. E., & Spalding, D. B. (1972). Lectures in mathematical models of turbulence. Academic Press, London, England.

26. Kays, W. M., Crawford, M. E., & Weigand, B. (2012). *Convective heat and mass transfer*. Tata McGraw-Hill Education.

27. Gatne, K. P., Jog, M. A., & Manglik, R. M. (2009). Surfactant-induced modification of low Weber number droplet impact dynamics. *Langmuir*, *25*(14), 8122-8130.

CHAPTER 4: MODELING EVAPORATION AND CHEMICAL REACTION IN A MULTI-COMPONENT DROPLET

4.1 Overview

This chapter describes the mathematical modeling of transport and chemical reaction phenomena in a single droplet deposited on a heated substrate by spray pyrolysis. The droplet contains mixed salt solutions of Tin Chloride ($SnCl_4$) and Indium Nitrate ($In(NO_3)_3$) which react on the substrate to produce mixed oxides ($In_2O_3+SnO_2$) and water residue. The water residue is subsequently evaporated, leaving a thin film of the mixed oxides. The droplet, containing solvent and precursors is modeled using Computational Fluid Dynamics technique. The various stages of droplet morphology associated with surface energy and evaporation are predicted. The transient distribution is also predicted of the concentration of the various species in the droplet. The results show that homogeneous chemical reaction occurs within 60% of the radial distance from the center. This in turn results in the deposition of metal oxide within that region while a significant amount of unused reactants remains thereafter.

4.2 Problem Considered

The droplet, consisting of a two-phase aqueous solution of Tin Chloride ($SnCl_4$) and Indium Nitrate ($In(NO_3)_3$), impinges on a hot substrate as illustrated in Fig. 4-1. The concentration of $SnCl_4$ considered was 0.25 mol/l while that of $In(NO_3)_3$ was 0.1 mol/l. These concentrations were chosen based on optimum concentration employed in a previous study [1]. It should be noted that due to symmetry only one half of the droplet is simulated. Allowance is made for different species in the solution. The model assumes perfect thermal contact between the droplet and the isothermal substrate.

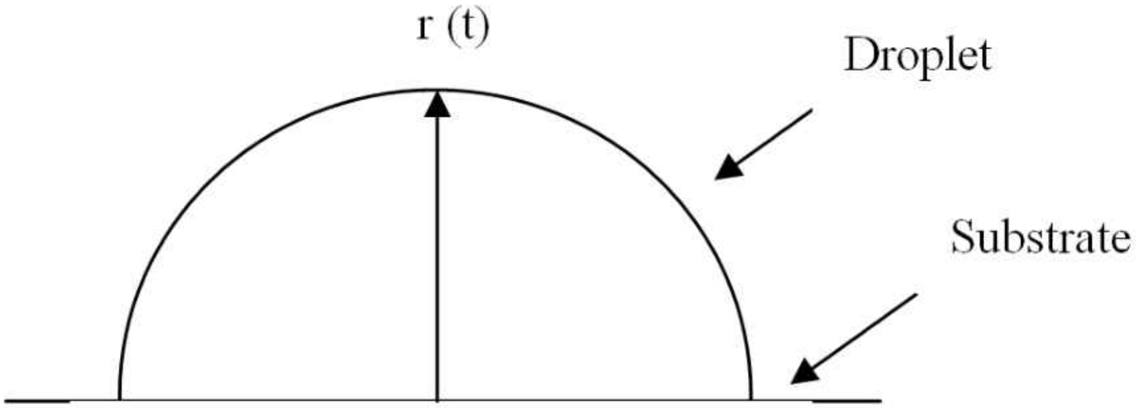

Figure 4-1 - Droplet domain for computation.

The transport equation comprises not only the equation of momentum and energy, but also species conservation due to variation of species in the droplet. Energy equation is required to model the heat transfer between the surface and the two-phase fluid which consists of liquid and gas phases (droplet and surrounding air) and between two fluids. Species transport between the fluid and the surface is also considered to model the deposition phenomena.

The preparation of a metal oxide thin film by the spray pyrolysis method depends on surface reaction (pyrolysis) of metal compounds, such as metal chlorides, on a heated substrate. The reaction type depends on the selection of the carrier gas and the solvent. The spray nozzle uses the carrier gas to atomize the chemical solution into aerosols. The temperature of the substrate is fixed at a constant value by using a temperature-controlled furnace or hot plate. In general, the films grown at a substrate temperature less than a specific value (depending on metal oxide type) are amorphous in nature [2]. The film formation depends on the droplet landing, reaction and solvent evaporation which relates to the droplet size [2]. The most ideal condition for film preparation is for the droplet to approach the substrate just before the solvent is completely evaporated off.

A similar approach is considered here to produce mixed metal oxides in which a dilute solution consisting of two metal compounds is sprayed on the hot substrate for the chemical pyrolysis. For example, in order to produce the mixed metal oxide, the following two chemical reactions occur:

$$\mathrm{SnCl_4} + 2\,\mathrm{H_2O} \rightarrow \mathrm{SnO_2} + 4\,\mathrm{HCl} \tag{4-1}$$

$$\mathrm{ZnCl_{2(l)}} + \mathrm{H_2O} \rightarrow \mathrm{ZnO} + 2\,\mathrm{HCl_{(g)}} \tag{4-2}$$

$$2\mathrm{In(NO_3)_3} + 3\,\mathrm{H_2O} \rightarrow \mathrm{In_2O_3} + 6\,\mathrm{HNO_3} \tag{4-3}$$

The details of the analysis of chemical reaction are provided in the subsequent section.

4.3 Formulation

4.3.1 Droplet Evaporation

4.3.1.1 Liquid-Gas Phase Model

The volume of Fluids (VOF) model embodied in the FLUENT computer code is applied [3] to model the two-phase transport phenomena because of the inherent well-defined interface between the liquid and gas phases. The liquid phase is water and the gaseous phase consists of water vapor and air. The approach essentially applied a surface-tracking technique to a fixed

Eulerian mesh. It is typically used for two or more immiscible fluids where the position of the interface between the fluids is desired [4]. The model simulates the flow of two fluids (liquid and gas) by solving a single set of Navier-Stokes equations. The governing equations in differential notations are as follows [5]:

4.3.1.2 Mass Conservation

$$\frac{\partial(\alpha_1\rho)}{\partial t}+\frac{\partial(\alpha_1\rho u)}{\partial r}+\frac{\partial(\alpha_1\rho u)}{r}+\frac{\partial(\alpha_1\rho v)}{\partial z}=-\dot{m}_{12} \qquad (4\text{-}4)$$

where $\alpha_1$is the liquid fraction, $\alpha_2(=1-\alpha_1)$ is the gas mass fraction, *u* is the radial velocity, *v* is the axial velocity, $\overset{o}{m}$ is the mass transfer rate per unit volume, and ρ is the density. In Eq. (4-4), *z* denotes the vertical and *r* the radial coordinate direction. The VOF equation is solved for the liquid phase only from which the gas phase volume fraction is deduced.

4.3.1.3 Momentum Conservation

$$\frac{\partial(\rho u)}{\partial t}+\frac{\partial(\rho uu)}{\partial r}+\frac{\partial(\rho vu)}{\partial z}+\frac{\partial(\rho uu)}{r}=\frac{\partial p}{\partial t}+2\frac{\partial}{\partial r}\left(\mu\frac{\partial u}{\partial r}\right)+\frac{\partial}{\partial z}\left(\mu\frac{\partial u}{\partial z}\right)+\frac{2\mu}{r}\frac{\partial u}{\partial r}+\frac{\partial}{\partial z}\left(\mu\frac{\partial v}{\partial r}\right)- \qquad (4\text{-}5)$$

$$\frac{2\mu u}{r^2}+\frac{2\sigma\rho K_1}{\rho_1+\rho_2}\frac{\partial\alpha_1}{\partial r}$$

$$\frac{\partial(\rho v)}{\partial t}+\frac{\partial(\rho uv)}{\partial r}+\frac{\partial(\rho vv)}{\partial z}+\frac{\partial(\rho uv)}{r}=-\frac{\partial p}{\partial z}+\frac{\partial}{\partial r}\left(\mu\frac{\partial v}{\partial r}\right)+2\frac{\partial}{\partial z}\left(\mu\frac{\partial v}{\partial z}\right)+\frac{\mu}{r}\frac{\partial v}{\partial r}+$$

$$\frac{\partial}{\partial r}\left(\mu\frac{\partial u}{\partial z}\right)+\frac{\mu}{r}\frac{\partial u}{\partial z}+\rho g+\frac{2\sigma\rho K_1}{\rho_1+\rho_2}\frac{\partial\alpha_1}{\partial z} \qquad (4\text{-}6)$$

where K is the curvature, σ is the surface tension, μ is the dynamic viscosity, p is the gauge pressure, ρ_1 is the density of phase 1, ρ_2 is the density of phase 2, $\rho = \alpha_1\rho_1 + \alpha_2\rho_2$, $2\sigma\rho K$ represents the surface tension force, u is the radial velocity, and v is the axial velocity,

4.3.1.4 Energy Equation

$$\frac{\partial(\rho E)}{\partial t} + \frac{\partial(u(\rho E+p))}{\partial r} + \frac{\partial(v(\rho E+p))}{\partial z} + \frac{u(\rho E+p)}{r} = \frac{\partial}{\partial r}\left(k\frac{\partial T}{\partial r}\right) + \frac{\partial}{\partial z}\left(k\frac{\partial T}{\partial z}\right) + \frac{k}{r}\frac{\partial T}{\partial r} \tag{4-7}$$

where $E = \frac{\alpha_1\rho_1E_1+\alpha_2\rho_2E_2}{\alpha_1\rho_1+\alpha_2\rho_2}$ is total energy per unit volume, and T is temperature.

4.3.1.5 Species Conservation

The species consist of water in liquid phase, and water vapor and air in gaseous phase involving in the evaporation and non-reaction processes. The equation governing species conservation can be expressed as:

$$\frac{\partial(\rho_g Y_{g,H_2O})}{\partial t} + \frac{\partial(\rho_g u Y_{g,H_2O})}{\partial r} + \frac{\partial(\rho_g v Y_{g,H_2O})}{\partial z} + \frac{\rho_g u Y_{g,H_2O}}{r} = \frac{\partial}{\partial r}\left(\rho_g D_{H_2O-air}\frac{\partial Y_{g,H_2O}}{\partial r}\right) + \tag{4-8}$$

$$\frac{\partial}{\partial z}\left(\rho_g D_{H_2O-air}\frac{\partial Y_{g,H_2O}}{\partial z}\right) + \frac{\rho_g D_{H_2O-air}}{r}\frac{\partial Y_{g,H_2O}}{\partial r} + \dot{m}_{lg}$$

where $Y_{g,air} = 1 - Y_{g,H_2O}$, $Y_{g,H20}$ is the mass fraction of water vapor, $Y_{g,air}$ is the mass fraction of air, and $D_{H2O\text{-}air}$ is the droplet diameter, and m_{lg} is the mass transfer rate between liquid and gas phases.

4.3.1.6 Boundary Conditions

Figure 4-2 shows a schematic of the computational domain and boundary conditions utilized in the study. The initial temperature in the domain is assumed to be 300 K. The following conditions are imposed on the boundaries:

- Substrate Surface:

$$\left.\begin{aligned} u &= 0\\ v &= 0\\ T &= 600K\end{aligned}\right\}\text{No-slip condition}$$

$$\frac{\partial \alpha_1}{\partial z} = 0,\ \frac{\partial Y_{H_2O}}{\partial z} = 0$$

where Y_{H20} is the mass fraction of water. The above conditions imply isothermal surface with no allowance gradient of water concentration since the wall is not permeable to the solution.

- Symmetry axis:

$$\frac{\partial \alpha_1}{\partial r} = 0, u = 0, \frac{\partial v}{\partial r} = 0, \frac{\partial Y_{g,O}}{\partial r} = 0, \mathit{and}\ \ \frac{\partial T}{\partial r} = 0$$

- Pressure-Outlet:

$P = 0$ (gauge)

The outlet boundary is located approximately 10 droplet diameters from the substrate surface, following a previous study [5] indicating that at such a distance, the boundary-induced disturbances are negligible.

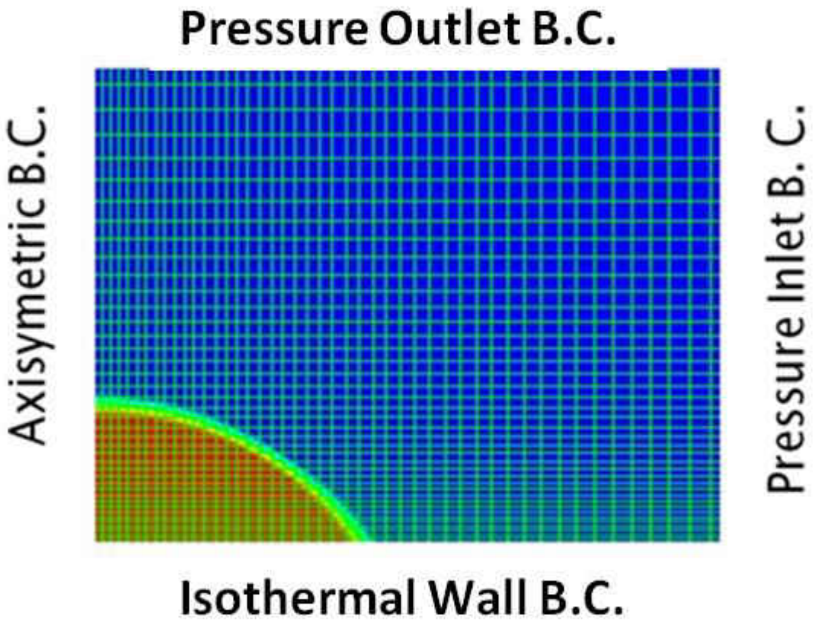

Figure 4-2 - Schematic of computational domain and boundary conditions.

4.3.2 Deposition on a Heated Surface

Mixing and transport of chemical species are modeled by solving the conservation equations for species concentration that include chemical reaction sources. The species in the present study are Tin Chloride ($SnCl_4$) and Indium Nitrate ($In(NO_3)_3$) and Oxygen (O_2) as reactants and Tin Oxide (SnO_2) and Indium Oxide (In_2O_3) as products. Although multiple simultaneous chemical reactions can be modeled with reactions occurring in the bulk phase (volumetric reactions) and on the wall surfaces, the present study considers the chemical reaction species separately to reduce complexity.

4.3.2.1 Volumetric Reactions

4.3.2.2 Species Transport Equations

The species transport equations for the evaporation process was presented in a previous Eq. (4-8). This equation needs to be modified for the process involving chemical reaction as follows.

The local mass fraction of each species Y_i can be predicted through the solution of a convention-diffusion equation for the *i-th* species. The equation takes the following general form [3]:

$$\frac{\partial}{\partial t}(\rho Y_i) + \nabla.(\rho \vec{v} Y_i) = -\nabla.\vec{J_i} + R_i + S_i \tag{4-9}$$

where R_i is the net rate of production of species i by chemical reaction, S_i is the rate of reaction by addition from the dispersed phase and, $\vec{J_i}$ is the flux of species *i*.

4.3.2.3 Mass Diffusion

The diffusion flux of species i (J_i in Eq. (4-9)) is due to gradients of concentration and temperature. Assuming laminar flux due to the typically low Re number of flow within the droplet, mass diffusion due to concentration gradients is modeled using the Fick's law, giving the flux:

$$\vec{J_i} = -\rho D_{i,m} \nabla Y_i - D_{T,i} \frac{\nabla T}{T} \tag{4-10}$$

where $D_{i,m}$ is the mass diffusion coefficient for species i in the mixture, and $D_{T,i}$ is the thermal diffusion coefficient.

4.3.2.4 The Laminar Finite Rate Model

The laminar finite rate model computes the chemical source term using the Arrhenius expression, and ignores the effect of turbulent fluctuations [4]. The net source of chemical species *i* due to reactions is computed as the sum of the Arrhenius reaction sources over the N_R reactions in which the species participate, thus:

$$R_i = M_{w,i} \sum_{r=1}^{N_R} \hat{R}_{i,r} \tag{4-11}$$

where $M_{w,i}$ is the molecular weight of species *i* and $\hat{R}_{i,r}$ is the Arrhenius molar rate of creation/destruction of species *i* in reaction *r*. The reaction occurs in the continuous phase at the wall surface.

Consider the *r-th* reaction written in the general form:

$$\sum_{i=1}^{N} \nu'_{i.r}\,\mathcal{M}_i \leftrightharpoons^{k_{f,r}}_{k_{b,r}} \sum_{i=1}^{N} \nu''_{i.r}\mathcal{M}_i \tag{4-12}$$

where:

N = Number of chemical species in the system

$\nu'_{i,r}$ = stoichiometric coefficient for reactant *i* in reaction *r*

$\nu''_{i,r}$ = stoichiometric coefficient for product *i* in reaction *r*

$\mathcal{M}_i$= Symbol denoting species *i*

$k_{f,r}$ = forward rate constant for reaction r

$k_{b,r}$ = backward rate constant for reaction r

This equation is valid for both reversible and non-reversible reactions. For non-reversible reactions, the backward rate constant, $k_{b,r}$ is omitted.

The forward rate constant for each $k_{f,r}$ is computed using the Arrhenius expression:

$$k_{f,r} = A_r T^{\beta_r} e^{(-\frac{E_r}{RT})} \tag{4-13}$$

where:

A_r = pre-exponential factor

β_r = temperature exponent

E_r = activation energy for the reaction (J/kmol)

R = universal gas constant (J/kmol)

The Arrhenius expression contains parameters A_r and β_r that must be set based on the experimental data. The parameters are obtained for Eq. (4-1) from a previous study [6] as $A_{r,\ SnO2} \sim 10^{12}$, and $\beta_{r,\ SnO2}$ =0.5. The parameters for Eq. (4-3) are [7] $A_{r,In2O3} \sim 10^6$ and $\beta_{r,In2O3} = 0.5$. The reactions are considered to start with equal initial concentration.

The reaction rate is defined on a volumetric basis and the rate of creation and destruction of chemical species becomes a source term in the species conservation equations. For surface reactions, the rate of adsorption and desorption is governed by both the chemical kinetics and the diffusion to and from the surface.

4.4 Results

Figure 4-3 shows the predicted velocity vectors in the computational domain. The droplet is clearly outlined in the figure. There is flow circulation inside the droplet due to convection from the heated surface. The convective flow is particularly strong near the 3-phase contact point at the end of the droplet attachment to the surface due to amplification by the local high surface energy between the vapor and water there. Wakes also develop on the droplet surface at the point of attachment to the substrate due to temperature gradient between the heated surface and the surrounding air. Specifically, this wake results from the interaction between water vapor on the droplet surface and the diffusive motion of the surrounding heated air.

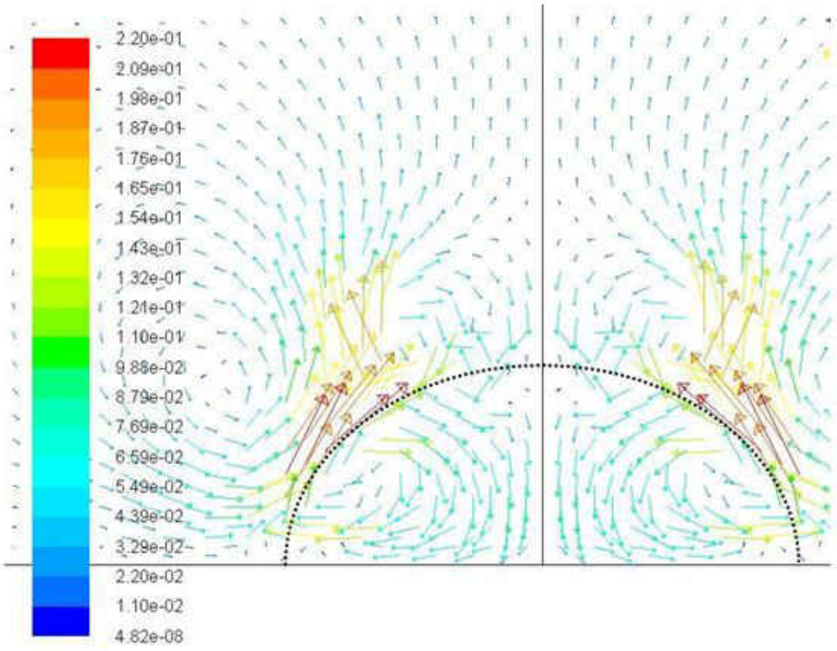

Figure 4-3 - Predicted velocity vectors within and outside the droplet.

Figure 4-4 shows the variation of droplet surface height (H) with radius as a function of time. The height and radius have been normalized by H_o and R_o respectively, in which H_o is the initial height of droplet and R_o is the initial radius of droplet. The Parameter t* is a dimensionless time defined as $t^* = t.(V_o/D_o)$ where V_o and D_o are the initial velocity and diameter of droplet respectively. The droplet initially spreads along the surface ($0< t^*<0.018$) when evaporation rate is relatively small. As the evaporation rate intensifies especially at the center of the droplet, the droplet deforms and the height decreases in the range ($0.18< t^*<0.252$). The droplet diameter correspondingly starts to decrease, implying the termination of spreading and onset of shrinkage.

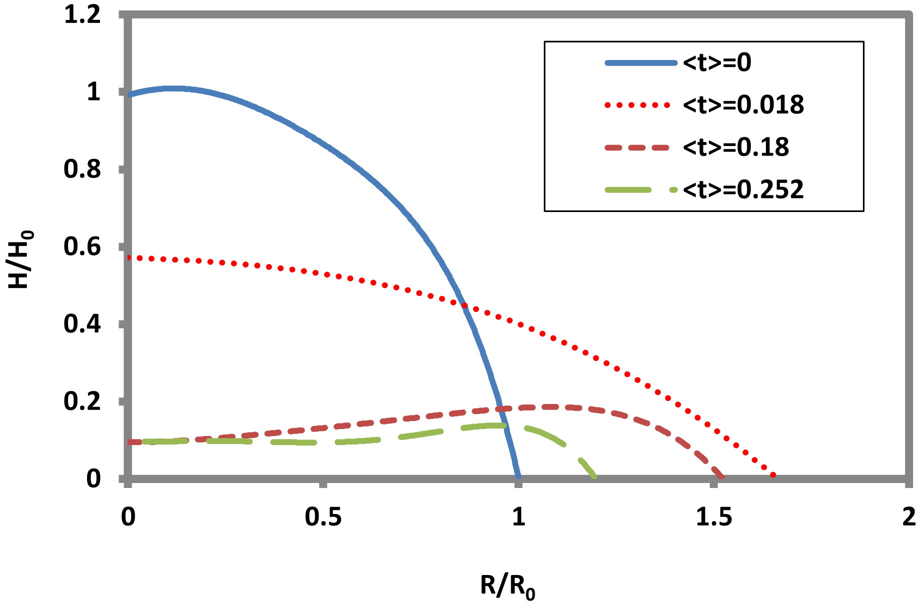

Figure 4-4 - Transient variation of droplet boundary height with radius.

Figure 4-5 shows the transient variation of droplet height normalized by the initial height H_0. There is initially a rapid decrease in droplet height due to the spreading on the surface (0< t*<0.03). Next the height decreases more gradually (0.03< t*<0.018), and remains almost constant (0.18< t*<0.22), before gradually decreasing again (0.22< t*<0.252). When the droplet is almost flat, the rate of height reduction starts to decrease. These trends are consistent with evaporation occurring mainly from the 3-phase contact point at the edges due to the high temperature and not from the center of the droplet.

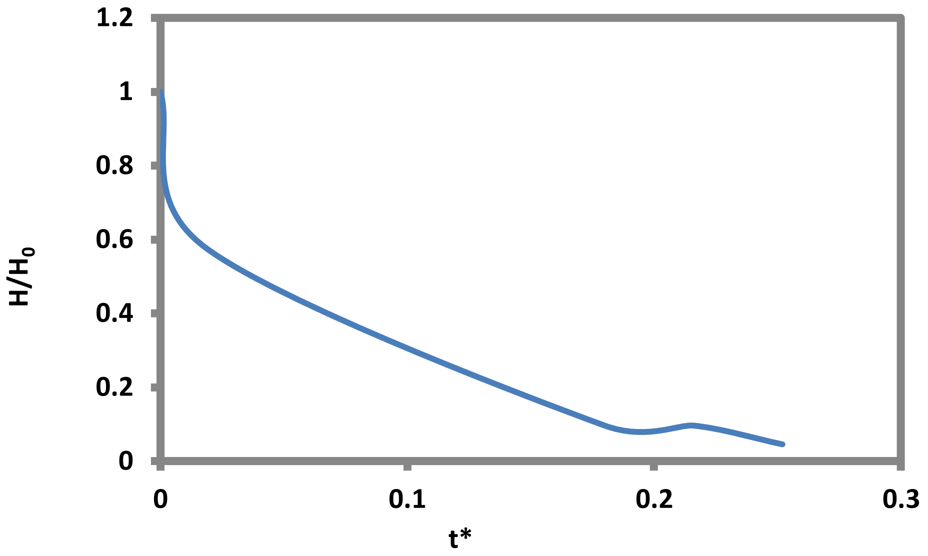

Figure 4-5 - Transient variation of normalized droplet height.

Figure 4-6 shows the corresponding transient variation of droplet radius at the 3-phase contact point. The radius has been normalized by the initial value R_o. The results indicate initial rapid increase in radius (up to t* = 0.018) as the droplet spreads along the surface immediately after impact. This trend is consistent with the initial rapid decrease in droplet height observed previously in Figs. 4-4 and 4-5. Next, the radius gradually decreases (i.e. the droplet shrinks laterally) due to intense evaporation that originates from the contact line. This trend continues until t* = 0.18 when the droplet is nearly flat on the substrate. Subsequently the contact line shrinks very fast until the droplet is completely evaporated.

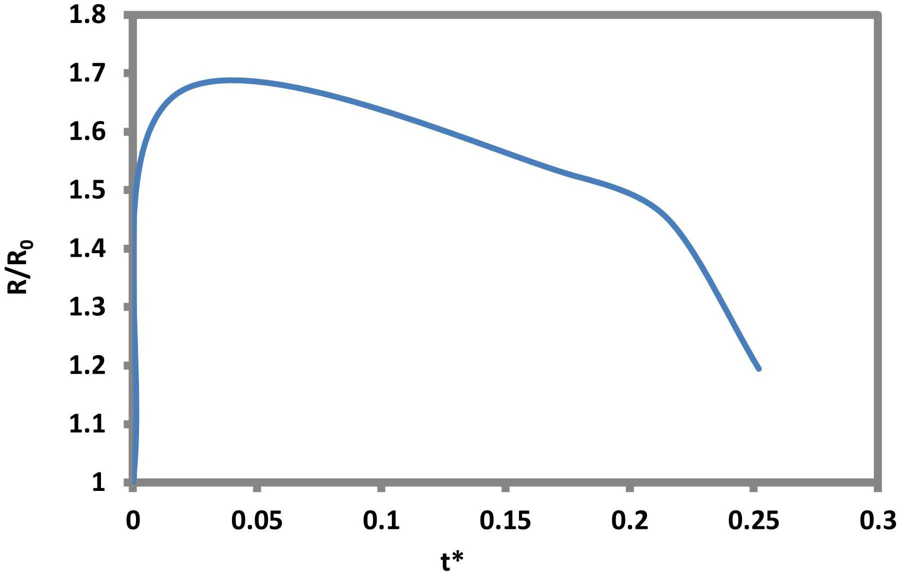

Figure 4-6 - Transient variation of normalized droplet radius.

Figure 4-7 shows the temperature distribution in the computational domain investigated at t* = 0.18. Preliminary calculations indicate that t* = 0.18 is the threshold duration over which the droplet resides on the substrate before evaporation occurs. There is observed a temperature gradient on the droplet surface which produces the velocity wakes around the droplet that was observed in a previous Fig. 4-3. The temperature is also much higher at the midpoint along the droplet surface.

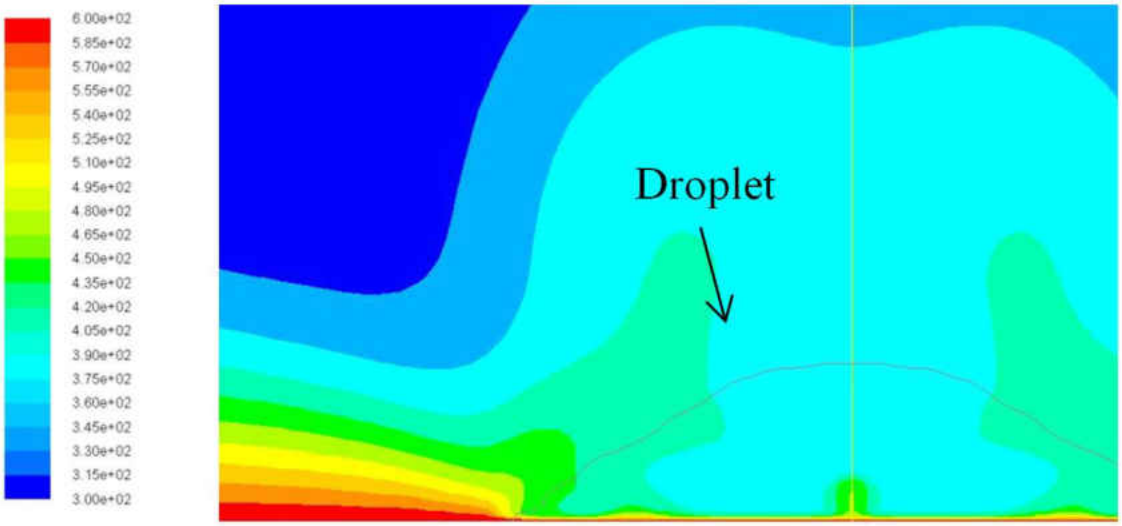

Figure 4-7 - Temperature distribution at $t^* = 0.18$.

Figure 4-8 shows the temperature variation along the centerline of the droplet from substrate ($H/H_o = 0$) to the free surface ($H/H_o = 1$). The temperature is observed to be highest near the heated substrate and lowest at the free surface of the droplet. The profile exhibits four distinct zones. In Zone 1 ($0<H/H_o<0.05$) near the substrate, the temperature decreases sharply away from the substrate due to convection inside the droplet as observed in Fig. 4-7. Liquid circulation causes temperature homogeneity inside the droplet. However at the center of the droplet, there is reduced circulation which allows the water there to be heated to initiate evaporation. The heating decreases away from the center. In Zone 2 ($0.05<H/H_o<0.22$), the temperature is nearly constant because the inside of the droplet has not been affected by the decreasing surface temperature due to evaporation. In Zone 3 ($0.22<H/H_o<0.3$) there is again a steep temperature gradient due to phase change from liquid to air/vapor. Finally, in Zone 4 ($H/H_o>0.3$), the temperature is essentially constant due to reduced influence of the heated surface on the surrounding air.

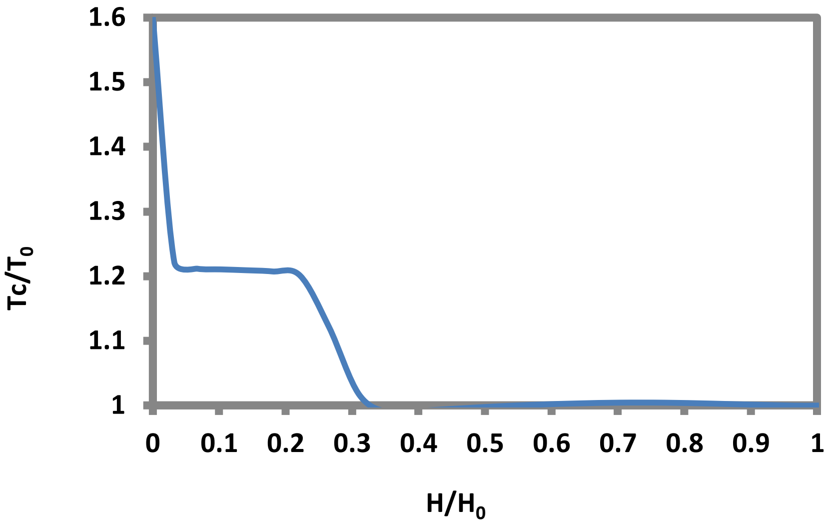

Figure 4-8 - Temperature distribution along centerline of droplet at t* = 0.18.

Figure 4-9 shows the radial variation of temperature on the droplet surface at t*= 0.18 which indicates the time when droplet height remains nearly invariant. The temperature gradually increases from the apex of the droplet ($R/R_o = 0$) to the edge (i.e. the 3-phase contact line). The temperature gradient is particularly steep near the contact line in the consensus of the previous Fig. 4-7. This trend may be attributed to the high temperature and the low thermal conductivity of the substrate.

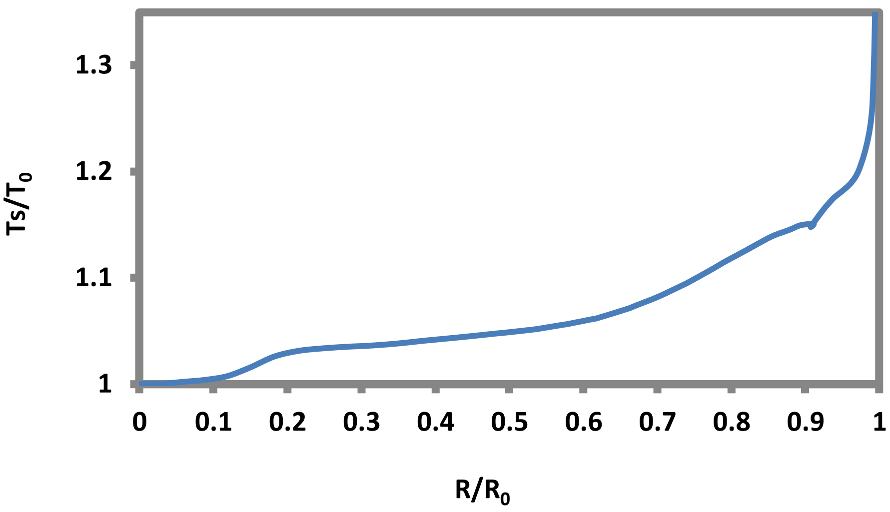

Figure 4-9 - Temperature distribution on droplet surface at t*= 0.18.

The results of the chemical reaction are presented below. Only the results for one of the two oxides formed (SnO_2) are presented for brevity since the normalized features are similar for SnO_2 and In_2O_3. The transient variation of molar concentration of SnO_2 in the droplet is presented in Fig. 4-10. The concentration generally increases with time as the evaporation rate decreases.

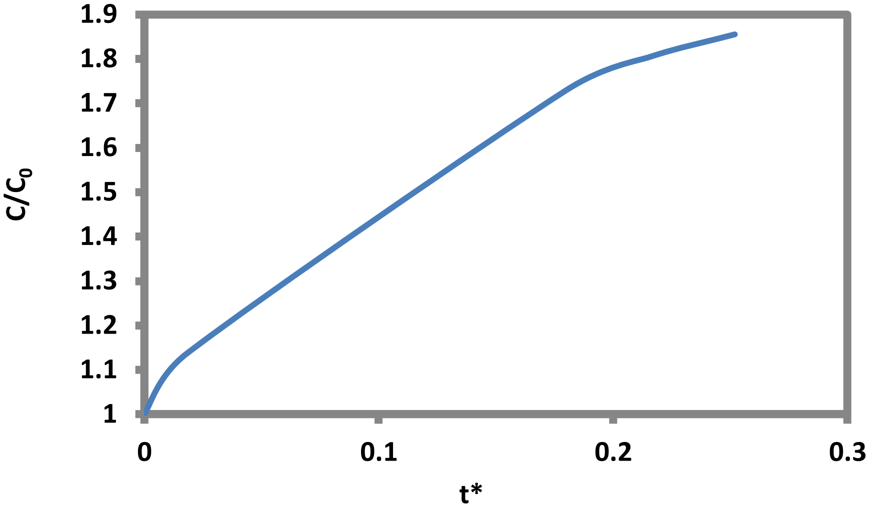

Figure 4-10 - Transient variation of precursor SnO_2 concentration.

Figure 4-11 shows the chemical reaction rate profile for the reaction associated with the deposition of SnO_2 of the mixed oxide In_2O_3+SnO_2 on the substrate within the domain of the droplet. Figure 4-12 shows the corresponding variation of chemical reaction rate with radius. Both figures show that the chemical reaction rate is nearly constant from the center to about 60% of droplet radius. This implies that the chemical reaction is homogenous within most of the droplet. At $0.6<r<0.95$ the rate decreases linearly. The observed trend is because most of the heat conduction occurs near the center of the droplet and the convention inside the droplet enhances both evaporation and reaction. Near the edge of the droplet ($r>0.95$) the reaction rate increases slightly due to larger convection of hot air near the contact line. This circulation enhances both evaporation and heat conduction to the droplet at the vicinity of the contact line.

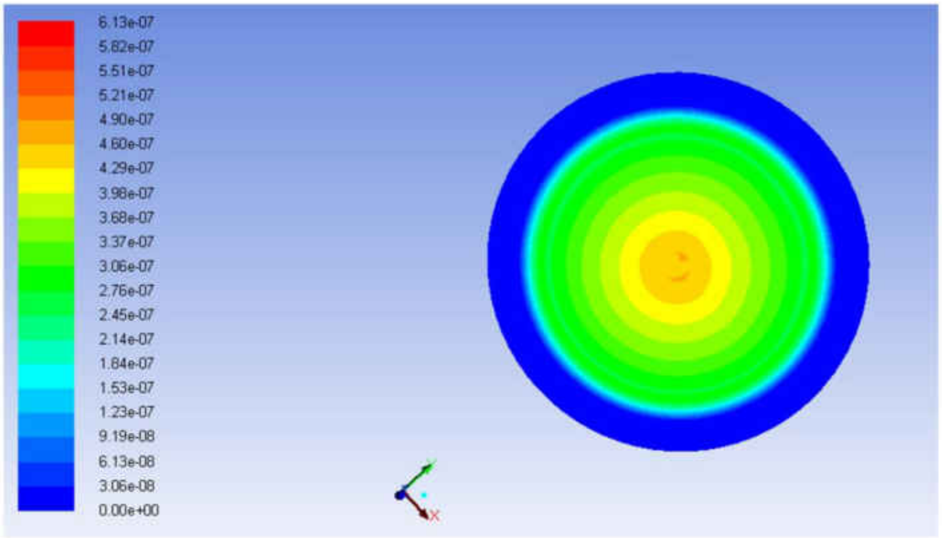

Figure 4-11 - Contour of chemical reaction rate of deposition of SnO_2 on substrate within droplet domain.

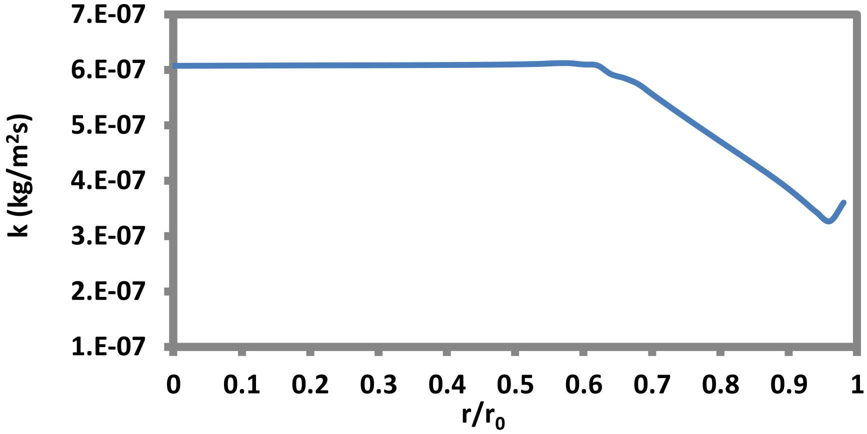

Figure 4-12 - Chemical reaction rate of deposition of SnO_2 on substrate within droplet domain.

Figures 4-13 and 4-14 show the corresponding deposition of SnO_2 of the mixed oxide In_2O_3+SnO_2 on the substrate. The results are consistent with those obtained for chemical reaction rates of SnO_2 in Figs. 4-11 and 4-12. Specifically, the deposition rate correlates with the chemical reaction rate. The highest deposition occurs again at $0<r<0.6$ and $r>0.95$.

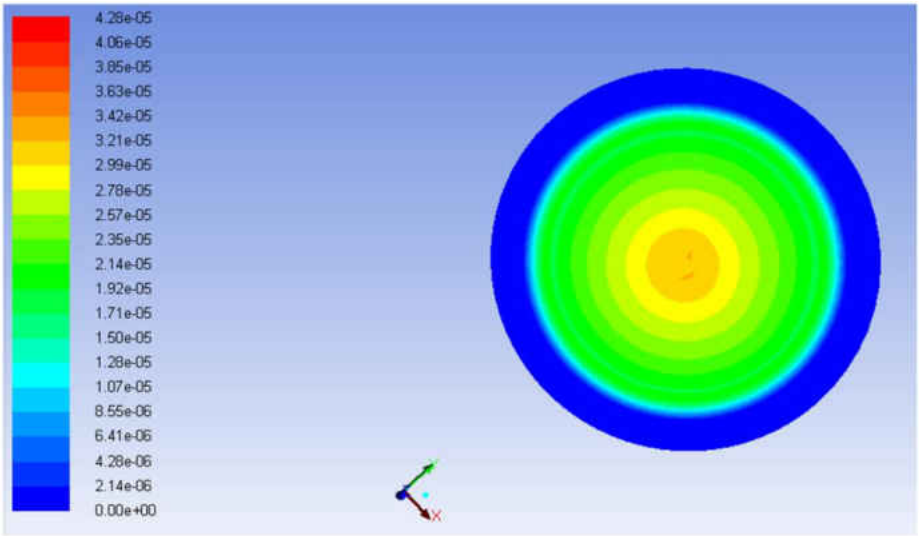

Figure 4-13 - Contour of deposition of SnO_2 on substrate within droplet.

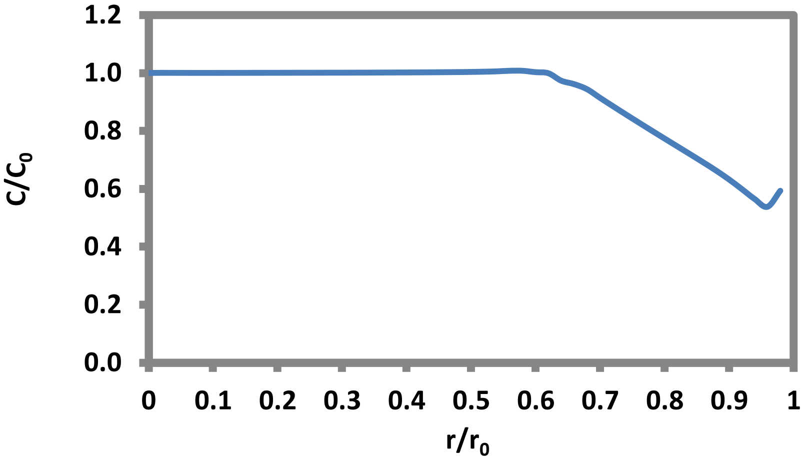

Figure 4-14 - Normalized deposition rate of SnO_2 on substrate within droplet.

Figures 4-15 and 4-16 show the predicted radial variation of mass fraction of reactant $SnCl_4$ associated with the SnO_2 component of the mixed oxide In_2O_3+SnO_2 on the substrate after completion of chemical reaction. Initial mass fraction was achieved based on the results of a previous stud [8-9]. There is a significant amount of unused $SnCl_4$ at $r>0.6$. This result is again consistent with the predicted higher reaction rate in the middle of the droplet compared to the edges that was observed in previous Figs. 4-11 and 4-12.

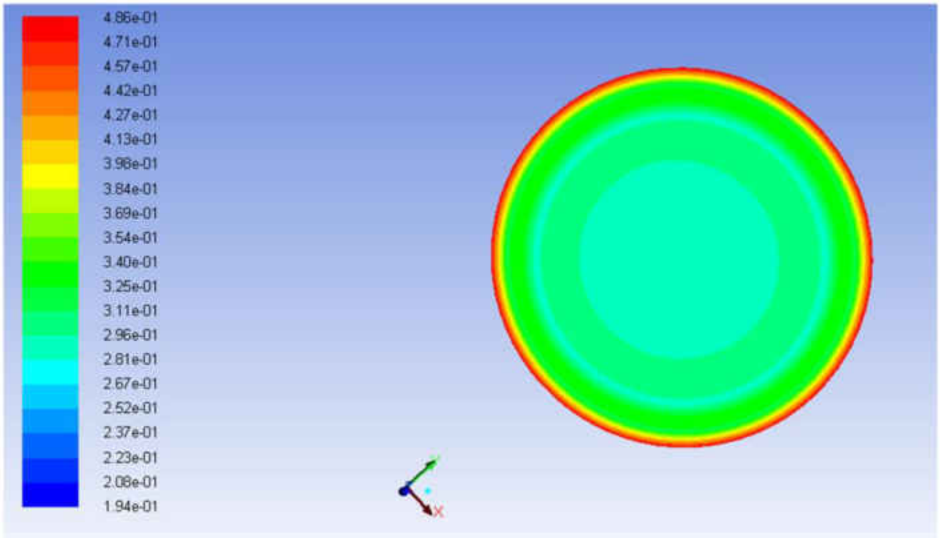

Figure 4-15 - Contour of mass fraction of $SnCl_4$ on substrate within droplet domain after completion of reaction.

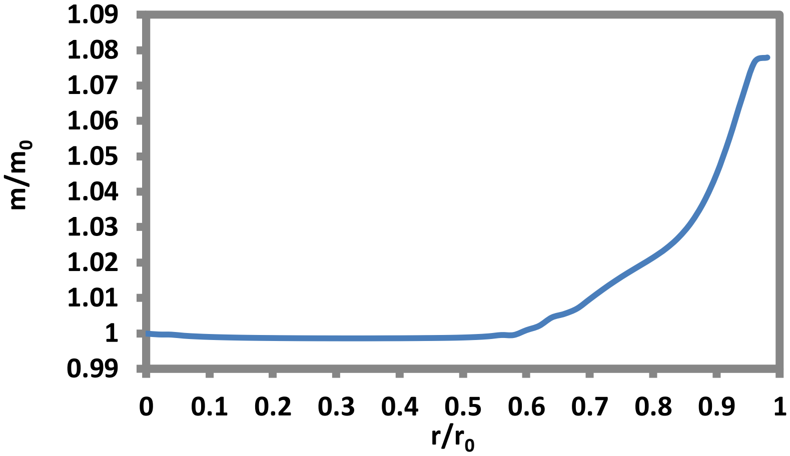

Figure 4-16 - Normalized mass fraction of $SnCl_4$ on substrate within droplet domain after completion of reaction.

4.5 Conclusion

A numerical study has been performed for a droplet sprayed from a nozzle, deposited and evaporated on a heated flat substrate surface. The model involves solving the time dependent governing equations of continuity, momentum, energy, species concentration, and chemical reaction. The model also considers surface tension, wall adhesion, gravitational body force, and evaporation.

The predicted results show that the droplet behavior after impingement occurs in stages, depending on the degree and location of significant evaporation. First the droplet spreads rapidly radially along the substrate due to force balance between surface force and droplet weight. The contact angle decreases and the spreading rate increases. The apex height starts to oscillate and the amplitude of oscillation decreases with time due to viscous dissipation. Subsequently, with more evaporation, the contact angle and apex height remains nearly constant while the three-phase contact line decreases and the droplet shrinks laterally.

The predicted temperature variation on the droplet surface and near the substrate correlates with the observed convection of fluid inside the droplet. The roll cells resulting from this convection sustains the evaporation rate at the early stages. Evaporation rate decreases as the droplet gradually flattens on the substrate and can no longer sustain the roll cells.

The results of chemical reaction model assuming surface reaction show that the reaction occurs homogenously inside most of the droplet. There is a constant reaction rate within about 60% radius of the droplet from the interior. Beyond that, the reaction rate decreases linearly away from the center. The reaction rate is partially high at the contact line of droplet with the substrate. Oxide deposition is concentrated within the 60% radius from the center and there is a significant amount of unused reactants thereafter.

4.6 List of References

1. Perednis, D. and Gauckler, L. J. (2005). Thin film deposition using spray pyrolysis. *Journal of Electroceramics*, *14*(2), pp. 103-111.
2. Wilms, J. (2005) Evaporation of Multicomponent Droplets, Doctoral dissertation, University of Stuttgart, Germany.
3. ANSYS FLUENT 12.0, User's Guide, www.ansys.com, April 2009.
4. ANSYS FLUENT 12.0, Theory Guide, Chapter 15. Discrete Phase, www.ansys.com, April 2009.
5. Briones, A. M., Ervin, J. S., Putnam, S. A., Byrd, L. W., & Gschwender, L. (2010). Micrometer-sized water droplet impingement dynamics and evaporation on a flat dry surface. *Langmuir*, *26*(16), 13272-13286.
6. van Mol, M. B. (2003). Chemical Vapour Deposition of Tin Oxide Thin Films, Doctoral dissertation, Eindhoven University of Technology, Netherlands.
7. Lin, S. E. and Wei, W. C. J. (2008). Synthesis and investigation of submicrometer spherical indium oxide particles. *Journal of the American Ceramic Society*, *91*(4), pp. 1121-1128.
8. Khatami, S. M. N., & Ilegbusi, O. J. (2011, January). Modeling of Aerosol Spray Characteristics for Synthesis of Mixed-Oxide Nanocomposite Sensor Film. In: *ASME 2011 International Mechanical Engineering Congress and Exposition,* pp. 581-589.
9. Khatami, S. M. N., Ilegbusi, O. J. and Trakhtenberg, L. (2013). Modeling of aerosol spray characteristics for synthesis of sensor thin film from solution. *Applied Mathematical Modelling*, *37*(9), pp. 6389-6399.

CHAPTER 5: PROCESSING OF SINGLE AND MIXED METAL -OXIDE THIN FILMS

5.1 Overview

In this chapter, the influence of deposition parameters is investigated on the structural characteristics of nanoheterogeneous single and mixed oxides produced by spray pyrolysis technique. The films were synthesized by spraying precursor solutions through a nozzle onto a heated alumina substrate. The precursor consisted separately of aqueous solutions of tin chloride for SnO_2, and zinc chloride for ZnO single oxide deposition. For mixed oxide cases, aqueous solutions of tin chloride and indium nitrate were mixed and used for deposition of SnO_2+In_2O_3, while zinc chloride and indium nitrate solutions were used for deposition of ZnO+In_2O_3. The substrate temperature was varied from 350° C to 450° C for ZnO, and 350° C to 500° C for SnO_2. The temperature was set at 400° C for ZnO+In_2O_3 and 500° C for SnO_2+In_2O_3. The films produced were characterized by X-ray Photoelectron Spectroscopy and Scanning Electron Microscopy. The X-ray diffraction data show that the SPT process results in polycrystalline films of hexagonal wurtzite types. The morphology of the synthesized films is studied by scanning electron microscopy as well as the dependence of morphology on the synthesis conditions, specifically the temperature of the aerosol precipitation and the concentration of the precursors in solutions. The results indicate that a non-homogenous film is formed at low temperature for both single oxides considered. The temperature has significant effect on the composition of the synthesized films of both single oxides below 450° C. The characteristics of nucleation and growth of oxide crystals during the synthesis of mixed oxide composite films are also considered. The results for mixed oxides show that the best homogeneous films are obtained for

80 wt. % ZnO + 20 wt. % In_2O_3, and 80 wt. % SnO_2 + 20 wt. % In_2O_3. However, the film with the composition 25 wt% ZnO+75 wt% In_2O_3 contains a large number of small crystal aggregates of arbitrary shape with a high density of contacts between the aggregates and are characterized by a homogeneous structure with high dispersion. Such morphology has high specific surface, which favors high sensory response. In addition, in this range of aggregate composition the relationship between the particles of the catalytically active component – ZnO, cleavage of hydrogen molecule, and In_2O_3 particles with a high concentration of conduction electrons is close to optimal for the maximum sensory effect in the detection of hydrogen.

5.2 Experiments Performed

5.2.1 *Deposition Mechanism*

A precursor solution which contains constituent reactant compounds is atomized in a nozzle to tiny droplets which are then sprayed onto a preheated substrate. The surface of the substrate must be sufficiently hot to initiate chemical reaction between the precursors in the droplet solution. Specifically, the droplet must still contain enough reactants in solution after reaching the substrate [1-2]. A film of stable compounds subsequently forms that adheres to the substrate due to chemical reaction and thermal decomposition of the solution.

5.2.2 *Experimental Procedure*

The importance of spray parameters and their effects were investigated completely in chapter 3. The results are used to determine experimental conditions to synthesis thin films through spray system.

Zinc oxide was deposited using aqueous solution of zinc chloride ($ZnCl_2$) precursor while tin oxide utilized tin chloride ($SnCl_4$) precursor solution in water. In order to deposit mixed oxides, tin chloride and indium nitrate were dissolved together in water to synthesize $SnO_2+In_2O_3$. Zinc chloride and indium nitrate were used for deposition of $ZnO+In_2O_3$ for different composition ratios. The chemical reactions were previously formulated in chapter 4, Eqs. (4-1), (4-2), and (4-3) [3]. It should be noted that the reaction of tin chloride solution is a heterogeneous reaction that occurs in the vapor phase [4].

Each precursor was fed into a 2 mm-diameter duct at a flow rate of 1 ml/min [5]. The solution was injected through a 1 mm-diameter round spray nozzle and then atomized at 1 bar air pressure. The solution in the nozzle was then sprayed onto a heated aluminum oxide (Al_2O_3) coated substrate. The distance between the spray nozzle and the hot substrate was kept constant at 10cm for the experiments. This distance was chosen based on the results of previous studies [1, 6]. The thin film was finally annealed for 30 minutes after deposition to the desired structures at 450° C [7-9]. The annealing process promotes adhesion of the film to the substrate. These conditions were kept constant for all other sets of experiments performed. Figure 5-1 is the experimental setup used for the deposition of thin films in this research.

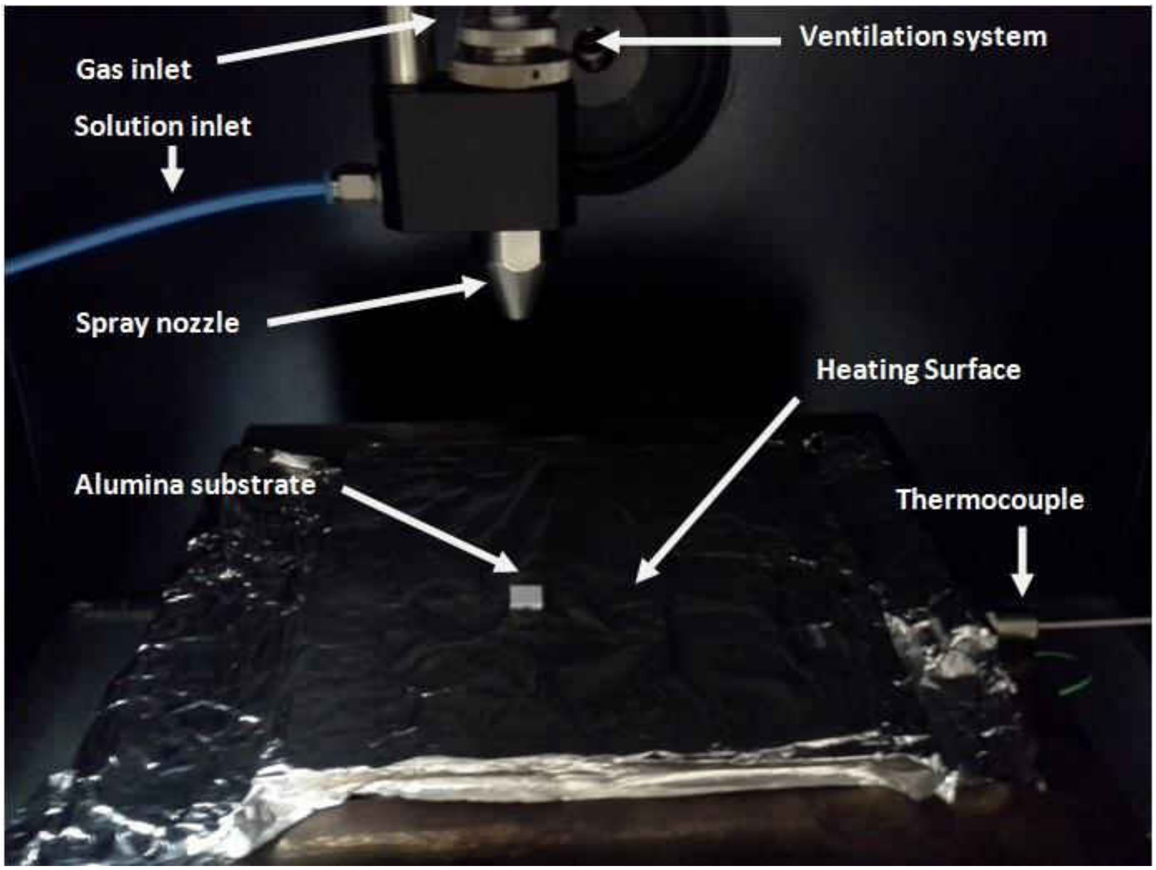

Figure 5-1 – Experimental apparatus.

5.2.3 Control Parameters

The substrate Temperature (T_s) and solution concentration (C) were used as the control parameters. In order to assess the results of mixed oxide deposition, the optimum case from single oxide deposition was also considered. The experimental parameters are chosen and determined based on previous studies which were explained thoroughly in chapter 2, section *2.4.2*.

Two sets of experiments were designed for deposition of ZnO. In the first set of experiments (Cases 1 and 2), the concentration was maintained constant (C=0.1 mol/lit) while the temperature was varied from 400° C to 450° C. In the second set (Cases 3 and 4), the concentration was increased from C=0.2 mol/lit for Case 3 to 0.3 mol/lit for Case 4 while the temperature was constant at 400° C [10].

The same approach was used for deposition of SnO_2. In the first set (Cases 5 to 8), the substrate temperature (T_s) was varied from 350° C to 500° C at 50 degrees increments for different sets of experiments while the concentration was constant at 0.25 mol/lit. In the second set (Cases 9 and 10), the temperature was kept constant at 450° C while the concentration was varied from 0.1 to 0.5 mol/lit [11-12].

In order to deposit mixed oxide films, the precursor concentration ratio was changed for new sets of experiments. Indium nitrate was mixed with zinc chloride to produce 25 wt. % ZnO + 75 wt. % (Case 11) and 80 wt. % ZnO + 20 wt. % In_2O_3 (Case 12). For these cases, temperature and solution concentration were kept constant at 400° C and 0.1 mol/lit, respectively. For deposition of SnO_2+In_2O_3, indium nitrate was added to produce 80 wt. % SnO_2 + 20 wt. % (Case 13) and 95 wt. % SnO_2 + 5 wt. % In_2O_3 (Case 14).

5.2.4 Material Characterization

The deposited thin films were characterized by X-ray photoelectron spectroscopy (XPS) and Scanning electron microscopy (SEM). Surface morphology was studied using a Zeiss ULTRA-55 FEG SEM system which used Schottky field emission source with a resolution of 1 nm @ 15 KV and 1.7 nm @ 1 KV and STEM detector. Surface spectroscopy was performed by Physical Electronics 5400 ESCA system to detect elemental composition.

5.3 Results

Table 5-1 summarizes the various cases considered and the corresponding substrate temperature (T_s), precursor concentration (C) and the observed morphology for the various films produced. The results show that the resulting film structure is strongly dependent on the deposition temperature in each case. However the qualities of films were found to be enhanced by systematically increasing the precursor concentration. The effect of these two processing parameters is investigated in this section.

Table 5-1 - Film morphology of deposited films.

Case	**Film Composition**	**Temperature T_s (°C)**	**Concentration C (mol/lit)**	**Film Morphology**
1	ZnO	400	0.1	granular
2	ZnO	450	0.1	dense
3	ZnO	400	0.2	columnar
4	ZnO	400	0.3	columnar
5	SnO_2	350	0.25	dense
6	SnO_2	400	0.25	non-homogenous
7	SnO_2	450	0.25	porous
8	SnO_2	500	0.25	dense
9	SnO_2	450	0.1	dense
10	SnO_2	450	0.5	granular
11	25 wt. % ZnO+75 wt. % In_2O_3	0.1	400	columnar
12	80 wt. % ZnO+20 wt. % In_2O_3	0.1	400	columnar
13	80 wt. % SnO_2+20 wt. % In_2O_3	0.25	450	granular
14	95 wt. % SnO_2+5 wt. % In_2O_3	0.25	450	dense

5.3.1 Single Oxides

5.3.1.1 Effect of Substrate Temperature

Figure 5-2 shows the SEM micrographs of ZnO films (Cases 1 to 4). Figures 5-2(a) and 5-2(b) show the deposition of ZnO at low concentration (C=0.1 mol/lit) and different temperatures (T=400° C and T=450° C) while Figs. 5-2(c) and 5-2(d) show the deposition at constant temperature (T=400° C) and higher concentrations (C=0.2 mol/lit and C=0.3 mol/lit), respectively.

Figure 5-2(a) (Case 1: T=400° C and C=0.1 mol/lit) shows that small spherical crystallites are formed that agglomerate at the surface in the shape of powder with an average size of ~ 50 *nm* in the consensus of previous studies [13-15]. In Fig. 5-2(b) (higher temperature of T=450° C), the film uniformity is enhanced due to the progression of chemical reaction at the higher temperature. The film is denser and the growth rate is highly limited by diffusion. The results are in good agreement with a previous study [16].

Temperature has similar effect on the deposition of SnO_2 film (cases 5 to 10). Table 5-1 shows that a dense film is formed at the lowest temperature (Case 5, 350° C). This result may be attributed to the limited evaporation of the droplets reaching the surface at low temperature. Some cracks are observed in the film due to thermal stress during the annealing process [17]. In addition, the precursor solution does not have sufficient time to form a continuous film on the Al_2O_3 substrate. As the temperature increases, a non-stoichiometric film with rough aspect ratio is formed (Table 5-1, Case 6). In this case, the nucleation process is faster due to the higher temperature [18] and a film with a non-homogenous structure is synthesized which is similar to the previous ZnO films deposited at low temperature (Fig. 5-2, Case 1).

Figure 5-3 shows the SEM micrographs of some SnO_2 films produced (Cases 7 to 10). Figures 5-3(a) and 5-3(b) show the deposition of SnO_2 at low concentration (C=0.25 mol/lit) and different temperatures (T=450° C and T=500° C) while Figs. 5-3(c) and 5-3(d) show the deposition at constant temperature (T=450° C) and different concentrations (C=0.1 mol/lit and C=0.5 mol/lit).

Figures 5-3(a) (T=450° C) and 5-3(b) (T=500° C) show thin films with continuous structure at both temperatures while the precursor solution is constant at C=0.25 mol/lit. At 450° C (Fig. 5-3(a)), the deposited film exhibits porous structure which prevents homogeneity. Such a characteristic porous microstructure has also been observed in a previous study [8]. The pore sizes are in the sub-micron range. The increase in porosity can be attributed to increased temperature and the film becomes denser without cracks at higher temperature [17], as observed in Fig. 5-3(b). In this case, the pores shrink and the film surface subsequently becomes smooth.

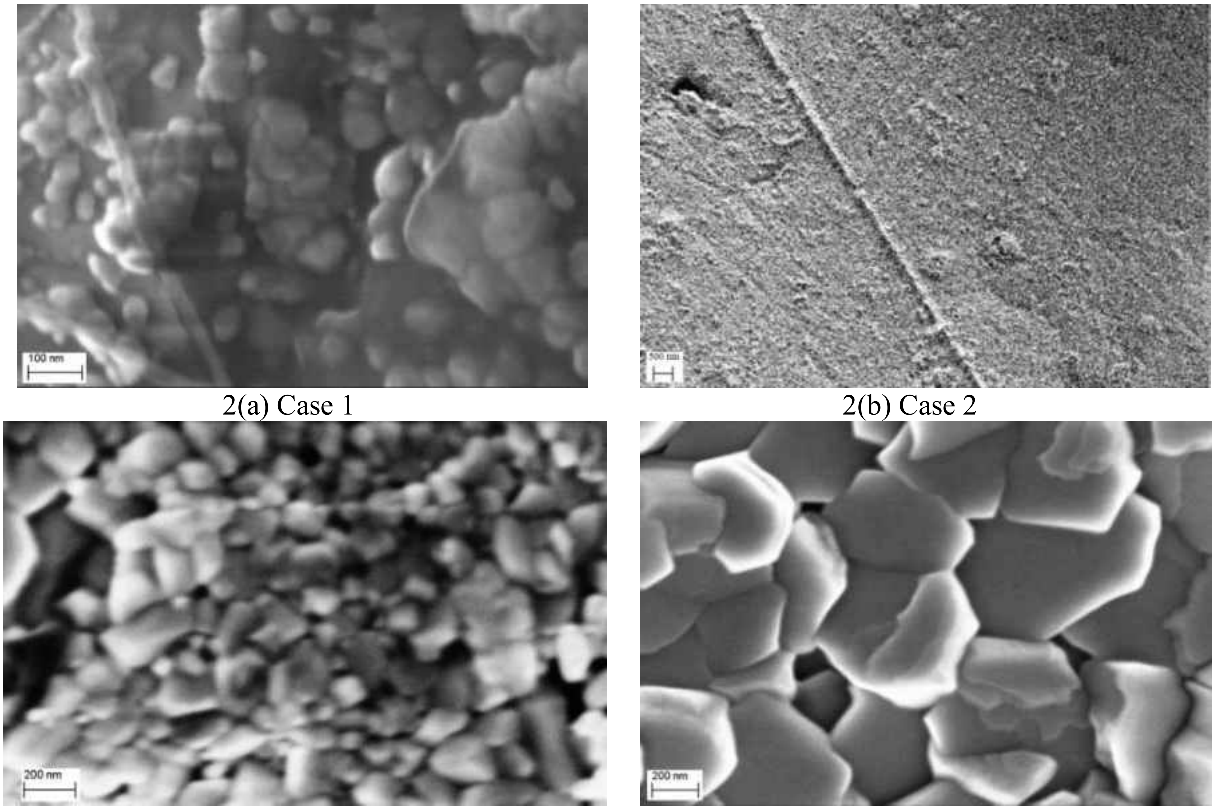

2(a) Case 1 2(b) Case 2

2(c) Case 3 2(d) Case 4

Figure 5-2 - SEM micrographs of spray pyrolysis deposition of ZnO thin films on Al_2O_3 substrate: (a) T= 400° C and C=0.1 mol/lit; (b) T= 450° C and C=0.1 mol/lit; (c) T= 400° C and C=0.2 mol/lit; and (d) T= 400° C and C=0.3 mol/lit.

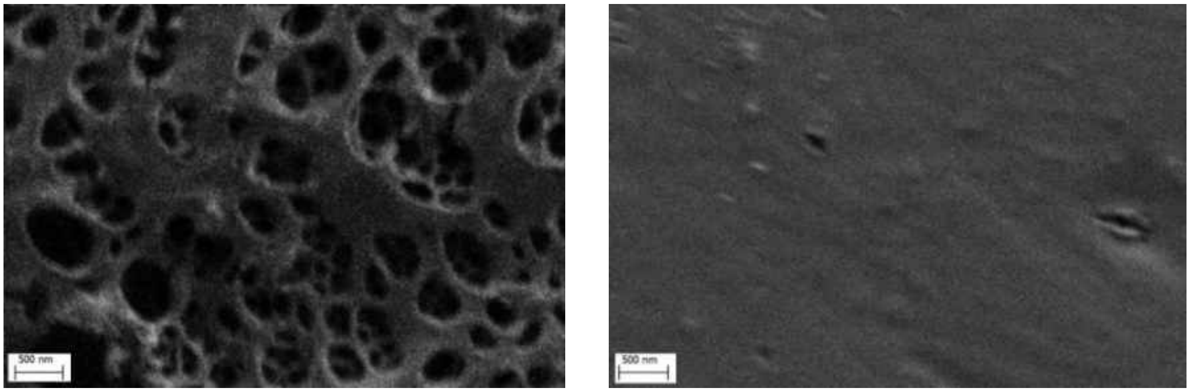

3(a) Case 7 3(b) Case 8

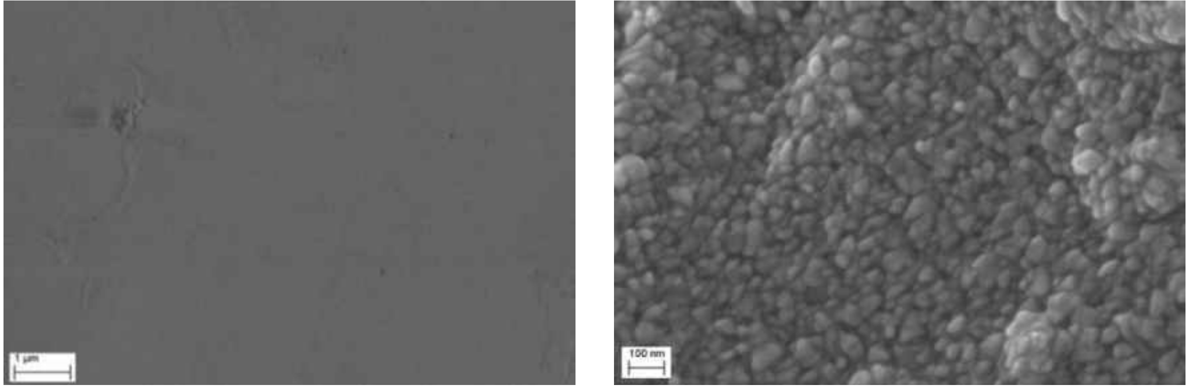

3(c) Case 9 3(d) Case 10

Figure 5-3 - SEM micrographs of spray pyrolysis deposition of SnO_2 thin films on Al_2O_3 substrate: (a) T= 450° C and C=0.25 mol/lit; (b) T= 500° C and C=0.25 mol/lit; (c) T= 450° C and C=0.1 mol/lit and (d) T= 450° C and C=0.5 mol/lit.

The compositions of the deposited films are determined by X-ray photoelectron spectroscopy (XPS). Figure 5-4(a) shows the XPS of ZnO film grown at 400° C (Case 1). The corresponding result at 450° C (Case 2) is shown in Fig. 5-4(b). ZnO deposition is clearly evident in both cases. However the atomic concentration of Zn increases from 0.9% at 400° C to 7.1% at 450° C due to the enhanced chemical reaction at the higher temperature. The peak of Zn $2P_3$ is associated with the Zn-O bond [16].

Figure 5-5 (a) and 5-5(b) show the XPS results for SnO_2 films deposited at 450° C (Case 7) and 500° C (Case 8). These results clearly confirm the formation and deposition of SnO_2 at both temperatures, and exhibit the same atomic concentration of Sn at both temperatures. The result therefore shows that the temperature appears to have minimal effect on the atomic concentrations above 450° C.

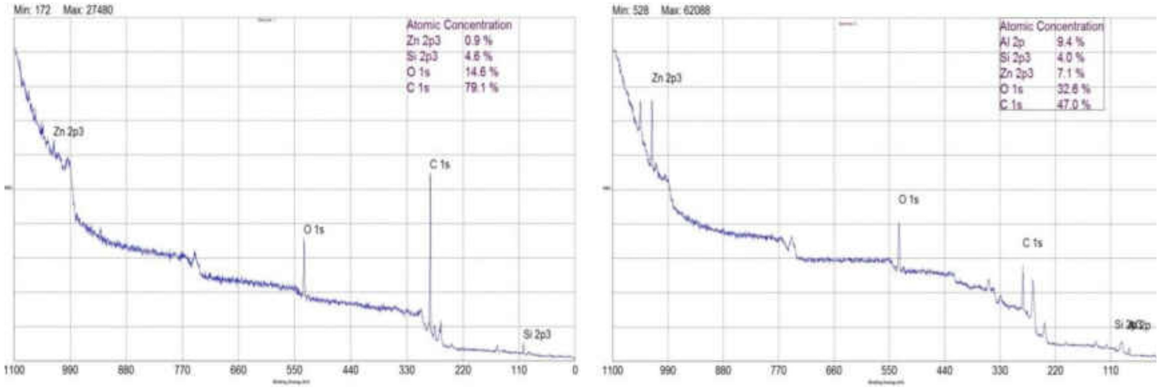

4(a) Case 1 4(b) Case 2

Figure 5-4 - XPS of ZnO thin film on Al_2O_3 substrate at (a) T=400° C and C=0.1 mol/lit; and (b) T=450° C and C=0.1 mol/lit.

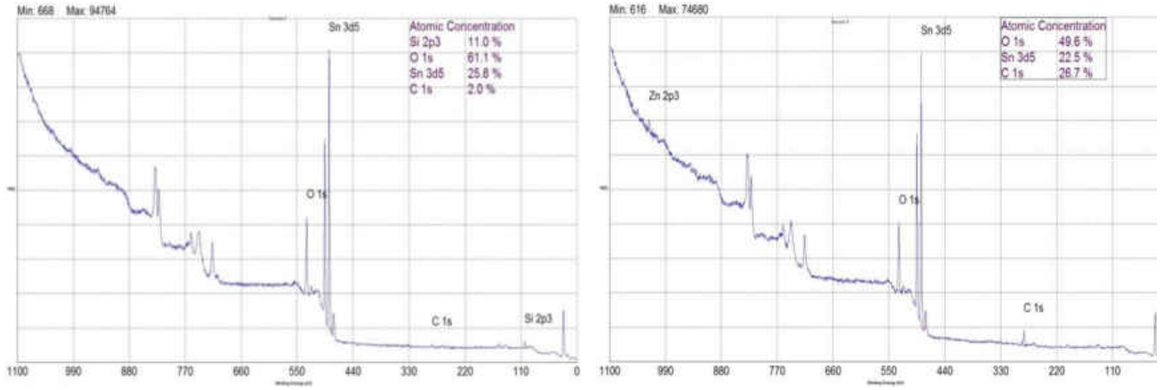

5(a) Case 7 5(b) Case 8

Figure 5-5 - XPS of SnO_2 thin film on Al_2O_3 substrate at (a) T=450° C and C=0.25 mol/lit; and (b) T=500° C and C=0.25 mol/lit.

5.3.1.2 Effect of Solution Concentration

The effect of concentration on deposition of ZnO are also presented in the previous Figs. 5-2(c) (Case 3: T=400° C and C=0.2 mol/lit) and 5-2(d) (Case 4: T=400° C and C=0.3 mol/lit). The results show that the grain size increases with increase in the amount of precursor dissolved in solution. The deposited grains tend to form crystalline shapes at higher concentrations (Fig. 5-

2(d)). Figure 5-2(c) shows that at a lower concentration, the film is uniform with nanoparticle sizes of ~ 100 *nm* with hexagonal flake-like morphology which is in the consensus of a previous study that utilized the same concentration of precursors [19]. When the concentration is increased, the density and size of particles are further increased. In Fig. 5-2(d), the crystals are plate-like and the sides of the walls are grown packed as was also observed in a previous study [20]. A larger size of grains was similarly observed at the higher concentration [21].

The effect of concentration on the deposition of SnO_2 can similarly be assessed by comparing Figs. 5-3(c) (Case 9: T=450° C and C=0.1 mol/lit) and 5-3(d) (Case 10: T=450° C and C=0.5 mol/lit). At low concentration, the grains form smooth, uniform thin film observed in Fig. 5-3(c). A previous study has shown that at low concentrations, the film surface is smooth with no well-defined crystallites [22]. However by increasing the concentration, the particles begin to agglomerate and form clusters. These particles have sharpened boundaries with spherical grain shapes [22]. A similar result can be observed in Fig. 5-3(d). Such a transition from an amorphous texture to a larger size of crystallites was also observed in a previous study [23]. The study attributed the observed trend to excess amount of surface-free energy at lower temperature which leads to formation of smooth film surface.

5.3.2 Mixed Oxides

Figures 5-6 and 5-7 show the SEM micrographs of $ZnO+In_2O_3$ and $SnO_2+In_2O_3$ thin films on Al_2O_3 substrate. Figures 5-6(a) and 5-6(b) are the results for $ZnO+In_2O_3$ at T= 400° C and concentration ratios of 25% of ZnO and 80% of ZnO respectively. It has been found that an un-doped ZnO film will form a non-uniform structure [24]. By doping with indium, the uniformity is enhanced and grain size is increased [24]. At low concentration ratio of ZnO (Fig. 5-6(a)), ZnO nano wires are formed. By increasing the amount of ZnO (from 25% in Fig. 5-6(a) to 80% in Fig. 5-6(b)), crystallization occurs and a well-structured thin film is produced. These results exhibit the same trend that was observed in the previous Fig. 5-2 for ZnO films. Thus by increasing the amount of zinc in solution, there is a better chance to produce zinc oxide crystals or rods. In Fig. 5-6(b), the growth of ZnO rods occurs fully due to the growth of side walls, resulting in the formation of nano tubes [20, 25-26]. By increasing the indium dopant, the grain size decreases. This trend is attributed to the stresses applied by the mixture which limits the growth of the grain size [27].

Figure 5-7 shows the SEM micrographs of SnO_2+In_2O_3 thin films deposited on Al_2O_3 substrate at T= 450° C and at a concentration ratio of 80% of SnO_2 and 95% of SnO_2 respectively. The results show that small spherical particles are formed at the low concentration of tin (Fig. 5-7(a)). When the concentration of tin is high (Fig. 5-7(b)), the synthesized film is similar to the single oxide thin film of Case 5, resulting in cracking and formation of a thick film.

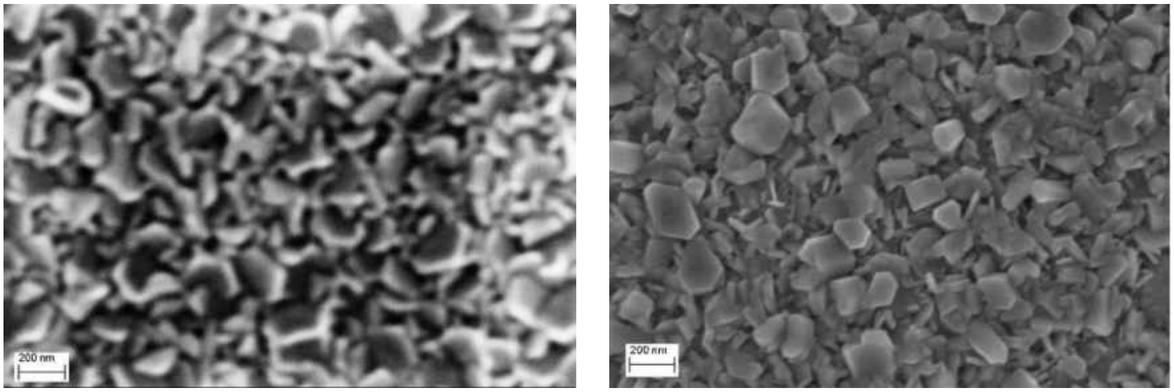

6(a) Case 11 6(b) Case 12

Figure 5-6 - SEM micrographs of spray pyrolysis deposition of ZnO+In_2O_3 on Al_2O_3 substrate: (a) 0.25ZnO+0.75In_2O_3 at T= 400° C and C=0.1 mol/lit; and (b) 0.8ZnO+0.2In_2O_3 at T= 400° C and C=0.1 mol/lit.

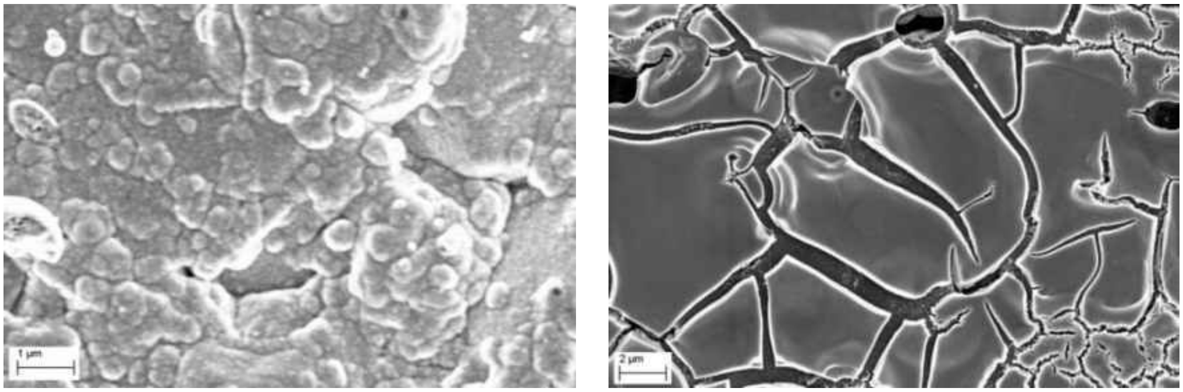

7(a) Case 13 7(b) Case 14

Figure 5-7 - SEM micrographs of spray pyrolysis deposition of SnO_2+In_2O_3 on Al_2O_3 substrate: (a) 0.80SnO_2+0.20In_2O_3 at T= 450° C and C=0.25 mol/lit; and (b) 0.95SnO_2+0.05In_2O_3 at T= 450° C and C=0.25 mol/lit.

5.3.2.1 Size distribution

Image processing techniques were applied to the SEM micrographs in order to calculate the particle size distribution, specifically the mean diameter of each particle. The average particle size was determined by considering all particle dimensions in the film. The mean area of particles ($\bar{A}$) was calculated by considering the total number of particles and the space intervals thus [28]:

$$\bar{A} = A + \left(\sum fd/N\right) i \tag{5-1}$$

where $\bar{A}$ is actual mean area, A is the assumed mean area, i is the class interval between particles, d is the deviation of midpoint from assumed mean, and N is total number of particles considered. The mean diameter was then obtained from $\bar{A}$ assuming spherical particles.

Table 5-2 shows the average particle size and standard deviation from average particle size obtained for some of the films produced. The standard deviation values show the dispersion of particle sizes from the measured average particle size for each case. Smaller values of standard deviations indicate narrower range of particle size distribution from average value. It implies simultaneous chemical reactions inside droplets and subsequently a homogenous particle growth on the substrate due to the balance between the substrate temperature and the concentrations of precursors in solution. Figures 5-8 and 5-9 show the particle size distributions obtained for ZnO single oxide and ZnO+In_2O_3 mixed oxide films respectively.

Table 5-2 - Particle size of synthesized ZnO and ZnO+In_2O_3 films.

Case	**Deposited Metal Oxide**	**Temperature (° C)**	**Concentration (mol/lit)**	**Ave. Particle Size (*nm*)**	**Standard Deviation SD (*nm*)**
1	ZnO	400	0.1	112	65
3	ZnO	400	0.2	119	70
4	ZnO	400	0.3	233	89
10	SnO_2	450	0.5	47	41
11	25wt.% ZnO+75wt.% In_2O_3	400	0.1	136	94
12	80wt.% ZnO+20wt.% In_2O_3	400	0.1	201	123
13	80wt.%SnO_2+20wt.% In_2O_3	450	0.25	94	46

Figure 5-8 shows that by increasing the concentration of ZnO, the particles grow larger. At low concentration, the particles are smaller and the size distribution is less homogenous (Table 5-2, Case 1) as was also observed in a previous study [21]. At C=0.3 mol/lit and T=400 °C (Table 5-2, Case 4), a narrow particle size distribution is observed with high probability of a more homogenous film. Comparing the standard deviation values of cases 1 to 3 approves that more particles within 1 SD is observed when solution concentration is high and subsequently the homogeneity of particle size is higher.

Figure 5-9 for $ZnO+In_2O_3$ mixed oxide shows that the addition of indium oxide component to ZnO results in the growth of particles over a wider range of sizes. Higher standard variation values represents that there is more deviation from average size when a mixed precursor is deposited on the surface. It means that the particles in mixed oxides cases are produced with less homogeneity compared to the single oxides (ZnO) of Fig. 5-8. In the mixed oxide film cases of Fig. 5-9, the results show that a more homogenous particle distribution is obtained when ZnO is the dominant precursor. The experimental results show that by increasing the amount of ZnO, crystallization occurs and a well-structured thin film is produced. There is therefore a better chance to produce zinc oxide crystals or rods at the higher ZnO concentration [20]. Thus the overall particle size is reduced when the concentration of indium is increased (Table 5-2, Case 11). This trend may be attributed to the fact that indium ions limit the growth of ZnO particles on the surface [24] or by the increased stresses applied by the mixture which limits the growth of grain size [27].

Figure 5-10 shows the particle size distribution for SnO_2 single oxide and $SnO_2+In_2O_3$ mixed oxide films. The single oxide is deposited in the shape of spherical grains with sharp boundaries as indicated in the previous Fig. 5-3(d). The mixed metal oxide is formed with rough structure with larger spherical grains as shown in the previous Fig. 5-7(a). The results show that in the latter case, the particles agglomerate and form larger-sized particles as depicted in Fig. 5-10 (Table 5-2, Cases 10 and 13).

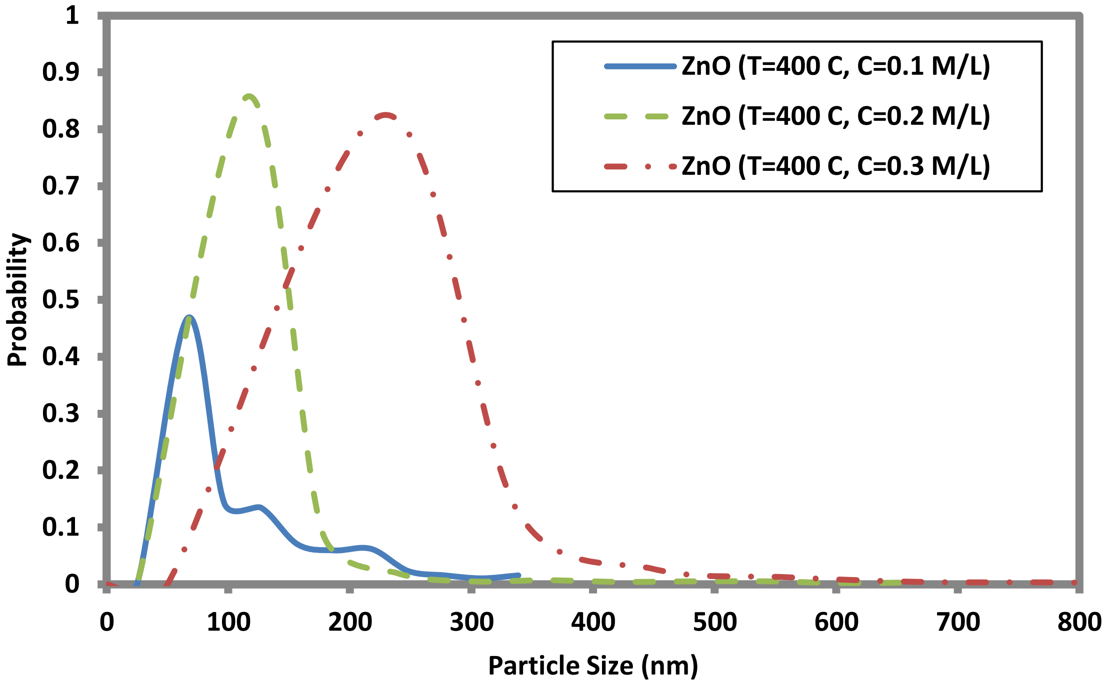

Figure 5-8 - Particle size distribution of ZnO single oxide thin films.

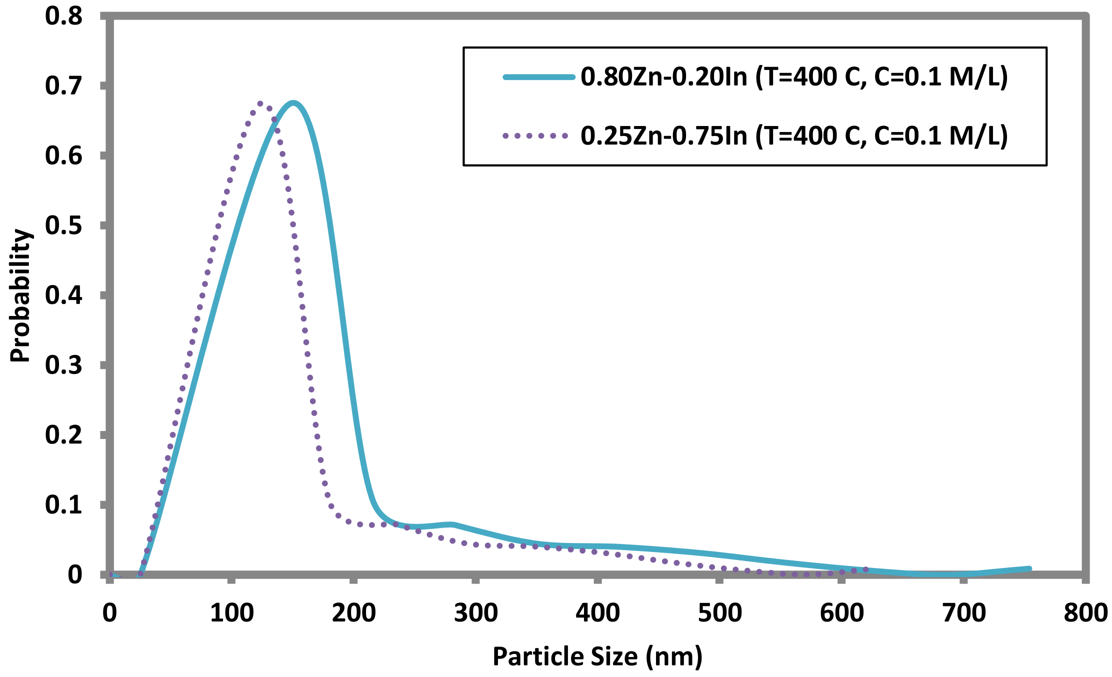

Figure 5-9 - Particle size distribution of (x wt. % ZnO + y wt. % In_2O_3) mixed oxide thin films.

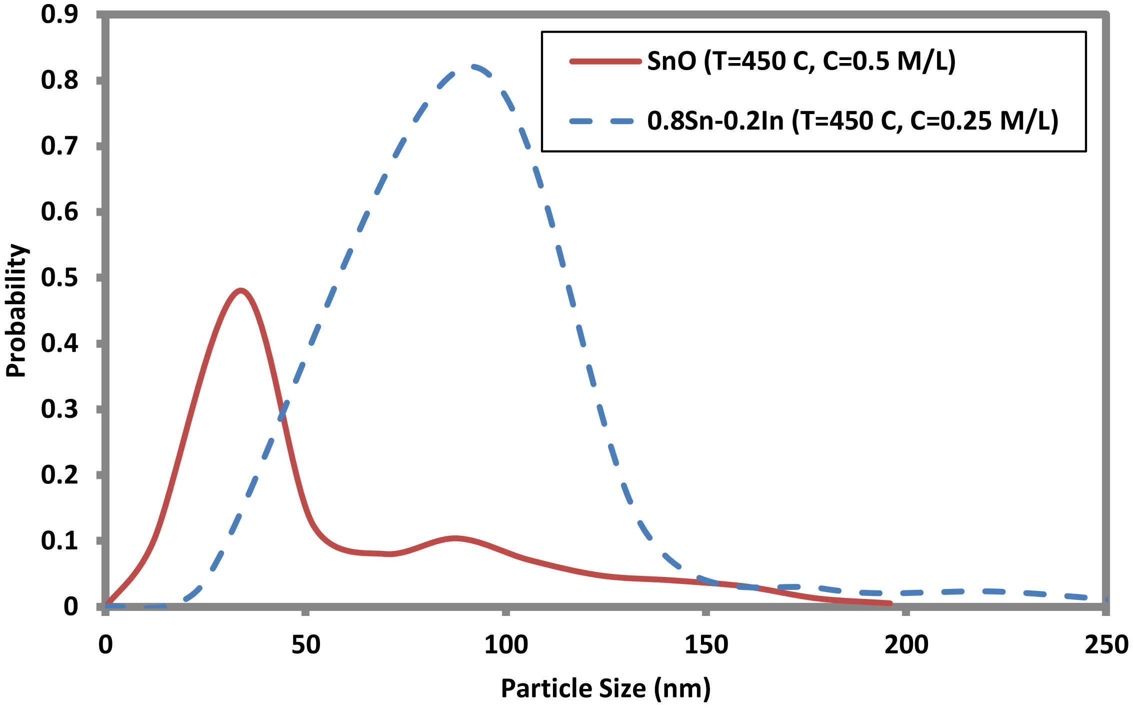

Figure 5-10 - Particle size distribution of SnO_2 single oxide and 80 wt. % SnO_2 + 20 wt. % In_2O_3 mixed oxide thin films.

5.4 Discussion on Sensor Properties

The previous Fig. 5-2 indicated the effect of temperature and concentration on morphology of ZnO films. The results showed that a further increase in temperature to 450 °C increases the film uniformity, but reduces its specific surface area which can adversely affect the sensor response of the film. The results also showed that the grain size of the ZnO film increases with increase in the amount of precursor dissolved in solution.

Thus, there are interparticle contacts of two types in the synthesized films: contacts between crystallites inside crystalline aggregates and contacts between aggregates. The contacts between aggregates of crystallites largely determine the conductivity of the nanocrystalline film [29].

Our study of $ZnO+In_2O_3$ composite oxide films has demonstrated that the morphology of the films depends strongly on the composition. The previous Fig. 5-6 presented the photomicrographs of the composite films with various ZnO to In_2O_3 ratios. The composite film $0.25ZnO+0.75In_2O_3$ (Fig. 5-6(a)) consists of elongated particles of arbitrary shape, which are aggregates that combine small crystallites of In_2O_3 and ZnO. The composite $0.8ZnO+0.2In_2O_3$ (Fig. 5-6(b)) contains for the most part faceted particles that are large individual ZnO crystals (or splices of such crystals). In this composite, such particles of ZnO are mixed with the In_2O_3 particles, which other studies [30] have shown to also increase the sensory response by about 15-20% compared to the response of pure ZnO, i.e. considerably less than in the composite of Fig. 5-6(a).

5.5 Conclusion

In this chapter, the processing of single oxide and mixed oxide films by spray pyrolysis technique (SPT) was investigated. Two single oxides (ZnO and SnO_2) and two mixed oxides ($ZnO+In_2O_3$ and $SnO_2+In_2O_3$) were considered. The films were processed under varying substrate temperature conditions and different precursor solution concentrations, and deposited on heated Al_2O_3 substrates. The films were then characterized by SEM for microstructure and XPS for composition.

The study also considered the dependence of the morphology of the films on the synthesis conditions. It has been shown that increasing the deposition temperature in the range 350 to 450°C results in the formation of films with more uniform particle sizes and the size of deposited particles increases with increasing concentration of precursor solution from 0.1 to 0.3 mol/liter.

The particles of the film are not separate crystallites, but splices or aggregates of crystallites. The interaction between crystallites inside crystalline aggregates is stronger that the interaction between aggregates. The conductivity of the film is determined by the electron density in an aggregate and the contacts between aggregates.

5.6 List of References

1. Khatami, S. M. N., Ilegbusi O. J. (January 2011). Modeling of Aerosol Spray Characteristics for Synthesis of Mixed-Oxide Nanocomposite Sensor Film, In: *ASME 2011 International Mechanical Engineering Congress and Exposition* (pp. 581-589). American Society of Mechanical Engineers.
2. Khatami, S. M. N., & Ilegbusi, O. J. (2012, November). Droplet Evaporation and Chemical Reaction in a Single Multi-Component Droplet to Synthesis Mixed-Oxide Film Using Spray Pyrolysis Method. In *ASME 2012 International Mechanical Engineering Congress and Exposition* (pp. 633-638). American Society of Mechanical Engineers.
3. Hdz-Garcia, H. M., & Martinez, A. I. (2010, January). Formation of metal oxides thin films: a thermodynamic analysis. In *Proceedings of the 4th WSEAS international conference on Circuits, systems, signal and telecommunications Cambridge, USA Pages* (pp. 144-146).
4. Korotchenkov, G., Brynzari, V., & Dmitriev, S. (1999). SnO_2 films for thin film gas sensor design. *Materials Science and Engineering: B*, *63*(3), 195-204.
5. Khatami, S. M. N., Kuruppumullage, D. N., Ilegbusi, O.J. (November 2013). Characterization of Metal Oxide Sensor Thin Films Deposited by Spray Pyrolysis, In: *ASME 2013 International Mechanical Engineering Congress and Exposition* (pp. V010T11A044-V010T11A044). American Society of Mechanical Engineers.
6. Khatami, S. M. N., Ilegbusi, O. J., & Trakhtenberg, L. (2013). Modeling of aerosol spray characteristics for synthesis of sensor thin film from solution. *Applied Mathematical Modelling*, *37*(9), 6389-6399.

7. Vigil, O., Cruz, F., Santana, G., Vaillant, L., Morales-Acevedo, A., & Contreras-Puente, G. (2000). Influence of post-thermal annealing on the properties of sprayed cadmium–zinc oxide thin films. *Applied surface science*, *161*(1), 27-34.
8. Patil, G. E., Kajale, D. D., Gaikwad, V. B., & Jain, G. H. (2012). Spray pyrolysis deposition of nanostructured tin oxide thin films. *International Scholarly Research Notices*, *2012*.
9. Ramireddy, T. R., Venugopal, V., Bellam, J. B., Maldonado, A., Vega-Pérez, J., Velumani, S., & Olvera, M. D. L. L. (2012). Effect of the Milling Time of the Precursors on the Physical Properties of Sprayed Aluminum-Doped Zinc Oxide (ZnO: Al) Thin Films. *Materials*, *5*(8), 1404-1412.
10. Zaier, A., Lakfif, F., Kabir, A., Boudjadar, S., & Aida, M. S. (2009). Effects of the substrate temperature and solution molarity on the structural opto-electric properties of ZnO thin films deposited by spray pyrolysis. *Materials Science in Semiconductor Processing*, *12*(6), 207-211.
11. Korotcenkov, G., Brinzari, V., Schwank, J., DiBattista, M., & Vasiliev, A. (2001). Peculiarities of SnO_2 thin film deposition by spray pyrolysis for gas sensor application. *Sensors and Actuators B: Chemical*, *77*(1), 244-252.
12. Bagheri-Mohagheghi, M. M., & Shokooh-Saremi, M. (2004). Electrical, optical and structural properties of Li-doped SnO_2 transparent conducting films deposited by the spray pyrolysis technique: a carrier-type conversion study. *Semiconductor science and technology*, *19*(6), 764.
13. Hu, J., & Gordon, R. G. (1992a). Atmospheric pressure chemical vapor deposition of gallium doped zinc oxide thin films from diethyl zinc, water, and triethyl gallium. *Journal of Applied Physics*, *72*(11), 5381-5392.
14. Hu, J., & Gordon, R. G. (1992b). Textured aluminum-doped zinc oxide thin films from atmospheric pressure chemical-vapor deposition. *Journal of Applied Physics*, *71*(2), 880-890.
15. Zunke, I., Heft, A., Schäfer, P., Haidu, F., Lehmann, D., Grünler, B., ... & Zahn, D. R. T. (2013). Conductive zinc oxide thin film coatings by combustion chemical vapour deposition at atmospheric pressure. *Thin Solid Films*, *532*, 50-55.

16. Ayouchi, R., Martin, F., Leinen, D., & Ramos-Barrado, J. R. (2003). Growth of pure ZnO thin films prepared by chemical spray pyrolysis on silicon. Journal of crystal growth, 247(3), 497-504.
17. Ghimbeu, C. M., Van Landschoot, R. C., Schoonman, J., & Lumbreras, M. (2007). Preparation and characterization of SnO_2 and Cu-doped SnO_2 thin films using electrostatic spray deposition (ESD). *Journal of the European Ceramic Society*, *27*(1), 207-213.
18. Chen, Z., Salagaj, T., Jensen, C., Strobl, K., Nakarmi, M., & Shum, K. (2009, January). ZnO thin film deposition on sapphire substrates by chemical vapor deposition. In *MRS Proceedings* (Vol. 1167, pp. 1167-O07). Cambridge University Press.
19. Jiao, B. C., Zhang, X. D., Wei, C. C., Sun, J., Huang, Q., & Zhao, Y. (2011). Effect of acetic acid on ZnO: In transparent conductive oxide prepared by ultrasonic spray pyrolysis. *Thin Solid Films*, *520*(4), 1323-1329.
20. Liang, Z., Gao, R., Lan, J. L., Wiranwetchayan, O., Zhang, Q., Li, C., & Cao, G. (2013). Growth of vertically aligned ZnO nanowalls for inverted polymer solar cells. *Solar Energy Materials and Solar Cells*, *117*, 34-40.
21. Tucic, A., Marinkovic, Z. V., Mancic, L., Cilense, M., & Miloševic, O. (2003). Pyrosol preparation and structural characterization of SnO_2 thin films. *Journal of materials processing technology*, *143*, 41-45.
22. Patil, P. S., Kawar, R. K., Sadale, S. B., & Chigare, P. S. (2003). Properties of spray deposited tin oxide thin films derived from tri-n-butyltin acetate. *Thin Solid Films*, *437*(1), 34-44.
23. Smith, A. (2000). Pyrosol deposition of ZnO and SnO_2 based thin films: the interplay between solution chemistry, growth rate and film morphology. *Thin Solid Films*, *376*(1), 47-55.
24. Badadhe, S. S., & Mulla, I. S. (2009). H_2S gas sensitive indium-doped ZnO thin films: Preparation and characterization. Sensors and Actuators B: Chemical, 143(1), 164-170.
25. Miki-Yoshida, M., Paraguay-Delgado, F., Estrada-Lopez, W., & Andrade, E. (2000). Structure and morphology of high quality indium-doped ZnO films obtained by spray pyrolysis. *Thin Solid Films*, *376*(1), 99-109.

26. Sivalingam, D., Gopalakrishnan, J. B., & Rayappan, J. B. B. (2012). Nanostructured mixed ZnO and CdO thin film for selective ethanol sensing. *Materials Letters*, *77*, 117-120.
27. Lee, J. H., Lee, S. Y., & Park, B. O. (2006). Fabrication and characteristics of transparent conducting In_2O_3–ZnO thin films by ultrasonic spray pyrolysis. *Materials Science and Engineering: B*, *127*(2), 267-271.
28. Gupta, S. P. (1985). Measures of dispersion. Statistical Methods. New Delhi: Sultan Chand and Sons.
29. Korotcenkov, G., Brinzari, V., & Boris, I. (2008). (Cu, Fe, Co, or Ni)-doped tin dioxide films deposited by spray pyrolysis: doping influence on film morphology. *Journal of Materials Science*, *43*(8), 2761-2770.
30. Trakhtenberg, L. I., Gerasimov, G. N., Gromov, V. F., Belysheva, T. V., & Ilegbusi, O. J. (2012). Effect of composition on sensing properties of SnO_2 + In_2O_3 mixed nanostructured films. *Sensors and Actuators B: Chemical*, *169*, 32-38.

CHAPTER 6: MATHEMATICAL MODELING AND EXPERIMENTAL VALIDATION OF FILM GROWTH

6.1 Overview

In this chapter, the deposition of metal oxide films using SPT is investigated through mathematical and physical modeling. A comprehensive model is developed of the processes including atomization, spray, evaporation, chemical reaction and deposition. The predicted results including particle size and film thickness are compared with the experimental data obtained in the previous chapter. The predicted film thickness is in good agreement with the measurements when the temperature is high enough to for the chemical reaction to proceed. The model also adequately predicts the size distribution when the nanocrystals are well-structured at controlled temperature and concentration.

6.2 Problem Considered

A comprehensive mathematical model of the SPT process can be considered in two broad categories. The first involves the atomization process and the second involves collectively the evaporation, chemical reaction and the film growth processes. The parameters associated with each process are listed in Table 6-1.

Table 6-1 - Spray pyrolysis process models.

Model	**Type**	**Input**	**Output**
Spray	*CFD Model*	T_s (Substrate Temperature) V_i (Initial droplet velocity)	P (Pressure) T (Temperature) m_i (Initial Droplet mass) d_d (Initial Droplet diameter)
Evaporation	*Math Model*	P (Pressure) T (Temperature) m_i (Initial droplet mass) d_d (Initial droplet diameter)	m_f (Final droplet mass)
Decomposition/ Reaction	*Math Model*	T (Temperature) C (Initial concentration of precursor) derived from m_f	$x_{R,f}$ (Final fraction of precursor reacted) d_f (Final droplet diameter)
Deposition/ Growth	*Math Model*	D_i (Initial film thickness) derived from d_f	D_f (Final film thickness)

The major parameters associated with each process are shown in Fig. 6-1. First, a spray model is developed to predict droplet diameter before reaching the substrate (d_d). The details of the spray model have been presented in previous chapter 3. This CFD model also is used to determine the pressure and temperature distribution within the domain. The initial droplet mass (m_i) can be calculated from the droplet diameter and used in the subsequent evaporation model.

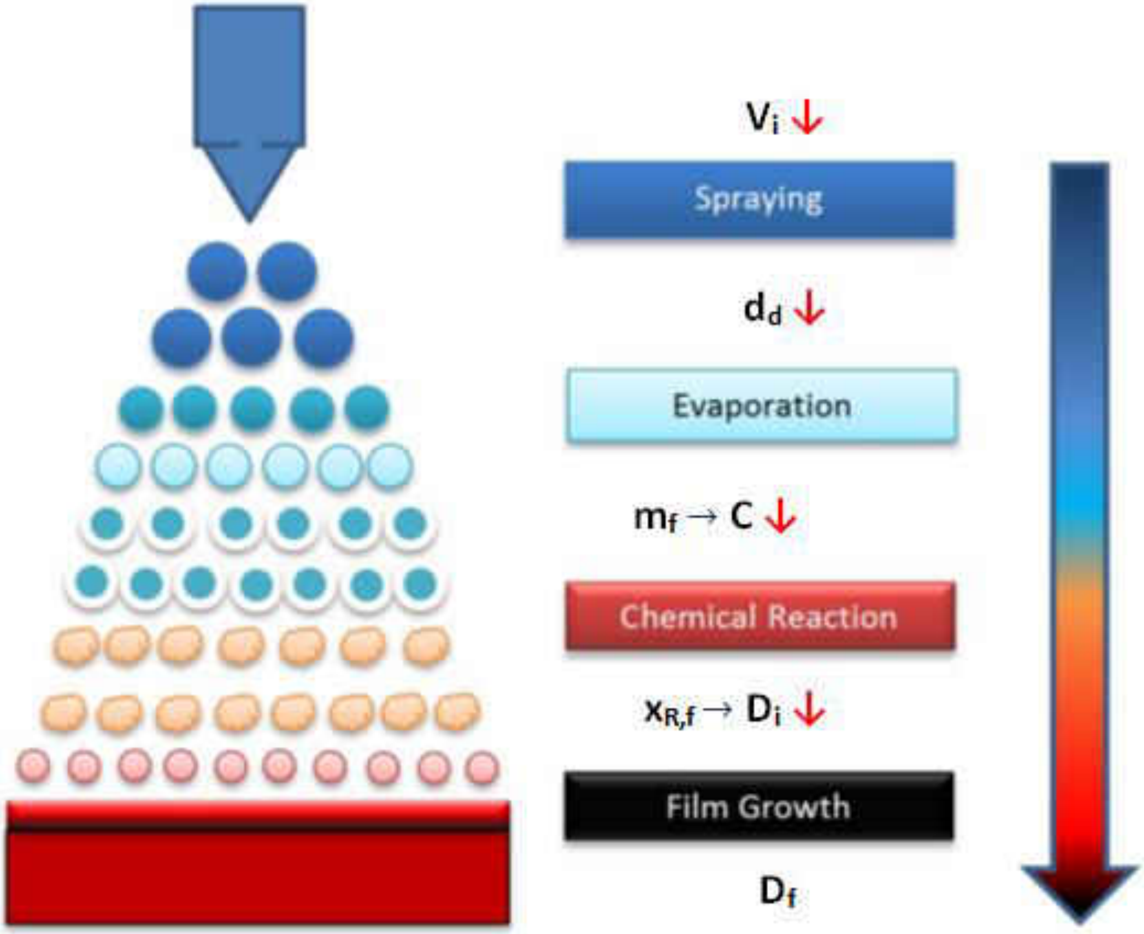

Figure 6-1 - Schematic view of spray pyrolysis stages.

6.3 Formulation

6.3.1 *Evaporation*

The solvent evaporation rate is determined by the decreasing droplet mass (m) and can be formulated as:

$$\frac{dm}{dt} = \frac{2\pi d_d D_v M}{N_A}.(n_g - n_{sat}).\varphi \qquad (6\text{-}1)$$

where D_v is the diffusion coefficient of solvent vapor in air, N_A is Avogadro's constant (6.0221413×10^{23} 1/mole), M is the molecular weight of water, and n_g and n_{sat} are the vapor concentrations at the droplet surface and in the surrounding air, respectively [1]. Initial mass (m_i) is determined from CFD modeling of spray for a droplet at the substrate. This value considers the mass of water inside the droplet. In the specific experiment considered for validation, the precursor comprised 1% $ZnCl_2$ (for ZnO single oxide) and 5% $ZnCl_2$ + 95% $In(NO_3)_3$ (for ZnO+In_2O_3 mixed oxide) of the total mass of droplet. Therefore, the mass of precursor can be neglected in consideration of the total mass at this stage. The parameter φ in Eq. (6-1) is the Knudsen correction which allows for the effect of transport when the size of droplet is on the order of the mean free path of molecules in air (λ~68 *nm*):

$$\varphi = \frac{2\lambda+d_d}{d_d+5.33\left(\frac{\lambda^2}{d_d}\right)+3.42\lambda} \tag{6-2}$$

where d_d is the droplet diameter.

The vapor concentration can be calculated as:

$$n_g = \frac{x_w P_g}{k_B T_{sat}} \tag{6-3}$$

$$n_{sat} = \frac{x_w P_{sat}}{k_B T_{sat}} \tag{6-4}$$

where P is the pressure and x_w is the mole fraction of solvent (water). The parameter D_v can be defined as [1]:

$$D_v = \frac{1.13*10^{-5}.T^{2.159}}{P} \tag{6-5}$$

Since D_v, n_g and n_{sat} are dependent on surrounding air pressure (P) and temperature (T), the temperature and pressure are determined by CFD modeling of spray using the FLUENT software package which was developed in previous chapter 3. The substrate temperature is fixed at 400° C as a reference.

By solving Eq. (6-1) in MATLAB, the final mass (m_f) inside the droplet can be determined. This value can be used to calculate the initial droplet diameter (d_i) and the concentration of initial precursor (C) for the next stage.

6.3.2 Decomposition/Reaction

The pyrolysis of the precipitate starts before the precipitate reaches the substrate and nucleation and growth of thin films on the substrate occurs later. Subsequently, a continuous thin layer of metal oxide is synthesized by the growth of the nuclei. The desired condition is for the droplet to approach the substrate when the solvent has been largely removed [2].

A chemical reaction (thermal decomposition) occurs during spray pyrolysis in addition to the physical processes of evaporation and drying [1]. The chemical reaction for the system considered was previously formulated in chapter 4 (Eqs. (4-1), (4-2), and (4-3))

The general kinetic equation can be described as [1]:

$$\frac{d_{x_R}}{dt} = Ae^{(-E_a/RT)}.f(x_R) \tag{6-6}$$

where $\frac{d_{x_R}}{dt}$ is the reaction rate, R is gas constant (8.3144621 J/mol.K), x is the fraction of precursor reacted [$ZnCl_2$ and/or $In(NO_3)_3$], and $f(x_R)$ is the function of fraction reacted which depends on the mechanism of the decomposition reaction. This function represents the theoretical kinetic equation of the decomposition mechanism and it can be defined by normal grain growth model: $f(x_R) = (1 - x_R)^n$ where n=1.25 is a function of reaction order [1]. In Eq. (6-6), A is the pre-exponential factor and E_a is the activation energy which can be determined from the Arrhenius kinetic reaction equation. By solving the differential Eq. (6-6), the final x_R ($x_{R,f}$) can be found which is the fraction of the precursor reacted at the final stage.

The final diameter after chemical reaction is derived from the one-droplet to one-particle principle in spray pyrolysis [1] thus:

$$d_f = d_d \left(\frac{C.M_p}{\rho_p}\right)^{1/3} \tag{6-7}$$

where d_f is the final particle diameter, d_i is initial droplet diameter, C is concentration of initial precursor, M_p is molecular weight of the generated particle, and ρ_p is the density of the generated particle (ZnO in single oxide and ZnO+In_2O_3 in mixed oxide). Since only a fraction of precursor is involved in the chemical reaction at this stage, the final droplet diameter needs to be modified accordingly. Therefore, the final droplet size is corrected using the $x_{R,f}$ factor. In effect, when $x_{R,f}$ =1, the final d_f is equal to the calculated diameter, and when $x_{R,f}$ =0, there is no particle created and d_f=0.

6.3.3 Deposition/Growth

The growth rate in a spray deposition process is linearly dependent on spray time and logarithmically dependent on substrate temperature [3]. This rate can be represented as:

$$\frac{dD}{dt} = A_1.e^{(-E/k_B T)} \tag{6-8}$$

where D is the film thickness, A_1 is the growth rate coefficient, T is temperature, t is time and k_B is the Boltzmann constant (=1.3806488×10^{-23} m^2.kg/s^2.K). Based on the experimental results, the following parameters were used to solve Eq. (6-8): A_1 = 3.1 µm, t =30 s, T =400° C, E = 0.427eV. Since the amount of indium nitrate in the mixture is less than 20%, the same growth rate coefficient can be used for the mixed oxide cases.

The initial film thickness (D_i) is derived from the reaction stage. Specifically, the final droplet diameter (d_f) at that stage is assumed to be the same as the initial film thickness, assuming a spherical particle shape. The final film thickness (D_f) is predicted subsequently by solving Eq. (6-8). It should be remarked that since the precursor solution used for the spray is typically dilute, the above model is expected to be valid for both single and mixed oxides.

An experimental study was conducted to validate the modeling results. The details about the experiment were presented in the previous chapter 5, section 5.2. In the experiment, the optimum processing conditions are strongly dependent on the composition of the precursor solution. The deposited single and mixed oxide thin films are subsequently characterized by Scanning Electron Microscopy (SEM) for the particle size and film thickness. SEM combines high spatial resolution with a wide field of view to improve accuracy [4]. The calculation of particle size distribution from SEM micrographs was explained in previous Section 5.3.2.1 [5]. Table 6-2 summarizes the input data used for the experiments to validate the results.

Table 6-2 - Experimental parameters used for deposition of ZnO and ZnO+In_2O_3 films.

Deposited Metal Oxide	**Concentration C (mol/lit)**	**Temperature T_s (° C)**
ZnO	0.1	350
ZnO	0.1	400
ZnO	0.2	400
ZnO	0.3	400
25 wt. % ZnO+75 wt. % In_2O_3	0.1	400
80 wt. % ZnO+20 wt. % In_2O_3	0.1	400

6.4 Results

6.4.1 Film Thickness

Figure 6-2 shows the predicted variation of ZnO film thickness with deposition duration. The film initially grows rapidly and after a certain duration (~10s), becomes gradual. The result illustrates the role of mass diffusion in the growth of crystalline structures. This observed trend may be attributed to space limitation on the substrate surface and pressure from adjacent growing particles which subsequently limit the growth rate. At long time duration, the growth rate is limited by diffusion at a constant level in the consensus of previous studies [6].

Figure 6-3 shows the predicted variation of ZnO film thickness with substrate temperature. Increasing the substrate temperature enhances the growth of particles on the surface. This trend is consistent with the direct influence of temperature on both diffusion and chemical reaction. It should be noted that the threshold deposition time of 10s of previous Fig. 6-2 which produced a film thickness of 272 *nm* corresponds to a temperature of 400 °C in Fig. 6-3.

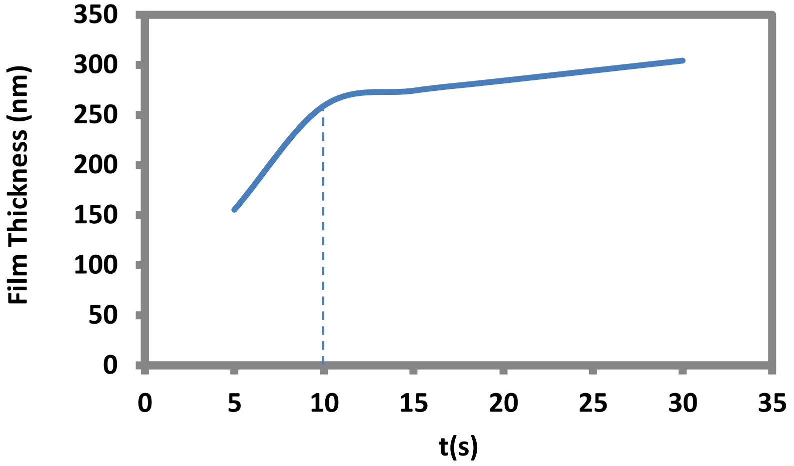

Figure 6-2 - Predicted variation of ZnO film thickness with deposition time (T=400 °C, C=0.2 mol/lit).

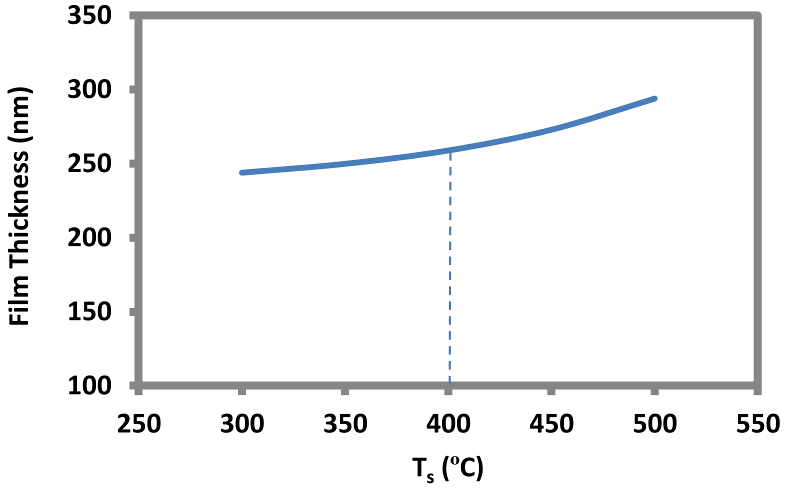

Figure 6-3 - Predicted variation of ZnO film thickness with substrate temperature (T=400 °C, C=0.2 mol/lit).

Table 6-3 compares the film thickness of ZnO films obtained from modeling and experiments at two substrate temperatures. The experiment was performed with deposition duration of 10s which is the threshold deposition time obtained from the model (Fig. 6-2). The model predicts the film thickness on the same order as the experiment and the accuracy is quite good (<3% error) at the higher temperature of 400 °C. The improved model accuracy at higher temperature is attributed to the heat loss in the experiment which impedes film growth. Some of the heat loss is compensated at the higher temperatures. These results are also consistent with Figs. 6-2 and 6-3. Thus the proposed model has the potential to successfully predict the optimum processing parameters for the film synthesis.

Table 6-3 - Predicted and measured thickness of ZnO films.

Temperature T_s (° C)	**Concentration C (mol/lit)**	**Time t (s)**	**Measured Film Thickness (*nm*)**	**Predicted Film Thickness (*nm*)**
350	0.1	10	112	169
400	0.2	10	233	214

6.4.2 Particle Size

The previous Figs. 5-2 (a) through 5-2(d) in chapter 5 showed the SEM micrographs of single ZnO oxides processed at defined temperature and different concentrations. The result indicated that at low concentration (C= 0.1 mol/lit) (Fig. 5-2(a)), small spherical crystallites are formed that agglomerate at the surface in the shape of powder. The average particle size is 112 *nm* which is in the consensus of previous studies [7-9].

The properties of particles change by increasing the concentration. The grain size increases with increase in the amount of precursor dissolved in solution in Fig. 5-2(c) as was also observed in previous studies [10-11]. The film is mostly homogenous with average nanoparticle size of about 119 *nm*. The particles exhibit hexagonal flake morphology similar to a previous study [12]. Upon further increase in concentration (C= 0.3 mol/lit), the density and size of particles are increased to an average size of 233 *nm*. In this case, the crystals are plate-like and the sides of the walls are grown packed together (Fig. 5-2(d)). A similar hexagonal wurtzie structure has also been observed at high concentration [13].

The previous Figs. 5-6(a) and 5-6(b) show the SEM micrographs of ZnO+In_2O_3 mixed oxide thin films on Al_2O_3 substrate at T= 400° C composed of 25% of ZnO mixed with 75% of In_2O_3 (Fig. 5-6(a)), and 80% of ZnO mixed with 20% of In_2O_3 (Fig. 5-6(b)). At lower composition ratio of ZnO (Fig. 5-6(a)), the growth of particle side walls results in the formation of nano tubes [10, 14]. By increasing the amount of zinc (Fig. 5-6(b)), crystallization is enhanced and a well-structured thin film is synthesized. In this case, there is a better chance to produce ZnO crystals or rods [10]. This result confirms that the overall particle size is increased when the concentration of In_2O_3 is decreased. The observed trend may be attributed to the fact that indium ions limit the growth of ZnO particles on the surface. The grain size has been observed to decrease by increasing the indium doping [15]. This is attributed to the stresses applied by the mixture which limits the growth of grain size.

The results show that addition of In_2O_3 component to ZnO results in the growth of particles over a wider size range as was also observed in a previous study [16]. Thus the particles are deposited with less homogeneity compared to the single oxide ZnO. A comparison of Figs. 5-6(a) and 5-6(b) also shows that the film is more homogenous when ZnO is the dominant precursor. At low concentration of ZnO, the structure of the mixed oxide is similar to that obtained for single oxide ZnO in Fig 5-2(d). However the average particle size obtained (~136 *nm*) is less than the single oxide. The value predicted from the mathematical model for the mixed oxide of Fig. 5-6(a) is 209 *nm* which is lower than the corresponding value for ZnO deposition. This value is however still in the range of the measured particle size. The predicted particle size is 244 *nm* at the higher concentration of ZnO (Fig. 5-6(b)). Table 6-4 summarizes the values of the average particle sizes obtained from modeling and experiments. The results show that the predicted particle size values are within 1 SD at high solution concentration while the predicted particle size values are within 2 SD when the concentration of zinc precursor in solution is lower than 0.2 mol/lit. These results imply that the predictions from the mathematical model are more reliable at higher concentrations of precursor solutions, which correspond to enhanced crystallization and well-structured thin films. The dependency of particle size on concentration is also expressed in Eq. (6-7) of mathematical model. At higher concentrations, the sufficient amount of precursors in solution promotes the chemical reaction and enhances the growth of particles from initial droplets. Therefore, the experimental result and mathematical model show better agreement on determination of final particle size. Similar statistical results indicate that the predicted values are within the standard deviation in the mixed metal oxide cases.

Table 6-4 - Predicted and measured particle size for single and mixed oxides.

Deposited Oxide	**Temperature T_s (° C)**	**Concentration C (mol/lit)**	**Measured Particle Size (*nm*)**	**Standard Deviation SD (*nm*)**	**Predicted Particle Size (*nm*)**
ZnO	400	0.1	112	66	189
ZnO	400	0.2	119	70	234
ZnO	400	0.3	233	89	265
25wt.%ZnO+75wt.% In_2O_3	400	0.1	136	94	209
80wt.%ZnO+20wt.% In_2O_3	400	0.1	201	123	244

The agreement between the experimental measurements and modeling is generally acceptable and the results are on the same order of magnitude. The agreement is particularly good when the deposited film is completely well-structured and the crystal shapes are fully formed as in cases 3 and 5 for which the maximum error is less than 14% in case 3.

6.5 Conclusion

A comprehensive mathematical model has been developed to simulate film deposition by Spray Pyrolysis Technique (SPT). The mechanism underlying film growth by SPT was systematically investigated, enabling identification of important processes for development of a comprehensive model. Thus, the model was divided into four sub-models: Atomization, Evaporation, Decomposition and Growth based on the underlying physical and chemical mechanisms. The model developed is applicable to the growth of both single oxide (ZnO) and mixed oxide ($ZnO+In_2O_3$). The predicted results (particle size and film thickness) were validated by comparison with the experimental data obtained in previous chapter.

6.6 List of References

1. Widiyastuti, W., Wang, W. N., Lenggoro, I. W., Iskandar, F., & Okuyama, K. (2007). Simulation and experimental study of spray pyrolysis of polydispersed droplets. *Journal of Materials Research*, *22*(07), 1888-1898.
2. Shinde, P. S. (2012). Photoelectrochemical Detoxification of water using spray deposited oxide semiconductor thin films.
3. Filipovic, L., Selberherr, S., Mutinati, G. C., Brunet, E., Steinhauer, S., Köck, A., ... & Schrank, F. (2013). Modeling spray pyrolysis deposition. In *Proceedings of the World Congress on Engineering* (Vol. 2, pp. 987-992).
4. Kowarik S., Hinderhofer A., Gerlach A., & F. Schreiber (2011). Modelling thin film deposition processes based on real-time observation. Book chapter in “Thin film growth” edited by Z. Cao, Oxford, Cambridge, Woodhead Publishing.

5. Gupta, S. P. (1985). Measures of dispersion. Statistical Methods. New Delhi: Sultan Chand and Sons.
6. Ayouchi, R., Martin, F., Leinen, D., & Ramos-Barrado, J. R. (2003). Growth of pure ZnO thin films prepared by chemical spray pyrolysis on silicon. *Journal of crystal growth*, *247*(3), 497-504.
7. Hu, J., & Gordon, R. G. (1992a). Atmospheric pressure chemical vapor deposition of gallium doped zinc oxide thin films from diethyl zinc, water, and triethyl gallium. *Journal of Applied Physics*, *72*(11), 5381-5392.
8. Hu, J., & Gordon, R. G. (1992b). Textured aluminum-doped zinc oxide thin films from atmospheric pressure chemical- vapor deposition. *Journal of Applied Physics*, *71*(2), 880-890.
9. Zunke, I., Heft, A., Schäfer, P., Haidu, F., Lehmann, D., Grünler, B., ... & Zahn, D. R. T. (2013). Conductive zinc oxide thin film coatings by combustion chemical vapour deposition at atmospheric pressure. Thin Solid Films, 532, 50-55.
10. Liang, Z., Gao, R., Lan, J. L., Wiranwetchayan, O., Zhang, Q., Li, C., & Cao, G. (2013). Growth of vertically aligned ZnO nanowalls for inverted polymer solar cells. *Solar Energy Materials and Solar Cells*, *117*, 34-40.
11. Tucic, A., Marinkovic, Z. V., Mancic, L., Cilense, M., & Miloševic, O. (2003). Pyrosol preparation and structural characterization of SnO_2 thin films. *Journal of materials processing technology*, *143*, 41-45.
12. Jiao, B. C., Zhang, X. D., Wei, C. C., Sun, J., Huang, Q., & Zhao, Y. (2011). Effect of acetic acid on ZnO: In transparent conductive oxide prepared by ultrasonic spray pyrolysis. *Thin Solid Films*, *520*(4), 1323-1329.
13. Sivalingam, D., Gopalakrishnan, J. B., & Rayappan, J. B. B. (2012). Nanostructured mixed ZnO and CdO thin film for selective ethanol sensing. *Materials Letters*, *77*, 117-120.
14. Miki-Yoshida, M., Paraguay-Delgado, F., Estrada-Lopez, W., & Andrade, E. (2000). Structure and morphology of high quality indium-doped ZnO films obtained by spray pyrolysis. *Thin Solid Films*, *376*(1), 99-109.

15. Lee, J. H., Lee, S. Y., & Park, B. O. (2006). Fabrication and characteristics of transparent conducting In_2O_3–ZnO thin films by ultrasonic spray pyrolysis. Materials Science and Engineering: B, 127(2), 267-271.
16. Badadhe, S. S., & Mulla, I. S. (2009). H_2S gas sensitive indium-doped ZnO thin films: Preparation and characterization. Sensors and Actuators B: Chemical, 143(1), 164-170.

CHAPTER 7: CONCLUSIONS AND RECOMMENDATIONS

7.1 Summary of Chapters

The research involves experimental and mathematical investigation of aerosol synthesis of mixed-oxide nanocomposite thin films for gas sensors. The chapters may be summarized in the following sections.

7.1.1 Chapter 3: Modeling of Aerosol Spray

The major findings of this chapter can be summarized thus:

- High spray mass flow rate produces droplets with high proportion of solvent.
- Increased swirl at the concentric annulus surrounding the central spray inlet enhances the radial spread and radial uniformity of droplet concentration, reduces the droplet size and generally increases the number of droplets over most of the spray.
- The effect of swirl perpetuates far from the nozzle at high swirl numbers.

The results of this study are used to optimize operating parameters for synthesis of thin film for sensor application. The parameters include nozzle diameter, mass flow rate, swirl rate, as well as the range of acceptable distance from nozzle to substrate for optimal film growth. The results are also applied for investigation of specific mixed-oxide precursor solution, detailed analysis of droplet deposition on substrate, droplet evaporation, chemical reaction and film growth.

7.1.2 Chapter 4: Modeling Evaporation and Chemical Reaction in a Multi-component Droplet

The results of this chapter demonstrate that the deposition of oxides from precursor solutions using spray pyrolysis method can be modeled subject to certain assumptions. The results appear plausible and confirm that the extent of significant chemical reaction and oxide deposition does not cover the entire the droplet domain, but is rather limited to about 60% radial distance from the center. In addition, the droplet morphology is transient and strongly dependent on the balance and interaction between the rate of water evaporation and chemical reaction. This interaction in turn is largely determined by the substrate temperature within the range of synthesis parameters investigated in the study. The findings are quite significant as they have provided insight into the parameters required for control of both the composition and morphology of metal-oxide semiconductor films. Such information is critical to the synthesis of mixed-oxide films with microstructure tailored to meet specific characteristics including nanoparticle size and inter-particle spacing. Control of these characteristics is critical to achieving the desired sensor selectivity, sensitivity and response time.

7.1.3 Chapter 5: Processing of Single and Mixed Metal-Oxide Thin Films

The findings of the study on single oxide in this chapter can be summarized thus:

- At low temperatures, small spherical crystallites of ZnO are formed which agglomerate at higher temperature.
- The density and size of ZnO particles are increased by increasing the solution concentration for deposition at 400° C. The results show that both low temperature and high concentration will produce packed ZnO rods.

- SnO_2 film with non-homogenous structure is synthesized at 400° C which reshapes to porous microstructure by increasing the temperature to 450° C. The composition of SnO_2 is however largely unaffected by temperature above 450° C.
- It is necessary to increase the concentration of Sn precursor in order to form packed rod arrays.

The study also has demonstrated the similarities and differences between the two metal oxides (ZnO and SnO_2) considered thus:

a. Non-homogenous film structures are observed at almost the same low temperatures, and crack-free films are formed by increasing the temperature in both cases.
b. SnO_2 requires a higher temperature and concentration than ZnO to produce continuous films.

The findings of this chapter on the mixed metal oxides (ZnO+In_2O_3 and SnO_2+In_2O_3) can be summarized in the following:

- ZnO+In_2O_3 deposition exhibits increasing particle size with increasing precursor solution concentration and Zn composition.
- Doping ZnO with indium oxide component results in a less homogenous particle size distribution. Thus indium ions limit the growth of ZnO particles in the mixture.
- ZnO nano wires are grown at low concentration of Zn. By increasing this concentration, ZnO rods grow and tend to reshape to nano tubes with distinct side walls.
- SnO_2+In_2O_3 film with more homogenous structure is formed at 80% ratio of tin. The precursor solution does not have sufficient time to form a continuous film at high concentration of Sn.

The morphology of the $ZnO+In_2O_3$ composite films depends strongly on the composition of the film. It was shown that the film of composition 25 wt% ZnO+75 wt% In_2O_3 contains a large number of small crystal aggregates of arbitrary shape and therefore has a high density of contacts between the aggregates. It should be emphasized that only the films with good homogeneous structure demonstrated high sensory properties. In this range of aggregate composition the relationship between the particles of the catalytically active component (ZnO), that breaks hydrogen molecules, and In_2O_3 particles with a high concentration of conduction electrons, is close to optimal value. Therefore, due to both morphology and electronic structure of the films of this composition, the sensor response to hydrogen in air ambience is able to reach the maximal value.

These findings could be significant in the choice of processing conditions for production of metal oxide films for next-generation highly selective and sensitive conductometric gas sensors with ultra-fast response. Such sensors are critical to the detection of hazardous environmental substances, and explosives. Specifically, the precise micro-structure of the sensor films determines the adsorption of analyzed gas on the semiconductor particles as well as interaction with the sensitive layer of the film. The results of this chapter have shown that this objective could be achieved through careful control of the substrate temperature and concentration of precursor solution.

7.1.4 Chapter 6: Mathematical Modeling and Experimental Validation of Film Growth

The predicted results from this chapter demonstrate the important roles that temperature, concentration and deposition duration play on film growth. This finding is in agreement with previous studies. The model however extends beyond the experiment by indicating the threshold deposition duration at which the initial rapid film growth seizes and the film thickness stabilizes by diffusion.

The model was validated with experimental results for both single oxide (ZnO) and mixed oxide ($ZnO+In_2O_3$) film growth. Both sets of results indicate that by increasing the concentration of precursors, particles grow faster and develop into large-sized crystals. At low concentration, the particles are smaller and the size distribution is less homogeneous. The results also indicate random orientation of crystallites and smaller particle sizes at low temperature.

SEM micrographs of synthesized films were used to measure particle size distribution on film surface. The predicted and measured particle size and film thickness are on the same order of magnitude. The accuracy of the model significantly improves at high substrate temperatures for which the reaction rate is close to the stoichiometric condition.

The mathematical model developed could potentially be applied in a variety of situations. For example, the results from the decomposition model can be used to determine the optimum condition to synthesize thin films with homogeneous particle size distribution.

7.2 Recommendations for Future Studies

It is recommended to investigate the following aspects for future studies:

7.2.1 Measurement of physical and dynamic properties of droplets in flight and on surface

There are different physical and chemical phenomena involved to grow nano-size particles on a non-conductive substrate. These phenomena are occurring on a short period of time subsequently and simultaneously. An engineer approach should be applied to break this continuous process into scientifically meaningful stages. Each of these stages needs to be defined in a theoretical or practical way. These definitions are supported by governing equations and fundamental concepts. Therefore, developing a comprehensive model for the whole process is completely achievable in theory. However, because of the level of the complexity involved in the nature of this problem, these models should be developed either empirically or mathematically or as a combination of both. The main stages of the models were already developed in this research: multi-component solution atomization; solution evaporation, multi-phase transport; chemical reaction between the precursors and the solvent, and film growth on the heated substrate. These models need to be verified for each case by conducting measurement techniques. Considering the initial stages of the process, the following parameters can be measured:

a) Temperature inside the droplet using laser induced methods.
b) Size of the droplet while approaching to the heated surface.
c) Velocity of droplet in flight.

The obtained values will be used as the input parameters of the evaporation model. The data will also be analyzed to determine the evaporation rate at each stage. This rate can be considered as a variable parameter influenced by changing the temperature and concentration inside the droplet. The results will be implemented in models to achieve more accurate prediction of thin film growth rate.

7.2.2 Optimization and test of synthesized films for gas sensor applications

There are three stages to improve the sensor properties of the deposited thin films:

Stage 1: The mixed metal oxide films were synthesized at different experimental conditions. The surface morphology of the films was investigated by characterization techniques in order to find the influence of deposition parameters on the structural characteristics of the films. A thorough study on the morphology of the deposited film can be performed to determine the particle size and distribution for each case of metal oxide. A comprehensive solution will also require extending the range of temperature and concentration investigated as well as other synthesis conditions. These parameters play a key role in understanding the actual interaction between thin film material and surrounding gases.

Stage 2: These nano-structured films deposited on a heated surface can potentially detect the presence and concentration of specific gases. Such a study would be followed by the design and testing of the sensor film on specific analytes. The measured response will be analyzed to determine the desired structure for each material. In order to achieve this goal, the electrical conductivity of the film will be tested by exposing it to specific gases. This test will be used to calibrate the film as a gas sensor. Sensitivity, selectivity and the response time for each film will be assumed as the optimization parameters. These parameters would be correlated to the particle size and distribution, as discussed in the previous stage.

Stage 3: The results of these studies could also be useful in the determination of the optimum conditions required to produce the desired films to meet specific performance characteristics. A backward analysis will be done to find the optimum initial conditions. The conditions are simply spray system working condition and the surface thermal conditions. By choosing limited number of parameters, this optimization will be repeatable for different combination of precursors in order to produce different metal oxide sensors. The next step will be developing an optimization model to show how setting experimental conditions can affect synthesizing the thin films. This optimization method will consider all main effective parameters in the process, such as the temperature of the surface, the concentration of the precursors in solution etc.